ETH-Diss.-No **19245**

Analysis of Z Boson Production in the Electron Channel with the CMS Detector at the LHC

A dissertation submitted to
ETH Zurich

for the degree of
Doctor of Sciences

presented by
Carmelo Marchica

Dipl.-Phys. ETH Zurich
born December 14th, 1976
citizen of Regensdorf (Zurich)
Switzerland

CERN-THESIS-2010-220
//2010

accepted on recommendation of

Prof. G. Dissertori	examiner
Prof. K. Kirch	co-examiner

2010

Abstract

A Monte Carlo (MC) analysis of Z bosons, based on the selection of electrons and positrons which will be produced at the LHC, is presented. In doing so, a full simulation based on the CMS detector was taken into account. Owing to a lack of data, a small dataset, so called pseudo data, with an integrated luminosity of $10\,\mathrm{pb}^{-1}$, at a center-of-mass energy of 10 TeV, was used. A simple and robust electron/positron selection procedure for the central part of the detector was devised. It was shown that this selection leads to practically background free sample of Z bosons. Based on the Z boson counting, with a statistical uncertainty of $\pm 3\%$, an efficiency correction of $\pm 3\%$ and the uncertainty on the integrated luminosity of about $\pm 11\%$, the Z boson cross-section could be calculated and compared to its theoretical value. In addition, the same counting method was used to calculate the integrated luminosity to $\pm 6\%$, which is mainly due to a theoretical uncertainty of about $\pm 5\%$. Various distributions, such as rapidity and transversal momentum, were also considered and compared to the complete ($1.4\,\mathrm{fb}^{-1}$) MC simulation. The Z boson transverse momentum and rapidity spectrum measurement was then calculated. It was shown that such measurements with an integrated luminosity of $10\,\mathrm{pb}^{-1}$ at 10 TeV are possible, with accuracies consistent with present knowledge. A small test with real data was performed and showed an nice agreement between data and MC simulation.

Zusammenfassung

Eine auf der Selektion von Elektronen und Positronen basierenden Monte Carlo (MC) Analyse von Z Bosonen, welche am LHC produziert werden, soll präsentiert werden. Dabei wurde eine vollständige Simulation basierend auf dem CMS Detektor berücksichtig. Aus Mangel an Daten wurde ein kleiner Datensatz, der einer integrierten Luminosität von $10\,\mathrm{pb}^{-1}$ bei einer Schwerpunktsenergie von 10 TeV entspricht, als so genannte Pseudo-Daten verwendet. Eine einfache und robuste Elektron/Positron Selektion für den zentralen Teil des Detektor wurde damit erarbeitet. Es konnte gezeigt werden, dass diese Selektion zu einem praktisch untergrundfreien Sample von Z Bosons führt. Die Fähigkeit Z Bosonen zu zählen wurde dazu verwendet, um den Wirkungsquerschnitt zu berechnen und mit dem theoretischen Wert zu verglichen. Dabei wurden statistische Fehler von $\pm 3\%$ auf die Anzahl Z Bosonen, einen Fehler auf die Effizienz von $\pm 3\%$ und einen auf die integrierten Luminosität von $\pm 11\%$ berücksichtigt. Die gleiche Zählmethode wurde dazu verwendet, um die integrierte Luminosität auf $\pm 6\%$ zu bestimmen, wobei der Fehler hauptsächlich auf der theoretischen Unsicherheit von $\pm 5\%$ basiert. Anschliessend wurden verschiedene Verteilungen, wie Rapidität und transversaler Impuls betrachtet und mit der gesamten ($\sim 1.4\,\mathrm{fb}^{-1}$) MC Simulation verglichen. Danach wurden die transversale Impuls- und Rapiditätsspektren gemessen. Dabei wurde gezeigt, dass mit einer integrierten Luminosität von $10\,\mathrm{pb}^{-1}$ bei 10 TeV eine solche Messung möglich ist und die Genauigkeit dem gegenwärtigen Wissensstand entspricht. Ein kleiner Test mit realen Daten wurde durchgeführt und zeigte eine gute Übereinstimmung zwischen Daten und MC Simulation.

Contents

Contents vi

List of Tables viii

List of Figures xii

Introduction 1

1 The Standard Model of Particle Physics 3
- 1.1 Standard Model of Particle Physics . . . 3
- 1.2 Quantum Electrodynamics . . . 6
  - 1.2.1 Global Gauge Invariance . . . 6
  - 1.2.2 Local Gauge Invariance . . . 7
- 1.3 Electroweak Theory . . . 8
  - 1.3.1 Nonabelian Local Symmetries . . . 9
  - 1.3.2 Spontaneous Symmetry Breaking . . . 10
- 1.4 Quantum Chromodynamics . . . 17
  - 1.4.1 QCD Lagrangian . . . 19
- 1.5 Experimental Parameters . . . 20
  - 1.5.1 The Running of the Strong Coupling Constant . . . 20
  - 1.5.2 Parton Distribution Functions . . . 22
  - 1.5.3 Lepton Pair Production . . . 24
- 1.6 Tests and Limits of the Standard Model . . . 26

2 The Collider Experiment 29
- 2.1 Large Hadron Collider . . . 29
  - 2.1.1 The Machine Parameter . . . 31
  - 2.1.2 Machine Components . . . 33
- 2.2 Generic High Energy Physics Collider Detector . . . 35
- 2.3 Compact Muon Solenoid . . . 38
  - 2.3.1 CMS Detector Overview . . . 39
  - 2.3.2 Superconducting Magnet . . . 41

2.3.3 Inner Tracking System . . . 41
2.3.4 Electromagnetic Calorimeter . . . 44
2.3.5 Hadron Calorimeter . . . 50
2.3.6 Muon System . . . 52
2.3.7 Data Acquisition and Triggering . . . 54
2.3.8 Computing . . . 57

3 Selection of $Z \to e^+e^-$ Events **59**
3.1 Generator Level . . . 59
3.1.1 Parameters of the Generator . . . 59
3.1.2 Distributions at the Generator Level . . . 61
3.2 Electron Reconstruction . . . 65
3.2.1 Electron Seeding . . . 65
3.2.2 ECAL Energy and Position Measurements . . . 65
3.2.3 Electron Tracking and Momentum Determination . . . 66
3.3 Isolated Electron Selection at Large p_t . . . 70
3.3.1 Electron Preselection . . . 70
3.3.2 Electron Isolation . . . 74
3.3.3 Electron Identification . . . 75
3.3.4 High Level Trigger . . . 76
3.4 Z Boson Reconstruction . . . 76
3.4.1 Z Reconstruction . . . 77
3.4.2 Electron Charge Misidentification . . . 80
3.4.3 Backgrounds . . . 82
3.5 Efficiency . . . 83
3.5.1 Monte Carlo . . . 83
3.5.2 Tag and Probe . . . 84
3.6 First Data . . . 86
3.6.1 First Real Electrons . . . 86
3.6.2 First Real Z Event . . . 89

4 Physics Measurements **93**
4.1 Z Boson Distributions . . . 94
4.1.1 Invariant Z Boson Mass and Energy Calibration . . . 94
4.1.2 p_t Spectrum of the Z Boson . . . 97
4.1.3 Rapidity Spectrum of the Z Boson . . . 99
4.2 Cross-Section or Integrated Luminosity . . . 99
4.2.1 Detector Quantities . . . 102
4.2.2 Integrated Luminosity . . . 104
4.2.3 $Z \to e^+e^-$ Cross-Section . . . 105
4.3 Measuring the Z Transverse Momentum and Rapidity Spectra . . . 106

4.3.1 Measuring the Z Transverse Momentum Spectrum . . . 108
4.3.2 Measuring the Z Rapidity Spectrum . . . 109
4.4 Jet Transverse Momentum Measurement . . . 113

Conclusion **119**

Appendices

A Pauli and Dirac Matrices **121**
A.1 Pauli Matrices . . . 121
A.2 Dirac Matrices . . . 121

B Vacuum Polarization **123**
B.1 Renormalization . . . 123
B.2 Regularization . . . 125

C Momentum Resolution Measurement **127**

D Novel Technique for Studying the Z Boson Transverse Momentum **129**

E Additional Work **131**

Bibliography **133**

List of Abbreviations **140**

Acknowledgment **141**

List of Tables

1.1 Particle content of the Standard Model of Particle Physics. 4
1.2 Comparison of the weak boson masses between theoretical and experimental results. 4
1.3 Charge, hypercharge and weak isospin components of the 1st Generation. 14
1.4 Coefficients for the axial- and vector-currents of the 1st Generation. 17
1.5 Couplings of fermions to gauge bosons and its propagator terms for the GSW theory. 17
1.6 Electroweak constants. 26
1.7 Experimentally observed values compared to the SM best fit predictions. 27

2.1 LHC luminosity parameter for design and startup condition. 33
2.2 Characteristic values of crystals. 46
2.3 L1 trigger rates. 56
2.4 L1 trigger efficiency. 57

3.1 Global and signal parameter set. 60
3.2 Background parameter set for 10 TeV. 62
3.3 Number of generated events with corresponding cross-section for signal and background. 63
3.4 Number of events on generator level with initial-state radiation. 64
3.5 Resolution for track and ECAL cluster based electrons and for the combination. 68
3.6 Efficiency and fake rate after preselection in pseudorapidity. 72
3.7 Relevant values for tracker, ECAL and HCAL electron isolation. 74
3.8 HLT cuts for the electron streams. 76
3.9 Electron isolation and identification criteria for $Z \to e^+e^-$ candidates. 78
3.10 Number of Z's in the mass peak with and without electron isolation and identification criteria. 78
3.11 Number of Z candidates in the mass peak, after varying the cuts. 79
3.12 Number of reconstructed Z events within the mass peak, after relaxing one or two electrons, compared with the number of generated Z events. 79
3.13 Number of same sign Z events in the mass peak, compared with the number of misidentified electrons. 81
3.14 Z boson background within the mass peak. 82
3.15 Electron "Tag and Probe" efficiencies. 86
3.16 Relevant parameters of the electron and the positron for the first Z event. . . . 91

4.1 Mean values of the invariant Z mass for an ideal detector and for the miscalibrated detector. 95
4.2 Number of Z candidates after selection for different Z transverse momentum bins and for an integrated luminosity of $10\,\mathrm{pb}^{-1}$ and $1.4\,\mathrm{fb}^{-1}$. 98
4.3 Comparison for the strong coupling constant and the cross-section for different PDF sets. 101
4.4 Z boson cross-section for different MC generators. 102
4.5 Statistical and systematic errors for the relevant quantities. 105

E.1 Validation work list. 131

List of Figures

1.1 Leading order Feynman diagram for $q\bar{q} \to \gamma^*/Z \to e^+e^-$ process. 5
1.2 Next to leading order Feynman diagrams for $q\bar{q}g \to \gamma^*/Z \to e^+e^-$ processes. . . 5
1.3 Feynman diagram for radiative correction on the Z and W boson propagator with dependence on top and Higgs mass. 15
1.4 $\Delta\chi^2 = \chi^2 - \chi^2_{\text{min}}$ as a function of Higgs mass. 15
1.5 Cross-section of the reaction $e^+e^- \to$ hadrons, normalized to $e^+e^- \to \mu^+\mu^-$, as a function of the center of mass energy. 18
1.6 Pictorial representation of the QCD Lagrangian. 20
1.7 Schematic diagram for a proton-proton interaction. 22
1.8 Parton distribution functions calculated by the MSTW collaboration. 24
1.9 Leading order Feynman diagram for the $q\bar{q} \to e^+e^-$ process. 24
1.10 Differential cross-section of $q\bar{q} \to e^+e^-$. 26

2.1 Map of the Geneva region and of the LHC. 30
2.2 First event measured with CMS. 30
2.3 A 7 TeV event recorded with CMS. 31
2.4 Livingston plot showing the energy in the constituent frame. 32
2.5 Diagram of an LHC dipole magnet. 34
2.6 LHC layout. 34
2.7 Generic particle detector for electromagnetic particles. 36
2.8 Generic particle detector for electromagnetic particles with magnet. 36
2.9 Generic particle detector without muon system. 37
2.10 Generic particle detector. 37
2.11 Generic particle detector including a vertex detector. 38
2.12 A perspective view of the CMS detector. 39
2.13 Cross-sectional and longitudinal view of CMS. 40
2.14 View of the CMS superconducting magnet with return yoke. 41
2.15 Schematic cross-section through the CMS tracker. 42
2.16 Material budget in units as a function of η for the inner tracker. 43
2.17 Layout of pixel detectors in the CMS tracker. 43
2.18 Illustration of the microscopic structure of the pixel detector. 44
2.19 ECAL energy resolution. 45
2.20 Layout of the CMS ECAL. 45
2.21 $PbWO_4$ crystals with photodetectors attached. 46
2.22 Transverse section through the ECAL, showing geometrical configuration. 47

2.23 ECAL modular structures. 47
2.24 Endcap Dee, half full equipped with supercrystals. 48
2.25 Avalanche Photodiodes. 49
2.26 Vacuum Phototriodes. 49
2.27 Invariant mass of the π^0-meson, measured with the ECAL detector. 50
2.28 Invariant mass of π^0 candidates with one of the photon legs converted. 51
2.29 Longitudinal view of the CMS detector, showing the location of the HCAL. . . . 52
2.30 Muon resolution for inner and outer track muons and global muons. 53
2.31 Layout of one quarter of the CMS muon system. 53
2.32 Architecture of the DAQ system. 55
2.33 Architecture of the L1 Trigger. 55
2.34 L1 trigger rate for jet events. 56
2.35 Data flow through CMS Computing Centers. 58

3.1 Leading order Feynman diagram for $q\bar{q} \to \gamma^*/Z \to e^+e^-$ process. 60
3.2 Feynman diagram for $gg \to t\bar{t}$ process, decay to Wb and the W's decaying in electron and positron. 61
3.3 Generated mass distribution of e^+e^- pairs. 63
3.4 Generated rapidity distribution for all Z candidates. 64
3.5 Distributions for uncorrected supercluster energy. 66
3.6 Reconstruction electron efficiency as a function of the supercluster ϕ. 67
3.7 Energy over track momentum distribution. 68
3.8 Momentum and energy resolution. 69
3.9 Momentum resolution for electrons combining the GSF track finding and the cluster energy information. 69
3.10 Double counting problem in an early stage of the electron reconstruction in combining the track finder information with the supercluster information. 70
3.11 Electron preselection distributions for electrons from $Z \to e^+e^-$ events. 71
3.12 Preselection efficiency. 72
3.13 Matching variable used to select real electrons and reject fake electrons. 73
3.14 Preselection fake rate. 73
3.15 Picture of the geometrical set-up for the isolation. 74
3.16 Distributions for the electron isolation variables for signal and background. . . . 75
3.17 Distributions for electron identification variables for signal and background. . . . 76
3.18 Invariant Z boson mass distribution after preselection. 77
3.19 Invariant Z boson mass peak, reconstructed with electrons passing the whole selection chain. 78
3.20 Draft of an electron charge misidentification by photon conversion. 80
3.21 Invariant Z mass for events with two same sign electrons. 81
3.22 Z boson mass distribution with backgrounds. 83
3.23 Electron MC efficiency for the MC sample and the pseudo data for the pseudo-rapidity and transverse momentum. 84
3.24 Supercluster MC efficiency, i.e. matched electrons with a supercluster over generated electrons. 85

3.25 Electron reconstruction efficiency measurements as a function of the supercluster η in $Z \to e^+e^-$ sample for the four steps. . . . 87
3.26 Electron reconstruction efficiency measurements as a function of the supercluster E_t in $Z \to e^+e^-$ sample for the four steps. . . . 88
3.27 Electron selection variable distributions. . . . 89
3.28 Electron isolation variable distributions. . . . 90
3.29 Electron distributions. . . . 90
3.30 Event display of the first reconstructed Z boson candidate within CMS. . . . 91

4.1 Invariant mass distribution for electron-positron pairs with opposite charge and a integrated luminosity of $10\,\mathrm{pb}^{-1}$ at 10 TeV. . . . 94
4.2 Invariant Z boson mass distribution. . . . 95
4.3 Difference between the generated and reconstructed dielectron mass distribution for electron-positron pairs. . . . 96
4.4 Mean of the Z boson mass for each supermodule with electron energy mismeasurement in ECAL a supermodule. . . . 96
4.5 Difference of the Z boson p_t for generated and reconstructed momentum for different p_t bins. . . . 98
4.6 Z boson spectrum for events passing the whole selection. . . . 98
4.7 Low Z p_t spectrum for Z candidates passing the whole selection. . . . 99
4.8 Z boson rapidity distribution for Z candidates passing the whole selection. . . . 100
4.9 Acceptance as a function of the transverse momentum of the Z boson. . . . 107
4.10 Illustration of the acceptance for high Z p_t electrons around the edge of the barrel. 107
4.11 Efficiency as a function of the transverse momentum of the Z boson. . . . 108
4.12 Differential cross-section as a function of the transverse momentum measured with the pseudo data, corresponding to $10\,\mathrm{pb}^{-1}$ at 10 TeV and compared with the normalized MC sample, corresponding to $1.4\,\mathrm{fb}^{-1}$ at 10 TeV. . . . 109
4.13 Differential cross-section as a function of the rapidity measured with the pseudo data, corresponding to $10\,\mathrm{pb}^{-1}$ at 10 TeV and compared with the normalized MC sample, corresponding to $1.4\,\mathrm{fb}^{-1}$ at 10 TeV. . . . 110
4.14 Z boson rapidity distributions for three different Z p_t cuts. . . . 111
4.15 Ratio of the Z boson rapidity distribution for different LO PDF sets. . . . 111
4.16 Kinematic ranges for different colliders. . . . 112
4.17 Bjorken x_1 distribution. . . . 113
4.18 Jet multiplicity for events with the reconstructed Z boson mass within $3\Gamma_Z$ for $1.4\,\mathrm{fb}^{-1}$. . . . 114
4.19 Jet p_t for events with a reconstructed Z boson mass within $3\Gamma_Z$. . . . 115
4.20 Z boson spectrum for the 0-jet, 1-jet and the >1-jet bin. . . . 115
4.21 Z boson spectrum compared with the jet spectrum for events with only one jet. 116
4.22 The p_t spectra for accepted W signal events in the electron channel for $25\,\mathrm{pb}^{-1}$. 117
4.23 The ratio of the reconstructed and generated W transverse momentum spectrum. 117

B.1 Feynman diagram for a leading order process ($e^+e^- \to \mu^+\mu^-$). . . . 123
B.2 Feynman diagram for a next-to-leading order process ($e^+e^- \to \mu^+\mu^-$). . . . 124

C.1 Illustration of the different variables used for the momentum determination. . . . 127

D.1 A schematic representation in the transverse plane, of the construction of a_t and a_l in a typical electron/positron Z decay. 129
D.2 Mean resolution $|X_{\text{reco}} - X_{\text{gen}}|/X_{\text{gen}}$ for each of the observables, p_t^Z, a_t and a_l as a function of the generator p_t^Z. 130

Introduction

"Particle physics" is a loose way of talking...
It is a modern name for the centuries old effort
to understand the laws of nature.
- Edward Witten [1]

Particle physics is striving to get to the bottom of the phenomena. The nature of physics lies in simplification, for only through simplification can the many different phenomena of the natural world be understood. Up to this day, it has been possible to reduce the complex structures of the known matter into only a few elements.

The Standard model of particle physics consists of 6 quarks and leptons with the corresponding antiparticles. For the interaction gluons, $W^{\pm}$, Z bosons and the photon (γ) are required, whereas gravitation is not included.

To reach this level of simplification, particle physics has come a long way. Its roots can be traced back to 500 A.D. with Empedocles, who probably would not have characterized himself as a particle physicist. He significantly shaped the teachings of the 4 elements, fire, earth, air and water. In doing so he saw love (Philotes) and hate (Neikos) as primal forces, which unite and separate the 4 elements.

Experimental results combined with theoretical ideas have transformed the ancient into a modern view. The last quark was added in 1995 with the discovery of the top quark [2]. During this period the number of experiments grew steadily and so did the collaborations. In 1909 it was possible for Ernest Rutherford to measure the structure of the gold atom nearly single-handedly, whereas today about 10 000 scientists are registered at CERN to run the Large Hadron Collider (LHC) with its 4 experiments. Whether a similar revolutionary conclusion can be attained still is unknown. Let us hope so!

Over the last 15 years, high energy physics has been waiting for a groundbreaking discovery beyond the SM, which was developed 40-50 years ago. Considering that the factor 10-100 increase in energy during the fifties and sixties lead to the discovery of 3 further quarks and the heaviest lepton in the seventies, the high expectations put on the LHC are understandable. With the factor of 10 increase expected from the LHC, it is possible to explore a new regime of energy. In the last 20 years the Tevatron has scratched the surface of the TeV scale and the

LHC will clearly reach it.

One can therefore certainly state that particle physics, especially high energy physics, has come to a turning point and the next 10 to 20 years will significantly contribute and define the course particle physics research will take.

Many theoretical models seem to be just waiting to be confirmed by experiments, thus to be "gotten from the bottom of the deck". The more well known models, such as the Higgs-mechanism or supersymmetry, remain only models, as long as they are not confirmed by experimental results. The LHC will be probably the only machine that can directly provide answers within the next 20 years.

I consider myself fortunate to be involved in the research of particle physics during these exciting times and at the same time it is bad luck that my PhD time is now coming to an end. Due to the delay of the launch of the LHC, the data which I would have liked to analyze for my dissertation was not available. For this reason I am constrained to present an analysis, which is based upon simulated data, so called Monte Carlo data. This data correspond to an integrated luminosity of $10\,\mathrm{pb}^{-1}$ at a center-of-mass energy of 10 TeV, although the start up energy of the LHC is 7 TeV. The decision to run on 7 TeV came rather late, to redo the analysis with 7 TeV. The $10\,\mathrm{pb}^{-1}$ at 10 TeV correspond, roughly, to $25\,\mathrm{pb}^{-1}$ at 7 TeV.

This dissertation is made up of four chapters. In the first chapter the theory of particle physics is explained, with a focus on electroweak interaction. Thereafter in the second chapter the description of the actual experiment follows. The Compact Muon Solenoid (CMS) is dissected into its single components and their meaning is explained, in doing so a special focus is put on the electromagnetic calorimeter. In the third chapter the selection of electrons and the subsequent reconstruction of Z bosons is described. In the fourth chapter the relevant physical measurements which can be done with the Z boson are presented. We focus on, firstly, the measurement of the Z spectrum, as well as the rapidity distribution and, secondly, the cross-section measurement and the integrated luminosity. The four chapters are enclosed by a brief introduction and conclusion.

Chapter 1

The Standard Model of Particle Physics

Any theory is good only if it is simple enough
to be understood by a barmaid.
- Ernest Rutherford [3]

The Standard Model of Particle Physics, in short: Standard Model (SM), is based on two gauge field theories,

- the Electroweak Theory and
- Quantum Chromodynamics.

The electroweak theory is the unified description of two fundamental interactions of nature: the electromagnetic and the weak interaction. Although these two forces appear very different at atomic energies, this theory models them as two different aspects based on a unified principle of the same force. The gauge field theory of the electromagnetism is called Quantum Electrodynamics (QED). The other, Quantum Chromodynamics (QCD), is the theory of the strong interaction, which is the third fundamental force describing the interactions of the quarks and gluons making up hadrons.

This chapter introduces the Standard Model through an illustration of its formal concept, from which we then provide a more detailed study of the two above-mentioned gauge field theories. This chapter is based on [4], in which a more detailed and complete description can be found. After the theoretical structure is introduced, the corresponding experimental parameters will be elaborated on. To conclude this chapter some tests and limits of the SM are discussed.

1.1 Standard Model of Particle Physics

Particle physics is the search for the fundamental constituents of matter and an understanding of their interactions. After many years of research the Standard Model of Particle Physics

was proposed, as a synthesis of all experimental and theoretical discoveries/results, excluding gravity. In Tab. 1.1 the elementary particles of the SM are summarized.

Standard Model of Particle Physics							
Fermions	Leptons	$< 2 \cdot 10^{-6}$ 0 1/2	ν_e electron neutrino	< 0.19 0 1/2	ν_μ muon neutrino	< 18.2 0 1/2	ν_τ tau neutrino
		0.511 −1 −1/2	e electron	106 −1 −1/2	μ muon	$1.78 \cdot 10^3$ −1 −1/2	τ tau
	Quarks	3 2/3 1/2	u up	$1.27 \cdot 10^3$ 2/3 1/2	c charm	$172 \cdot 10^3$ 2/3 1/2	t top
		6 −1/3 −1/2	d down	101 −1/3 −1/2	s strange	$4.19 \cdot 10^3$ −1/3 −1/2	b bottom
		1st		2nd		3rd	
		Generations					

Bosons		
0 0 1	γ photon	
0 0 1	g gluon	
$80.4 \cdot 10^3$ ±1 1	$W^\pm$ W boson	
$91.2 \cdot 10^3$ 0 1	Z Z boson	
mass [MeV] el. charge isospin	*symbol* *name*	

Table 1.1: Particle content of the Standard Model of Particle Physics divided into the three generations with mass, charge and spin values, taken from [5].

The particles are divided mainly into two groups: the spin-1/2 particles, so-called fermions, and the spin-1 particles, the bosons. For the fermions there is an additional division in leptons, electron like particles, and quarks, the constituents of protons and neutrons, the nucleus of the atom.

The leptons and quarks are the matter particles and they are divided into three, in principal, equal generations, wherein the only difference is the mass of the particles. The SM is in good agreement with a large number of experimental results, like the measurement of the W and Z boson mass (Tab. 1.2) or for the QED, the measurement of the anomalous magnetic dipole moment, or $(g-2)$, of the electron.

Quantity	Measured [GeV]	SM Values [GeV]
Mass of W boson	80.420 ± 0.031	80.384 ± 0.014
Mass of Z boson	91.1876 ± 0.0021	91.1874 ± 0.0021

Table 1.2: Comparison of the weak boson masses between theoretical and experimental results. Measured values taken from [5].

These results strongly support the picture that particles interact via the exchange of vector

bosons, wherein each vector boson carries a force. The photon is the carrier of the electromagnetic force and all electrically charged particles interact with it. The $W^{\pm}$ and the Z boson are the carriers of the weak force, which interact with all matter particles. The gluon is responsible for the strong interaction, with which only the quarks interact "strongly".

In this thesis, the analysis of the Z boson production at the LHC will be presented. As the title suggests, the focus is on high energy collisions producing a Z boson, which decays in a electron/positron pair. The most simple description of this process is the so-called leading order (LO) process. In Fig. 1.1 a LO Feynman diagram is shown.

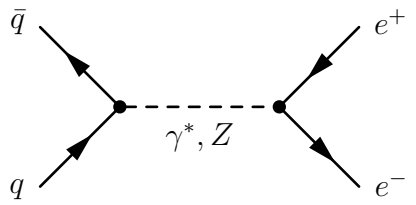

Figure 1.1: Leading order Feynman diagram for $q\bar{q} \to \gamma^*/Z \to e^+e^-$ process.

A full description requires more and more complicated higher order corrections, known as next to (next to ...) leading order (N(N)LO) corrections. In Fig. 1.2 the most important NLO Feynman diagrams are shown, with a gluon jet (left) and a quark jet (right).

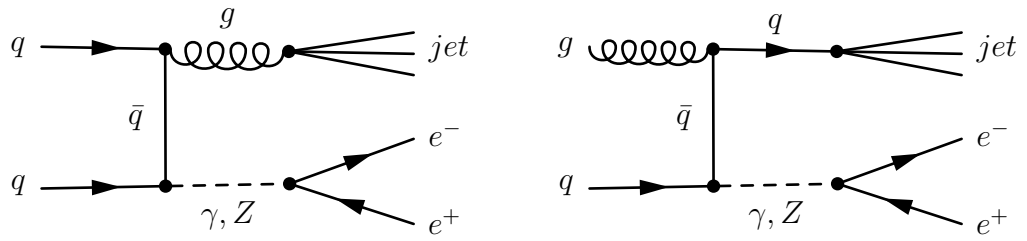

Figure 1.2: Next to leading order Feynman diagrams for $q\bar{q}g \to \gamma^*/Z \to e^+e^-$ processes, with the gluon jet (left) and the quark jet (right).

These high energy interactions are described with relativistic quantum field theories and they will be explained briefly in the following section, beginning with the QED. This leads then to the development of the electroweak theory, arising from a spontaneously broken SU(2)×U(1) symmetry. The QCD is introduced in the next stage, showing that it is a so-called asymptotically free theory, allowing to compute observable quantities for scattering processes at high momentum transfer, using perturbative approaches. The chapter ends with a introduction of parton distribution functions, which describe the momentum distribution of the components, the quarks and gluons. They are crucial parameters in hadron colliders. The analysis of the Z boson will help to determine these parameters in new energy frontiers and will enable us to apply this knowledge to verify the extrapolations done so far.

1.2 Quantum Electrodynamics

The goal of this section is to show that QED comes out naturally, by requiring local gauge invariance under a U(1) symmetry group. However firstly we will show that the conservation of the electric charge is a consequence of the global gauge invariance.

The concept of gauge invariance was first introduced by Hermann Weyl in [6]. The gauge field theories are types of field theories in which the Lagrangian $\mathcal{L}$ is invariant under a continuous group of transformations

$$\mathcal{L}(\psi, \partial_\mu \psi) \rightarrow \mathcal{L}'(\psi', \partial_\mu \psi') = \mathcal{L}(\psi, \partial_\mu \psi). \tag{1.1}$$

1.2.1 Global Gauge Invariance

Assume that the Lagrangian for the fermionic field $\psi(x)$ should be invariant under the transformations

$$\psi(x) \rightarrow \psi'(x), \tag{1.2}$$

with $\psi'(x) = U(\alpha)\psi(x)$, where $U(\alpha) = e^{i\alpha}$. The set of all transformations satisfying Eq. 1.2 is the unitary group U(1). The transformation is called global when the parameter α is constant. It is easy to show that the elements of U(1) commute [1]. Such a group is called abelian.

Consider an infinitesimal transformation for $U(\alpha)$

$$U(\alpha)\psi(x) \approx (1 + i\alpha)\psi(x) = \psi(x) + i\alpha\psi(x), \tag{1.3}$$

where $|\alpha| \rightarrow 0$. The same infinitesimal transformation for the Lagrangian $\mathcal{L}$ gives

$$\delta\mathcal{L} = \left(\frac{\partial \mathcal{L}}{\partial \psi}\right) \delta\psi + \left(\frac{\partial \mathcal{L}}{\partial(\partial_\mu \psi)}\right) \delta(\partial_\mu \psi) + \text{ c.c.} \tag{1.4}$$

then using Eq. (1.3)

$$\begin{aligned}
\delta\mathcal{L} &= \left(\frac{\partial \mathcal{L}}{\partial \psi}\right) i\alpha\psi + \left(\frac{\partial \mathcal{L}}{\partial(\partial_\mu \psi)}\right) i\alpha\partial_\mu\psi + \text{ c.c.} \\
&= i\alpha\partial_\mu \left(\frac{\partial \mathcal{L}}{\partial(\partial_\mu \psi)}\psi\right) + i\alpha \underbrace{\left[\left(\frac{\partial \mathcal{L}}{\partial \psi}\right) - \left(\partial_\mu \frac{\partial \mathcal{L}}{\partial(\partial_\mu \psi)}\right)\right]}_{=0 \text{ Euler-Lagrange-Equation}} \psi + \text{ c.c.} \\
&= i\alpha\partial_\mu \underbrace{\left(\frac{\partial \mathcal{L}}{\partial(\partial_\mu \psi)}\psi - \bar{\psi}\frac{\partial \mathcal{L}}{\partial(\partial_\mu \bar{\psi})}\right)}_{:= j^\mu} \equiv 0.
\end{aligned} \tag{1.5}$$

By using Emmy Noether's analysis of symmetries [7] it is found that a symmetry leads to a conserved current which, in turn, leads to a conserved charge. The current is with (1.5) and

[1] $U(\alpha)U(\beta) = e^{i\alpha}e^{i\beta} = e^{i(\alpha+\beta)} = e^{i(\beta+\alpha)} = e^{i\beta}e^{i\alpha} = U(\beta)U(\alpha)$∎

the Dirac-Lagrangian [2] [8] describing fermions

$$\begin{aligned} j^\mu &= i\left(\frac{\partial\mathcal{L}}{\partial(\partial_\mu\psi)}\psi - \bar{\psi}\frac{\partial\mathcal{L}}{\partial(\partial_\mu\bar{\psi})}\right) = i\left(i\bar{\psi}\gamma^\mu\psi - 0\right) \\ &= -\bar{\psi}\gamma^\mu\psi, \end{aligned} \tag{1.6}$$

where γ^μ are the Dirac-Matrices [3]. The conservation condition is then [4]

$$\partial_\mu j^\mu = 0 \quad \Rightarrow \quad \partial_t \underbrace{\int d^3\vec{x}\; j^0}_{=Q} = 0. \tag{1.7}$$

By using the global gauge invariance for the Dirac-Lagrangian, one gets a conserved current which is equivalent to the conservation of the electric charge (Q).

1.2.2 Local Gauge Invariance

Let us go further and consider a local transformation of U(1) and require that the Dirac-Lagrangian be conserved under the following transformation

$$U(\alpha(x)) = e^{ig\alpha(x)}, \tag{1.8}$$

where the constant g is arbitrarily extracted from the term $\alpha(x)$. The local gauge transformation is

$$\psi \to \psi' = e^{ig\alpha(x)}\psi. \tag{1.9}$$

Obviously the mass term $m\bar{\psi}\psi$ is invariant. By focusing on the kinetic term

$$\partial_\mu\psi \to \partial_\mu\left(e^{ig\alpha(x)}\psi\right) = e^{ig\alpha(x)}\partial_\mu\psi + \underbrace{ig\left(\partial_\mu\alpha(x)\right)e^{ig\alpha(x)}\psi}_{\text{breaks gauge invariance}} \neq e^{ig\alpha(x)}(\partial_\mu\psi), \tag{1.10}$$

the local transformation breaks the gauge invariance. By introducing a gauge invariant derivative D_μ

$$D_\mu = \partial_\mu + igA_\mu, \tag{1.11}$$

one arrives at the local gauge invariance. The gauge invariant derivative has to be applied on the fermionic field, and the following transformation

$$(D_\mu)'\left(e^{ig\alpha(x)}\psi\right) = (\partial_\mu + igA'_\mu)\left(e^{ig\alpha(x)}\psi\right) \stackrel{!}{=} e^{ig\alpha(x)}(\partial_\mu + igA_\mu)\psi, \tag{1.12}$$

has to be satisfied. By using Eq. (1.12) the transformation behavior of A_μ can be constructed as

$$A'_\mu = A_\mu - \partial_\mu\alpha(x). \tag{1.13}$$

In this case, the gauge field A_μ is an arbitrary function which fulfils the local gauge invariance.

[2] $\mathcal{L}_{Dirac} = i\bar{\psi}\gamma^\mu\partial_\mu\psi - m\bar{\psi}\psi$

[3] The so-called standard representation for the Dirac-Matrices is used. Its exact definition can be found in Appendix A.

[4] Summation over repeated indices is implied everywhere.

The function A_μ can be identified as the photon field and the transformation in Eq. (1.13) is allowed by the gauge freedom of Maxwell's equations. Thus one adds the kinetic term of the photon field to the Lagrangian

$$-\frac{1}{4}F_{\mu\nu}F^{\mu\nu}, \tag{1.14}$$

where the field tensor $F_{\mu\nu}$ is defined as [5]

$$\begin{aligned} igF_{\mu\nu} &= [D_\mu, D_\nu] \\ &= ig(\partial_\mu A_\nu - \partial_\nu A_\mu), \end{aligned} \tag{1.15}$$

and one gets

$$F_{\mu\nu} = \partial_\mu A_\nu - \partial_\nu A_\mu. \tag{1.16}$$

All other terms, namely a mass term for the photon field A_μ, would break the symmetry under the local transformation of Eq. (1.9).

By requiring local gauge invariance one gets the QED Lagrangian

$$\mathcal{L}_{QED} = i\bar{\psi}\gamma^\mu D_\mu \psi - \frac{1}{4}F_{\mu\nu}F^{\mu\nu} - m\bar{\psi}\psi \equiv \mathcal{L}_{\mathrm{U}(1)}, \tag{1.17}$$

describing the interaction of electrically charged fermions via the photon field, where $g = e$ is just the electric charge of the electron.

In this section, it was shown how powerful the concept of symmetry is. By starting with a Lagrangian, which is invariant under a local abelian symmetry group, one ends up with the QED Lagrangian. In the following section, this concept will be extended to nonabelian local symmetry groups, SU(2) and SU(3). This leads to the electroweak theory and the QCD, respectively.

1.3 Electroweak Theory

In the 19^{th} century, it was realized, mainly through the work of Hans Christian Ørsted and Michael Faraday, that electricity and magnetism are closely related, and are in fact two different aspects of the electromagnetic force. The final synthesis was presented in the 1860s by James Clerk Maxwell [9]. His work predicted the existence of electromagnetic waves and interpreted light as an electromagnetic wave phenomenon.

The first theory of weak interaction was put forward in 1934 by the Italian physicist Enrico Fermi. However, a few key experiments were crucial for further development of the theory. Namely:

- The introduction of a light neutral particle, ν_e, in a decay process such as

$$^{22}_{11}\mathrm{Na} \rightarrow {}^{22}_{10}\mathrm{Ne} + e^+ + \nu_e$$

  was Pauli's solution in 1930 to the problem of the continuous nature of the β spectrum.

[5] The commutator $[A, B]$ is defined as $[A, B] \equiv AB - BA$.

- A successful demonstration of an inverse β process using reactor antineutrinos was made 1959 by Reines and Cowan [10].
- Up until the early 1950s it was a common belief that all interactions were invariant under spatial inversion. The so-called τ-θ puzzle however cast doubt on this assumption, in relation to the weak interactions.
- In 1956 Lee and Yang [11] resolved the puzzle by suggesting that the τ and θ were different decay modes of the same particle (the K meson) and the parity was not conserved in the weak interactions.
- Parity non-conservation was first established by Wu at al. [12] by measuring the angular distribution of electrons, emitted in the decay of ^{60}Co, relative to the orientation of the nuclear spin.

The hypothesis of Lee and Yang and its confirmation by Wu et al. was followed by a period of intense experimental and theoretical activity aimed at understanding the detailed nature of the weak interaction. One of these works was the measurement of the helicity of the neutrino by Goldhaber et al. [13].

- In the early 1960s, experiments performed at Brookhaven and CERN produced conclusive evidence that a neutrino (ν_μ) quite distinct from the electron neutrino, is associated with the muon.

In a series of separate works in the 1960s, Sheldon L. Glashow, Abdus Salam and Steven Weinberg developed a theory [14] which is applicable at higher energies, and which, at the same time, unifies the weak and electromagnetic interactions in a common formalism. This theory become known as electroweak theory. It is formulated in the Glashow-Salam-Weinberg Model (GSW) as a SU(2)×U(1) gauge field theory, including the Higgs-Mechanism to generate the masses [15].

The final steps in establishing the electroweak part of the SM experimentally were the discovery of the neutral currents in neutrino scattering by the Gargamelle Collaboration [16], and the discovery of the gauge bosons $W^\pm$ and Z in $\bar{p}p$ collisions at the S$\bar{p}p$S collider by the UA1 and UA2 Collaborations [17].

In the following section we will extend the concept of symmetries to nonabelian local symmetries. The main difference in the Lagrangian is that there are more coupling terms, so-called self coupling terms. To get the real electroweak Lagrangian, with its massive vector bosons, it is necessary to break the local symmetry, by introducing a so-called Higgs-Field, with a non vanishing potential. This symmetry breaking mechanism is shown first for a U(1) symmetry group and then for the GSW model.

1.3.1 Nonabelian Local Symmetries

We have demonstrated above how easily one can construct a gauge field, by imposing a local symmetry. We now want to expand the discussion to a SU(n) group transformation [6]. The field

[6] We generalize the concept at this point, so that it can be also used in section 1.4 for the SU(3) symmetry group.

then is transformed as

$$\psi \to \psi' = e^{ig\alpha^a(x)t^a}\psi, \tag{1.18}$$

where $\alpha^a = \alpha^a(x)$ depends on x, and renders the symmetry local again. Here the t^a are generators of the symmetry group [7] and are represented by $n \times n$ hermitian matrices, with n the dimension of the symmetry group.

In the same way as was done for the QED case, we replace the derivative in the Lagrangian with the covariant derivative

$$D_\mu = \partial_\mu - igA^a_\mu t^a, \tag{1.19}$$

where A^a_μ is a new field for each generator t^a of the group. In this case one not only gets one field tensor, but for each field, one gets a field tensor $F^a_{\mu\nu}$, namely

$$igF^a_{\mu\nu}t^a = [D_\mu, D_\nu] = ig(\partial_\mu A^a_\nu - \partial_\nu A^a_\mu + gf^{abc}A^b_\mu A^c_\nu)t^a \tag{1.20}$$

thus

$$F^a_{\mu\nu} = \partial_\mu A^a_\nu - \partial_\nu A^a_\mu + gf^{abc}A^b_\mu A^c_\nu. \tag{1.21}$$

The last term in Eq. (1.21) is explicit due to the fact that the group generators t^a do not commute. The so-called structure constant of the symmetry group f^{abc} is defined by the commutation relation of the generators

$$[t^a, t^b] = if^{abc}t^c. \tag{1.22}$$

The general Lagrangian now looks very similar to the one in Eq. (1.17)

$$\mathcal{L}_{\mathrm{SU}(n)} = i\bar{\psi}\gamma^\mu D_\mu\psi - \frac{1}{4}F^a_{\mu\nu}F^{a\,\mu\nu} - m\bar{\psi}\psi. \tag{1.23}$$

The main difference between the nonabelian Eq. (1.23) and the abelian Lagrangian Eq. (1.17), is the term with the field tensors. In the general case, we have interaction terms (terms with at least three fields) with three and even four gauge fields. However in the QED case, the only interaction terms are those between fermion fields and the gauge field.

1.3.2 Spontaneous Symmetry Breaking

Spontaneous symmetry breaking has long been known in condensed matter physics, when in 1960 Yoichiro Nambu [18] made the profound assumption that it could also exist in quantum field theory for elementary particles. The beauty of this breaking is that even though the ground state is non symmetric, all the virtues of the symmetry are still there in the theory, and calculations can be performed using the restrictions that the symmetry provides.

Higgs-Mechanism for U(1)

Let us consider in a first approach, a complex scalar field ϕ that transforms under U(1), i.e.,

$$\phi \to \phi' = e^{ia(x)}\phi. \tag{1.24}$$

[7] For the symmetry group U(1) the generator is the identity, $\mathbb{1}$.

The Lagrangian for the field is

$$\mathcal{L}_\phi = (D_\mu \phi^*)(D^\mu \phi) - V(\phi) - \frac{1}{4} F_{\mu\nu} F^{\mu\nu}, \tag{1.25}$$

where

$$V(\phi) = \mu^2 |\phi|^2 + \lambda |\phi|^4, \tag{1.26}$$

and

$$D_\mu = \partial_\mu + igA_\mu. \tag{1.27}$$

The potential $V(\phi)$ has for $\mu^2 > 0$ and $\lambda > 0$ the minimum at $\phi_0 = 0$. To break the symmetry one has to choose $\mu^2 < 0$ and so one gets the minimum at

$$|\phi_0|^2 = -\frac{\mu}{2\lambda}. \tag{1.28}$$

This value is called the vacuum expectation value (VEV). Now let us expand the field around the minimum

$$\phi(x) = \phi_0 + \frac{1}{\sqrt{2}} \left(\phi_1(x) + i\phi_2(x)\right). \tag{1.29}$$

Replace ϕ in Eq. (1.25) with the new definition in Eq. (1.29) and consider just the first term

$$\begin{aligned}
(D_\mu \phi^*)(D^\mu \phi) &= \left[D_\mu \left(\phi_0^* + \frac{1}{\sqrt{2}}(\phi_1 - i\phi_2)\right)\right] \left[D^\mu \left(\phi_0 + \frac{1}{\sqrt{2}}(\phi_1 + i\phi_2)\right)\right] \\
&= \frac{1}{2} \left[D_\mu(\phi_1 - i\phi_2)\right] \left[D^\mu(\phi_1 + i\phi_2)\right] + (D_\mu \phi_0^*)(D^\mu \phi_0) + ... \\
&= \frac{1}{2}(D_\mu \phi_1)^2 + \frac{1}{2}(D_\mu \phi_2)^2 + (igA_\mu \phi_0^*)\,(igA^\mu \phi_0) + ... \\
&= \frac{1}{2}(\partial_\mu \phi_1)^2 + \frac{1}{2}(\partial_\mu \phi_2)^2 - g^2 \phi_0^2 A_\mu A^\mu + ...
\end{aligned}$$

Finally one sees that the last term has a mass form,

$$-\frac{1}{2} m_A^2 A_\mu A^\mu \equiv -g^2 \phi_0^2 A_\mu A^\mu, \tag{1.30}$$

and for the mass of the gauge boson

$$m_A^2 = 2g^2 \phi_0^2. \tag{1.31}$$

If the symmetry is not broken, $\phi_0 = 0$, thus $m_A^2 = 0$. This implies that one needs a non vanishing minimum to get masses unequal zero.

Glashow-Salam-Weinberg Model

As described in Steven Weinberg [19], we now outline the Glashow-Salam-Weinberg model. We will restrict our attention to symmetry groups that connect the observed electron type particles, the left handed doublet and the right handed singlet [8]

$$L \equiv \left(\frac{1 - \gamma_5}{2}\right) \begin{pmatrix} \nu_e \\ e \end{pmatrix} \quad \text{and} \quad R \equiv \left(\frac{1 + \gamma_5}{2}\right) e. \tag{1.32}$$

[8] Definition of γ^5 can be found in Appendix A.

The kinematic terms of the Lagrangian are

$$\mathcal{L}_{kin} = -i\bar{L}\gamma^{\mu}\partial_{\mu}L - i\bar{R}\gamma^{\mu}\partial_{\mu}R. \tag{1.33}$$

The largest group that leaves invariant $\mathcal{L}_{kin}$ are the isospin T^a acting on L and the numbers of left (N_L) and right (N_R) handed leptons acting on R. Two of these symmetries are unbroken, the charge $Q = T^3 + (N_R + 1/2N_L)$ and the lepton number $N = N_R + N_L$. As it was shown above, the gauge field corresponding to an unbroken symmetry has zero mass. In addition, there is no massless particle coupled to N [20]. So the gauge group has to be formed out of the isospin T^a [21] and the hypercharge Y, defined as

$$Y \equiv N_R + \frac{1}{2}N_L. \tag{1.34}$$

Therefore, the Lagrangian is constructed out of L, R, the gauge fields A^a_μ and B_μ coupled to T^a and Y, plus a spin zero doublet (Higgs-Field)

$$\phi = \begin{pmatrix} \phi^+ \\ \phi^0 \end{pmatrix} \tag{1.35}$$

whose VEV will break T^a and Y and give the bosons (and leptons) their masses. The only renormalizable [9] Lagrangian is

$$\begin{aligned} \mathcal{L} = \; & -\frac{1}{4}F^a_{\mu\nu}F^{a\,\mu\nu} - \frac{1}{4}F_{\mu\nu}F^{\mu\nu} - \bar{R}\gamma^{\mu}D^{\mathrm{U}(1)}_{\mu}R - \bar{L}\gamma^{\mu}D^{\mathrm{SU}(2)\times\mathrm{U}(1)}_{\mu}L \\ & -\frac{1}{2}|D^{\mathrm{SU}(2)\times\mathrm{U}(1)}_{\mu}\phi|^2 - \lambda_e(\bar{L}\phi R + \bar{R}\phi^{\dagger}L) - V(\phi), \end{aligned} \tag{1.36}$$

where

$$D^{\mathrm{U}(1)}_{\mu} = \partial_{\mu} - ig'B_{\mu} \quad \text{and} \tag{1.37}$$

$$D^{\mathrm{SU}(2)\times\mathrm{U}(1)}_{\mu} = \partial_{\mu} - igA^a_{\mu}t^a - ig'B_{\mu}. \tag{1.38}$$

Since the Lagrangian is gauge invariant, one can perform a combined isospin and hypercharge gauge transformation which eliminates three of the four real fields [22]. This means that we are able to simplify Eq. (1.36) by replacing ϕ with its VEV

$$\phi = \frac{1}{\sqrt{2}}\begin{pmatrix} 0 \\ v \end{pmatrix}. \tag{1.39}$$

The first four terms in Eq. (1.36) remain intact, while the rest of the Lagrangian, without the potential $V(\phi)$, becomes

$$\frac{1}{8}v^2g^2\left[(A^1_\mu)^2 + (A^2_\mu)^2\right] - \frac{1}{8}v^2\left(-gA^3_\mu + g'B_\mu\right)^2 - v\lambda_e\bar{e}e, \tag{1.40}$$

[9] A few comments on renormalization can be found in Appendix B.

where the lepton mass is $v\lambda_e$. The massive spin-1 fields are

$$W_\mu^\pm \equiv \frac{1}{\sqrt{2}}\left(A_\mu^1 \mp iA_\mu^2\right) \quad \text{and} \tag{1.41}$$

$$Z_\mu \equiv \frac{1}{\sqrt{g^2+g'^2}}\left(-gA_\mu^3 + g'B_\mu\right). \tag{1.42}$$

The massless spin-1 field orthogonal to the Z_μ field is

$$A_\mu \equiv \frac{1}{\sqrt{g^2+g'^2}}\left(g'A_\mu^3 + gB_\mu\right). \tag{1.43}$$

Their masses are

$$M_{W^\pm} = \frac{1}{2}vg, \quad M_Z = \frac{1}{2}v\sqrt{g^2+g'^2} \quad \text{and} \quad M_A = 0. \tag{1.44}$$

As required, the theory consists of three massive and one massless field.

We would like to rewrite the covariant derivative $D_\mu^{\mathrm{SU(2)\times U(1)}}$ with the mass eigenstate fields $W_\mu^\pm$, Z_μ and A_μ. Without loss of generality we add the hypercharge Y to the B_μ field and the general generators t^a are replaced by the isospin operators T^a, defined as

$$T^a = \frac{\sigma^a}{2} \tag{1.45}$$

where σ are the Pauli-matrices (see Appendix A). One obtains

$$\begin{aligned} D_\mu^{\mathrm{SU(2)\times U(1)}} = \partial_\mu &- \frac{ig}{\sqrt{2}}\left(W_\mu^+T^+ + W_\mu^-T^-\right) \\ &- \frac{i}{\sqrt{g^2+g'^2}}Z_\mu\left(g^2T^3 - g'^2Y\right) \\ &- \frac{igg'}{\sqrt{g^2+g'^2}}A_\mu(T^3+Y), \end{aligned} \tag{1.46}$$

where the operators $T^\pm$ are defined as $T^\pm = T^1 \pm iT^2$, and are the isospin creation and annihilation operators.

A_μ has to be identified with the photon field, its coupling should be the electromagnetic coupling constant e, i.e.,

$$e = \frac{gg'}{\sqrt{g^2+g'^2}}, \tag{1.47}$$

and its quantum number the electric charge is $Q = T^3 + Y$. To simplify further, the mixing of the fields A_μ^3 and B_μ can be parametrized with the so-called weak mixing angle θ_w as

$$\begin{pmatrix} Z_\mu \\ A_\mu \end{pmatrix} = \begin{pmatrix} \cos\theta_w & -\sin\theta_w \\ \sin\theta_w & \cos\theta_w \end{pmatrix} \begin{pmatrix} A_\mu^3 \\ B_\mu \end{pmatrix}, \tag{1.48}$$

with

$$\cos\theta_w = \frac{g}{\sqrt{g^2+g'^2}} \quad \text{and} \quad \sin\theta_w = \frac{g'}{\sqrt{g^2+g'^2}}. \tag{1.49}$$

The covariant derivative Eq. (1.47) becomes then

$$D_\mu^{\mathrm{SU(2)\times U(1)}} = \partial_\mu - \frac{ig}{\sqrt{2}}\left(W_\mu^+ T^+ + W_\mu^- T^-\right) - \frac{ig}{\cos\theta_w} Z_\mu \left(T^3 - \sin^2\theta_w Q\right) - ieA_\mu Q, \tag{1.50}$$

with $e = g\sin\theta_w$. The constants Q, T^3 and Y are summarized in Tab. 1.3.

	Fermions f	Q	T^3	Y
Doublets	$\begin{pmatrix}\nu\\ e\end{pmatrix}_L$	0 -1	$+1/2$ $-1/2$	$-1/2$
	$\begin{pmatrix}u\\ d\end{pmatrix}_L$	$+2/3$ $-1/3$	$+1/2$ $-1/2$	$+1/6$
Singlets	e_R	-1	0	-1
	u_R	$+2/3$	0	$+2/3$
	d_R	$-1/3$	0	$-1/3$

Table 1.3: Charge, hypercharge and weak isospin components of the 1st Generation.

All the couplings are described by three parameters, the electron charge e, a new parameter θ_w, and the mass of one massive boson, since

$$m_W = m_Z \cos\theta_w. \tag{1.51}$$

Some of these quantities are influenced by radiative corrections, which make these measurements also sensitive to the top (m_t) and the Higgs mass (m_H). The radiative corrections for the Z and W bosons are shown in Fig. 1.3.

In Fig. 1.4 the constraints on the Higgs boson mass, arising from fitting all high-Q^2 data of LEP experiments, is shown. An additional exclusion region from combined DØ and CDF results is added in the plot.

Couplings to Fermions

Now we would like to compute the coupling terms to the gauge bosons for the 1st Generation of the fermions. It has been shown in several experiments (e.g. [13]) that the W boson only couples to left handed fermions. As already shown in Eq. (1.32), one can decouple the fermion fields into a left and a right handed field. By relabeling the fermions of the 1st Generation, they are distinguishable

$$L_e = \begin{pmatrix}\nu\\ e\end{pmatrix}_L \quad \text{and} \quad R_e = e_R, \tag{1.52}$$

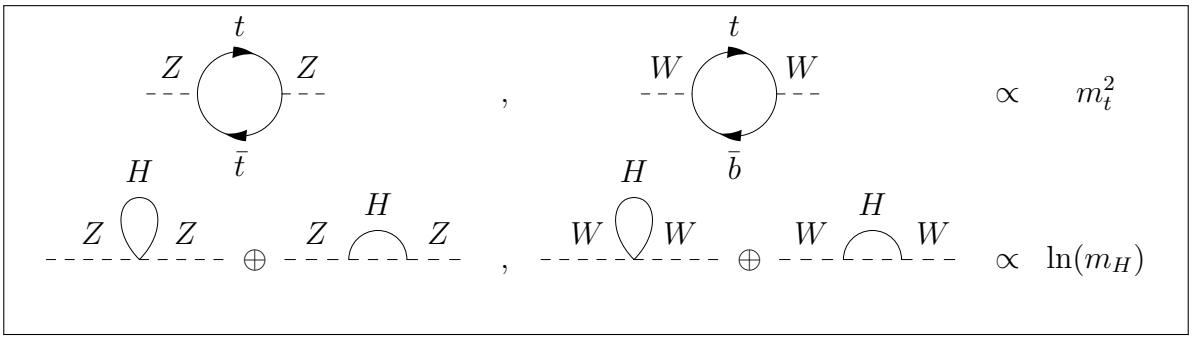

Figure 1.3: Feynman diagram for radiative correction on the Z and W boson propagator with dependence on top m_t and Higgs mass m_H.

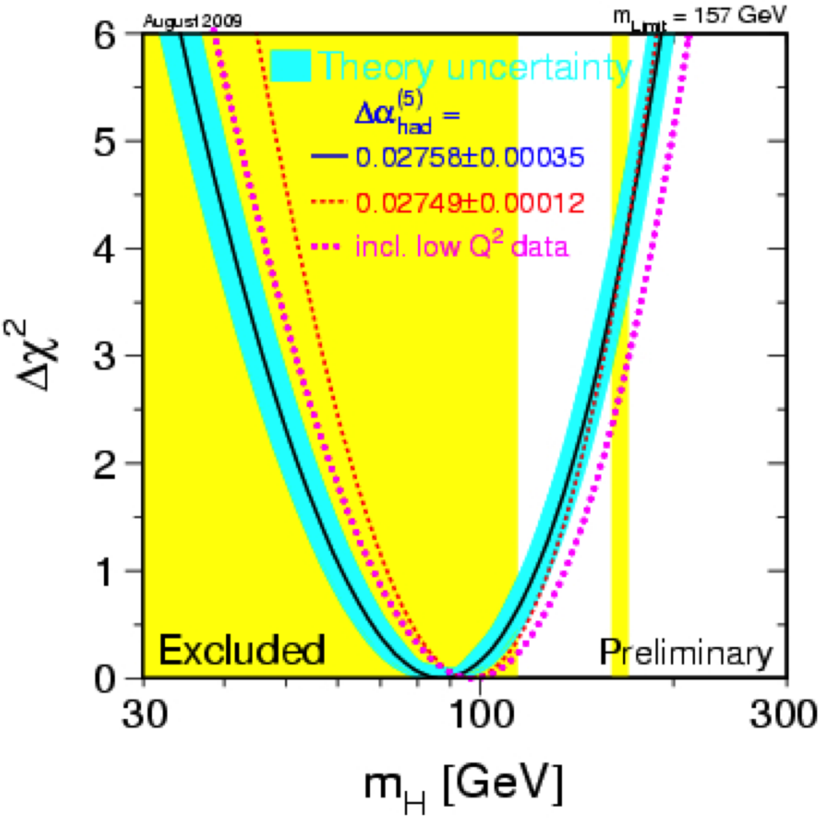

Figure 1.4: $\Delta\chi^2 = \chi^2 - \chi^2_{\text{min}}$ as a function of Higgs mass m_H. The solid line is the result of the fit, and the blue band represents an estimate of the theoretical error due to missing higher order corrections. The red dashed curve is the result obtained using an alternative evaluation of $\Delta\alpha^5_{\text{had}}$, the hadronic contribution to the photon vacuum polarization. The magenta dotted curve corresponds to a fit including low-Q^2 data, such as neutrino-nucleon scattering. The yellow shaded regions indicate the exclusion regions from direct searches at LEP and the Tevatron. [23]

as well as

$$L_u = \begin{pmatrix} u \\ d \end{pmatrix}_L, \quad R_u = u_R \quad \text{and} \quad R_d = d_R. \tag{1.53}$$

By analyzing the kinetic term of the Lagrangian, the couplings are

$$\mathcal{L}_{\text{kin}} = i\bar{L}_e \not{D} L_e + i\bar{R}_e \not{D} R_e + i\bar{L}_u \not{D} L_u + i\bar{R}_u \not{D} R_u + i\bar{R}_d \not{D} R_d \tag{1.54}$$

with $\not{D} \equiv \gamma^\mu D_\mu$ [10]. In each term, the covariant derivative is given by Eq. (1.50), with T^a and Y evaluated in the particular representation to which that fermion belongs. With Eq. (1.50) one gets

$$\begin{aligned} \mathcal{L}_{\text{kin}} = \; & + \; i\bar{L}_e \not{\partial} L_e + i\bar{R}_e \not{\partial} R_e + i\bar{L}_u \not{\partial} L_u + i\bar{R}_u \not{\partial} R_u + i\bar{R}_d \not{\partial} R_d \\ & + \; g(J_W^{\mu+} W_\mu^+ + J_W^{\mu-} W_\mu^- + J_Z^\mu Z_\mu) + e J_{EM}^\mu A_\mu, \end{aligned} \tag{1.55}$$

where

$$J_W^{\mu+} = \frac{1}{\sqrt{2}}(\bar{\nu}_L \gamma^\mu e_L + \bar{u}_L \gamma^\mu d_L), \quad J_W^{\mu-} = \frac{1}{\sqrt{2}}(\bar{e}_L \gamma^\mu \nu_L + \bar{d}_L \gamma^\mu u_L), \tag{1.56}$$

$$\begin{aligned} J_Z^\mu = \frac{1}{\cos\theta_w} \Big[& \bar{\nu}_L \gamma^\mu (\tfrac{1}{2}) \nu_L + \bar{e}_L \gamma^\mu (-\tfrac{1}{2} + \sin^2\theta_w) e_L + \bar{e}_R \gamma^\mu (\sin^2\theta_w) e_R \\ & + \bar{u}_L \gamma^\mu (\tfrac{1}{2} - \tfrac{2}{3}\sin^2\theta_w) u_L + \bar{u}_R \gamma^\mu (-\tfrac{2}{3}\sin^2\theta_w) u_R \\ & + \bar{d}_L \gamma^\mu (-\tfrac{1}{2} + \tfrac{1}{3}\sin^2\theta_w) d_L + \bar{d}_R \gamma^\mu (\tfrac{1}{3}\sin^2\theta_w) d_R \Big] \quad \text{and} \end{aligned} \tag{1.57}$$

$$J_{EM}^\mu = \bar{e}\gamma^\mu(-1)e + \bar{u}\gamma^\mu(+\tfrac{2}{3})u + \bar{d}\gamma^\mu(-\tfrac{1}{3})d. \tag{1.58}$$

Note that the current J_{EM}^μ associated with the photon field is indeed the standard electromagnetic current.

In many books the couplings to the fermion are written in an explicit way, i.e. by using the projection operators, defined as

$$j_{R/L}^\mu \equiv \bar{f}\gamma^\mu \left(\frac{1 \pm \gamma^5}{2} \right) f, \tag{1.59}$$

where f stands for e, ν, u and d. $J_W^{\mu+}$ and $J_W^{\mu-}$ are

$$J_W^{\mu+} = \frac{1}{\sqrt{2}} \left[\bar{\nu}\gamma^\mu \left(\frac{1-\gamma^5}{2} \right) e + \bar{u}\gamma^\mu \left(\frac{1-\gamma^5}{2} \right) d \right], \tag{1.60}$$

$$J_W^{\mu-} = \frac{1}{\sqrt{2}} \left[\bar{e}\gamma^\mu \left(\frac{1-\gamma^5}{2} \right) \nu + \bar{d}\gamma^\mu \left(\frac{1-\gamma^5}{2} \right) u \right]. \tag{1.61}$$

$$\tag{1.62}$$

J_Z^μ can be simplified by using the coefficients for the axial current c_A^f and the vector current c_V^f, defined in Tab. 1.4.

[10] In general, for an operator P one has $\not{P} = \gamma^\mu P_\mu$.

Fermions f	c_V^f	c_A^f
ν	$+\frac{1}{2}$	$+\frac{1}{2}$
e	$-\frac{1}{2}+2\,\sin^2\theta_w$	$-\frac{1}{2}$
u	$+\frac{1}{2}-\frac{4}{3}\,\sin^2\theta_w$	$+\frac{1}{2}$
d	$-\frac{1}{2}+\frac{2}{3}\,\sin^2\theta_w$	$-\frac{1}{2}$

Table 1.4: Coefficients for the axial- and vector-currents of the 1st Generation.

With these coefficients the following very simple expression is obtained

$$J_Z^\mu = \sum_{f=\nu,e,u,d} \bar{f}\gamma^\mu \left(\frac{c_V^f - c_A^f\gamma^5}{2}\right) f. \tag{1.63}$$

With this notation it should be now clear why the electroweak theory is a so-called V-A theory. In Tab. 1.5 all the couplings of the fermions to the gauge bosons are summarized; the propagator terms of the gauge bosons are also added. They can be computed using path integral methods [4].

Coupling Terms			Propagator Terms		
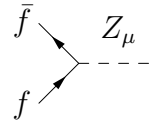	$\widehat{=}$	$\frac{-ig}{2\cos\theta_w}\gamma^\mu\left(c_V^f - c_A^f\gamma^5\right)$	μ ---Z---ν $\longrightarrow$ p	$\widehat{=}$	$\frac{-i}{p^2-m_Z^2}\left(g^{\mu\nu}-\frac{p^\mu p^\nu}{p^2-m_Z^2}\right)$
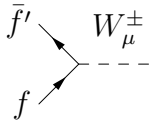	$\widehat{=}$	$\frac{-ig}{2\sqrt{2}}\gamma^\mu\,(1-\gamma^5)$	μ ---$W^\pm$---ν $\longrightarrow$ p	$\widehat{=}$	$\frac{-i}{p^2-m_W^2}\left(g^{\mu\nu}-\frac{p^\mu p^\nu}{p^2-m_W^2}\right)$
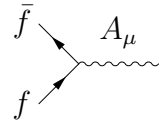	$\widehat{=}$	$-ieQ\gamma^\mu$	μ ~~~γ~~~ν $\longrightarrow$ p	$\widehat{=}$	$\frac{-ig^{\mu\nu}}{p^2}$

Table 1.5: Couplings of fermions to gauge bosons and its propagator terms for the GSW theory.

1.4 Quantum Chromodynamics

The discovery of many new strongly interacting particles in high energy worldwide experiments lead to, in 1964, the so-called quark model. The independent proposals of Gell-Mann and Zweig [24], were able to explain many results. A major prediction was that a particle (named by Gell-Mann as the omega-minus), with an isotopic singlet spin = 3/2, mass of roughly

1 680 MeV and stable to strong decay, should exist. It was therefore a major triumph for the scheme when the Ω^- was discovered in 1964 by a team of physicists from Brookhaven, using the 80-inch bubble chamber [25].

Despite their initial success, they were confronted with some problems. The Ω^- appeared to be symmetric under the interchange of two identical quarks, contradicting the antisymmetric nature of the fermions. To correct these, they had to introduce a new quantum number, the color [11] in order to keep the Pauli exclusion principle [27].

An experimental evidence for color came from the ratio measurement R of different $q\bar{q}$ resonances.

$$R := \frac{\sigma(e^+e^- \to \text{hadrons})}{\sigma(e^+e^- \to \mu^+\mu^-)} = \frac{\sum_f \sigma(e^+e^- \to q_f\bar{q}_f)}{\sigma(e^+e^- \to \mu^+\mu^-)} = 3 \cdot \sum_f Q_f^2, \tag{1.64}$$

where Q_f^2 is the electric charge of the quarks and f runs over the produceable [12] quarks. Here the 3-valued color charge provides a factor of 3, consistent with theoretical values. In Fig. 1.5 the cross-section of the reaction $e^+e^- \to$ hadrons, normalized to $e^+e^- \to \mu^+\mu^-$, as a function of the center-of-mass (CM) energy ($\sqrt{s}$) is shown.

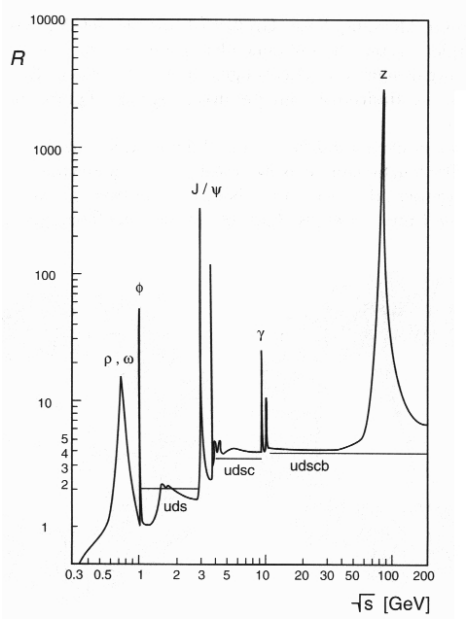

Figure 1.5: Cross-section of the reaction $e^+e^- \to$ hadrons, normalized to $e^+e^- \to \mu^+\mu^-$, as a function of the CM energy ($\sqrt{s}$). The horizontal lines correspond to $R = 6/3$, $R = 10/3$ and $R = 11/3$ [28].

[11] Obviously the particles aren't colored, but they have an additional quantum number with three different states. R.P. Feynman said: "The idiot physicists, unable to come up with any wonderful Greek words anymore, call this type of polarization by the unfortunate name of "color", which has nothing to do with color in the normal sense." [26]

[12] The invariant mass of the resonance $M(q\bar{q})$ must be smaller than the CM energy.

The assignment of color states led to the postulate that, one only observes combinations of quarks that are colorless. The mathematical description of all that led to describe the strong interaction by using a color SU(3) group. The corresponding quantum numbers are conventionally labeled as red, green and blue, whereas the anti-colors are anti-red, anti-green and anti-blue. Suppressing for a moment the spin and flavor quantum numbers, the quarks can be represented by q_i with $i = 1, 2, 3$ the color index. So the only simple combinations allowed are

$$\bar{q}^i q_i, \quad \epsilon^{ijk} q_i q_j q_k \quad \text{and} \quad \epsilon_{ijk} \bar{q}^i \bar{q}^j \bar{q}^k, \tag{1.65}$$

due to the assumption that physical hadrons are singlets. They can be identified as Mesons ($\bar{q}^i q_i$), Baryons ($\epsilon^{ijk} q_i q_j q_k$) and Anti-Baryons ($\epsilon_{ijk} \bar{q}^i \bar{q}^j \bar{q}^k$).

1.4.1 QCD Lagrangian

Now we can benefit from the derivations done in section 1.3.1, and can write down immediately the Lagrangian for a SU(3) symmetry group

$$\mathcal{L}_{\text{QCD}} = \sum_q \bar{q}_i (i \not{D}_\mu - m_q)_{ij} q_j - \frac{1}{4} F^a_{\mu\nu} F^{\mu\nu\, a}. \tag{1.66}$$

The field strength tensor $F^a_{\mu\nu}$ and the covariant derivative D_μ are given by the following expressions

$$F^a_{\mu\nu} = \partial_\mu A^a_\nu - \partial_\nu A^a_\mu - g_s f^{abc} A^b_\mu A^c_\nu \tag{1.67}$$

$$(D_\mu)_{ij} = \delta_{ij} \partial_\mu + i g_s T^a_{ij} A^a_\mu \tag{1.68}$$

$$(m_q)_{ij} = \delta_{ij} m_q, \tag{1.69}$$

where A^a_μ are the gluon fields, g_s the gauge coupling, f^{abc} the structure constants and T^a_{ij} the generators of the Lie group, which define the gauge symmetry. The free parameters of the theory are the mass terms and coupling constant. To complete the structure the eight generators of the SU(3) group are given here, the so-called Gell-Mann matrices λ_a, where $T^a = \lambda_a/2$,

$$\lambda_1 = \begin{bmatrix} 0 & 1 & 0 \\ 1 & 0 & 0 \\ 0 & 0 & 0 \end{bmatrix} \quad \lambda_2 = \begin{bmatrix} 0 & -i & 0 \\ i & 0 & 0 \\ 0 & 0 & 0 \end{bmatrix} \quad \lambda_3 = \begin{bmatrix} 1 & 0 & 0 \\ 0 & -1 & 0 \\ 0 & 0 & 0 \end{bmatrix} \quad \lambda_4 = \begin{bmatrix} 0 & 0 & 1 \\ 0 & 0 & 0 \\ 1 & 0 & 0 \end{bmatrix}$$

$$\lambda_5 = \begin{bmatrix} 0 & 0 & -i \\ 0 & 0 & 0 \\ i & 0 & 0 \end{bmatrix} \quad \lambda_6 = \begin{bmatrix} 0 & 0 & 0 \\ 0 & 0 & 1 \\ 0 & 1 & 0 \end{bmatrix} \quad \lambda_7 = \begin{bmatrix} 0 & 0 & 0 \\ 0 & 0 & -i \\ 0 & i & 0 \end{bmatrix} \quad \lambda_8 = \frac{1}{\sqrt{3}} \begin{bmatrix} 1 & 0 & 0 \\ 0 & 1 & 0 \\ 0 & 0 & -2 \end{bmatrix} \tag{1.70}$$

The structure constant of the group, $f^{abc} = f_{abc}$, defined through the commutation relations

$$[T^a, T^b] = i f^{abc} T^c, \tag{1.71}$$

are totally antisymmetric in their indices. For SU(3) the non-vanishing values are

$$\begin{aligned} f_{123} &= 1, \\ f_{458} &= f_{678} = \sqrt{3}/2 \\ f_{147} &= f_{165} = f_{246} = f_{345} = f_{376} = f_{257} = 1/2, \end{aligned} \tag{1.72}$$

with implied permutations of the indices. A more intuitive representation of the QCD Lagrangian is given in Fig. 1.6.

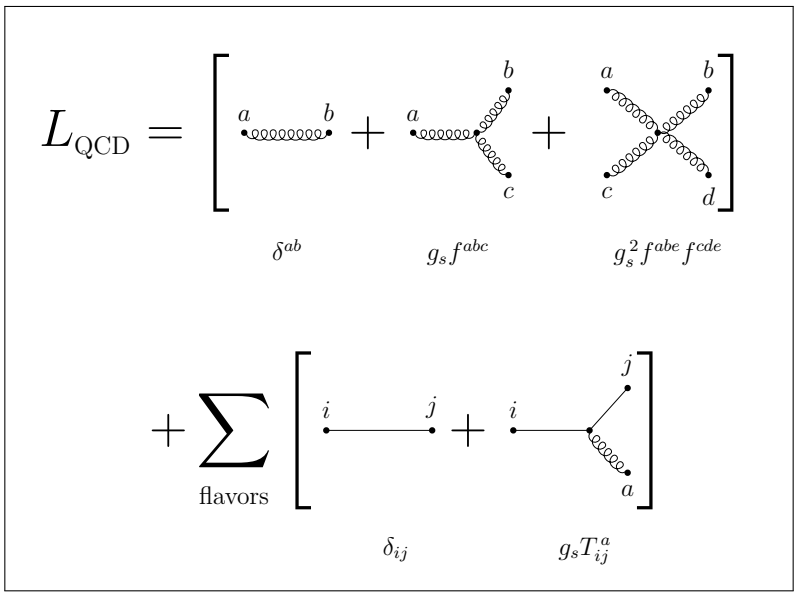

Figure 1.6: Pictorial representation of the QCD Lagrangian [29].

1.5 Experimental Parameters

In this section some experimental parameters will be introduced. The use of QCD to describe high energy collisions implies the use of perturbative QCD (pQCD). The running of the strong coupling constant is the reason why pQCD works. Since we are colliding protons, which are made of quarks and gluons, we have to know how the proton momentum is distributed over its constituents, the partons. This is parametrized by the parton distribution functions, which will be briefly discussed within this section. The considered final state for this work is a electron/positron pair. The cross-section for such a production, will be derived at the end.

1.5.1 The Running of the Strong Coupling Constant

In perturbative field theories one usually has to include the calculation of loop-diagrams to get physical amplitudes. As shown in Appendix B for the QED case, these loops are divergent. To get a finite result, the so-called renormalization technique is used. Within this procedure the

divergent terms are removed by counter terms at some specific renormalization scale μ_R. The theory is defined by physical parameters like the masses and the couplings. These quantities can be measured experimentally.

In general, the choice of this scale is arbitrary, since one requires that the observable quantities are independent of the μ_R in each order.

A dimensionless observable R is considered, so that in all the scales Q in which one is interested, any other scale is small (e.g., $m_q^2/Q^2 \ll 1$). The independence of $R = R\big(Q/\mu_R, \alpha_s(\mu_R)\big)$ from μ_R is expressed by the Callan-Symanzik equation

$$\left(\mu_R \frac{\partial}{\partial \mu_R} + \beta(g_s)\frac{\partial}{\partial g_s}\right) R = 0 \tag{1.73}$$

with g_s the QCD coupling constant. The β-function $\beta(g_s)$ can be expanded in orders of the coupling constant

$$\beta(g_s) = -\frac{g_s^3}{(4\pi)^2} b_0 + \mathcal{O}(g_s^5). \tag{1.74}$$

For the SU(3) group b_0 is

$$b_0 = (11 - \frac{2}{3} n_f), \tag{1.75}$$

where n_f is the number of light quarks compared to the scale Q. The scale dependence can be absorbed into a running coupling constant $\alpha_s(Q)$ defined as

$$\alpha_s(Q) = \frac{\bar{g}_s^2}{4\pi}, \tag{1.76}$$

where $\bar{g}_s$ is the renormalized coupling defined by the Renormalization Group Equation (RGE)

$$\frac{d}{d\log(Q/\mu_R)} \bar{g}_s = \beta(\bar{g}_s). \tag{1.77}$$

The solution of the RGE is

$$\alpha_s(Q) = \frac{\alpha_s}{1 + \frac{\alpha_s b_0}{2\pi} \log(Q/\mu_R)}. \tag{1.78}$$

Defining the scale parameter Λ as

$$1 = \frac{\bar{g}_s b_0}{8\pi^2} \log(\mu_R/\Lambda), \tag{1.79}$$

the running coupling constant becomes then independent of the running coupling constant $\bar{g}_s$

$$\alpha_s(Q) = \frac{2\pi}{b_0} \frac{1}{\log(Q/\Lambda)}. \tag{1.80}$$

One can immediately see that α_s depends on the sign of b_0. If the β-function is negative (b_0 positive), the coupling constant decreases when Q becomes larger. This effect is known as asymptotic freedom and appears in QCD as long as b_0 is positive, with Eq. (1.75) i.e., $n_f < 17$. Currently the total number of known quarks is 6. One can therefore safely argue

that, if the process scale Q is large compared to Λ, the coupling constant is small and one can apply perturbative calculations. On the other hand, if Q becomes small, i.e., at the order of Λ, the perturbative description is no longer valid. Experimentally it was found that Λ is $\sim 200\,\mathrm{MeV}$, corresponding to a distance of $d = 1/\Lambda \approx 1\,\mathrm{fm}$, the size of a hadron. In other words, Λ respectively, d is the scale respectively, distance at which the strong interaction actually becomes "strong".

As the RGE determines only the evolution of the coupling constant, its normalization has to be measured experimentally. Normally the scale is chosen to be the Z boson mass m_Z. The value reported by [5] is

$$\alpha_s(m_Z) = 0.1184 \pm 0.0007. \tag{1.81}$$

1.5.2 Parton Distribution Functions

Hadrons colliding at very high energy, mostly involve only soft interactions of the constituent quarks and gluons. These events cannot be treated using perturbative QCD, because α_s is large when the momentum transfer is small. Nevertheless in some collisions, the interesting ones, two partons will exchange a large momentum p_t perpendicular ($t$ransverse) to the collision axis. The parton momenta are collinear to the hadron momentum and each constituent carries a fraction x of the hadron momentum. This model is known as the parton model and is described in [30]. Here, the interaction takes place very rapidly compared to the internal time scale of the hadron wavefunctions, so the lowest order QCD prediction should describe the processes. A schematic diagram for such a collision is shown in Fig. 1.7.

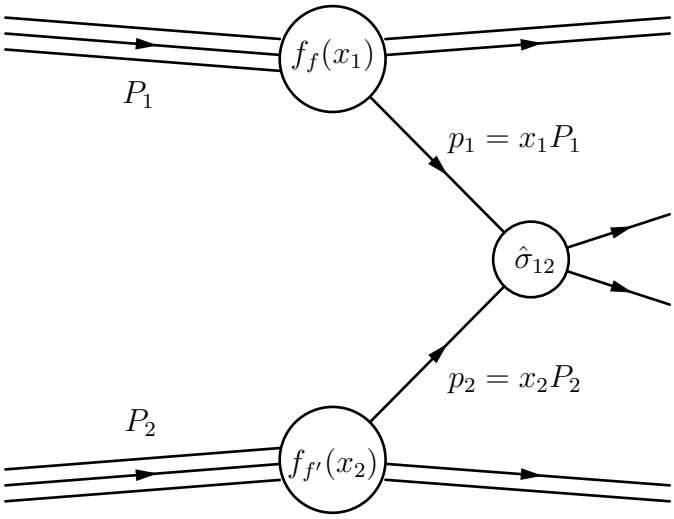

Figure 1.7: Schematic diagram for a proton-proton interaction at high energies.

With this model, the following notation for proton-proton collisions can be used. Assuming the incoming hadrons to have four momenta $P_{1,2}$ and that the energy compared to the hadron masses are large enough to be neglected, i.e.,

$$m^2_{P_{1,2}} = P^2_{1,2} \equiv 0, \tag{1.82}$$

the momenta of the interacting partons $p_{1,2}$ are than

$$p_i = x_i P_i \quad \text{with} \quad i = 1, 2 \tag{1.83}$$

wherein $x_i \in [0, 1]$ is the fraction of the hadron momentum carried by the partons. The CM energy squared of the proton-proton system is defined as

$$s = (P_1 + P_2)^2, \tag{1.84}$$

with the parton-parton CM energy squared as

$$\begin{aligned} \hat{s} &= (p_1 + p_2)^2 = (x_1 P_1 + x_2 P_2)^2 \\ &= x_1 x_2 s. \end{aligned} \tag{1.85}$$

The only variable one still needs to compute for the parton momenta is the variable x. Since the distribution of this variable x, the so-called Parton Distribution Functions (PDF) depends on the soft interactions within the hadrons, it cannot be derived using perturbative QCD. The PDF $f_q(x)$ can be defined where $f_q(x)\,dx$ is the probability of finding a parton of type f, that carries a fraction within $[x, x + dx]$ of the hadron momentum. The parton of type f can be any quark or anti-quark flavor and also a gluon. Obviously if one sums up all constituents of the hadron, one gets

$$\sum_q \sum_g \int_0^1 dx\, x f_{q/g}(x) = 1. \tag{1.86}$$

There are some other constraints on the PDFs due to the quantum numbers of the hadrons. In the case of the proton, which is a bound state of uud quarks and some quark anti-quark pairs, it should contain an excess of two (u)p quarks and one (d)own quark over the corresponding anti-quarks. These considerations imply the constraints

$$\begin{aligned} \int_0^1 dx \left(f_u(x) - f_{\bar{u}}(x)\right) &= 2 \quad \text{and} \\ \int_0^1 dx \left(f_d(x) - f_{\bar{d}}(x)\right) &= 1. \end{aligned} \tag{1.87}$$

These rules can be used to constrain the distributions using experimental deep inelastic scattering data. How to do that in detail, can be found in [31].

We now have everything needed to define the hadronic cross-section for a proton-proton process ($pp \to X$) as

$$\sigma_{pp\to X} = \sum_{qq'} \int_0^1 dx_1 \int_0^1 dx_2 f_q(x_1) f_{q'}(x_2) \hat{\sigma}(x_1, x_2, s), \tag{1.88}$$

with $\hat{\sigma}$ the partonic hard scattering cross-section and the sum running over all parton pairs qq' that contribute to the process. A set of distribution functions, chosen to fit all available data for $Q^2 = 10\,(\text{GeV})^2$ (left) and $Q^2 = 10^4\,(\text{GeV})^2$ (right), is shown in Fig. 1.8.

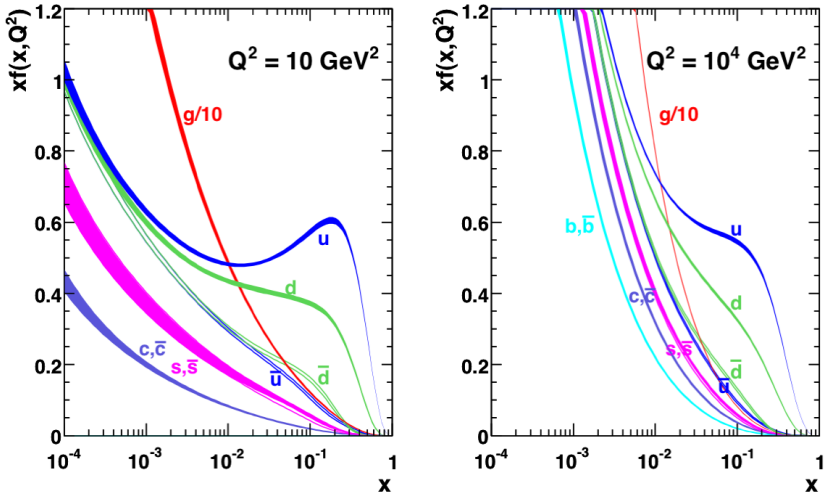

Figure 1.8: Parton distribution functions for quarks, anti-quarks and gluons in the proton at $Q^2 = 10\,(\mathrm{GeV})^2$ (left) and $Q^2 = 10^4\,(\mathrm{GeV})^2$ (right). These distributions are obtained from fits to deep inelastic scattering data performed by the MSTW collaboration, described in [32].

1.5.3 Lepton Pair Production

For lepton pair production, the simplest case is the reaction in which a high mass lepton pair l^+l^- (e.g., e^+e^-) emerges from a $q\bar{q}$ annihilation. A Feynman diagram can be found in Fig. 1.9.

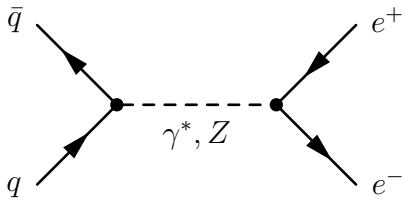

Figure 1.9: Leading order Feynman diagram for the $q\bar{q} \to e^+e^-$ process.

In this case, the underlying $q\bar{q}$ reaction is described by an elementary QED cross-section. In the leading order in QCD, the cross-section needed $\hat{\sigma}(q\bar{q} \to e^+e^-)$ is related to the cross-section of the inverted process

$$\sigma(e^+e^- \to q\bar{q}) = 3\sum_q Q_q^2 \cdot \sigma_0, \tag{1.89}$$

where the sum is taken over the quark flavors and σ_0 is the QED cross-section for $e^+e^- \to \mu^+\mu^-$,

$$\sigma_0 = \frac{4\pi\alpha^2}{3s}. \tag{1.90}$$

The only difference found in this cross-section is that one must average out rather than sum up over the color of the quark anti-quark pair. So one obtains

$$\hat{\sigma}(q\bar{q} \to e^+e^-) = \frac{1}{3}Q_q^2 \cdot \frac{4\pi\alpha^2}{3\hat{s}}. \tag{1.91}$$

Assuming that both final-state momenta are given, it is possible to reconstruct the 4-momentum q of the interacting boson. Let

$$m^2_{\gamma^*,Z} \equiv m^2 = q^2 \tag{1.92}$$

be the square of the invariant mass. The longitudinal momentum of the boson using the rapidity Y, can be parametrized as

$$q^0 = m \cosh Y. \tag{1.93}$$

Ignoring the small transverse momenta of the constituent quark and anti-quark, one can then write in the proton-proton CM frame

$$P_1 = (E, 0, 0, E), \quad P_2 = (E, 0, 0, -E), \tag{1.94}$$

where E satisfies $s = 4E^2$, and

$$q = x_1 P_1 + x_2 P_2 = \big((x_1 + x_2)E, 0, 0, (x_1 - x_2)E\big). \tag{1.95}$$

Rewriting Eq. (1.85) using Eq. (1.92) one finds

$$m^2 = x_1 x_2 s. \tag{1.96}$$

Similarly, using Eq. (1.93) one finds

$$\cosh Y = \frac{x_1 + x_2}{2\sqrt{x_1 x_2}} = \frac{1}{2}\left(\sqrt{\frac{x_1}{x_2}} + \sqrt{\frac{x_2}{x_1}}\right), \tag{1.97}$$

which implies

$$\exp Y = \sqrt{\frac{x_1}{x_2}}. \tag{1.98}$$

One can invert this equation to determine x_1 and x_2

$$x_1 = \frac{m}{\sqrt{s}}\, e^{Y} \quad \text{and} \quad x_2 = \frac{m}{\sqrt{s}}\, e^{-Y}. \tag{1.99}$$

Relations (1.96) and (1.98) let us convert the integral in Eq. (1.88) into an integral over the parameters m^2 and Y of the interacting boson. The Jacobian of the change of variables is

$$\left|\frac{\partial(m^2, Y)}{\partial(x_1, x_2)}\right| = \frac{m^2}{x_1 x_2}. \tag{1.100}$$

The purely QED differential cross-section is therefore

$$\frac{d^2\sigma}{dm^2 dY}(q\bar{q} \to e^+e^-) = \sum_q x_1 f_q(x_1) x_2 f_{\bar{q}}(x_2) \cdot \frac{1}{3} Q_q^2 \cdot \frac{4\pi\alpha^2}{3m^4}, \tag{1.101}$$

where x_1 and x_2 are given by Eq. (1.99).

For high energies, as at the LHC, Eq. (1.101) must be supplemented by the additional contribution from the Z boson exchange, so it becomes

$$\frac{d^2\hat{\sigma}_{q\bar{q}\to e^+e^-}}{dm^2 dY} = \frac{\hat{\sigma}_0}{3\hat{s}} \left[Q_q^2 - 2Q_q c_V^e c_V^q \chi_1(\hat{s}) + \left((c_A^e)^2 + (c_V^e)^2\right)\left((c_A^q)^2 + (c_V^q)^2\right)\chi_2(\hat{s})\right], \tag{1.102}$$

with c_V^f, c_A^f from Tab. 1.4 and

$$\chi_1(\hat{s}) = \kappa \frac{\hat{s}(\hat{s}-M_Z^2)}{(\hat{s}-M_Z^2)^2+\Gamma_Z^2 M_Z^2}, \quad \chi_2(\hat{s}) = \kappa^2 \frac{\hat{s}^2}{(\hat{s}-M_Z^2)^2+\Gamma_Z^2 M_Z^2} \quad \text{and} \quad (1.103)$$

$$\kappa = \frac{\sqrt{2}G_F M_Z^2}{16\pi\alpha}.$$

Here G_F is the Fermi constant, α is the electromagnetic coupling, M_Z and Γ_Z are the mass and total decay width of the Z boson respectively. The χ_2 term comes from the square of the Z exchange amplitude and the χ_1 term from the photon-Z interference. The experimental values are given in Tab. 1.6.

Parameters	G_F [(GeV)$^{-2}$]	m_Z [GeV]	Γ_Z [GeV]
PDG	$1.166\,37(1)\cdot 10^{-5}$	91.187 6(21)	2.495 2(23)

Table 1.6: Set of electroweak constants [5]. The uncertainties in the last digits are given in parentheses.

In Fig. 1.10 the calculated differential cross-section for such a process is shown. It can be deduced from the plot that one can expect a few thousand $Z \to e^+e^-$ events per pb^{-1}.

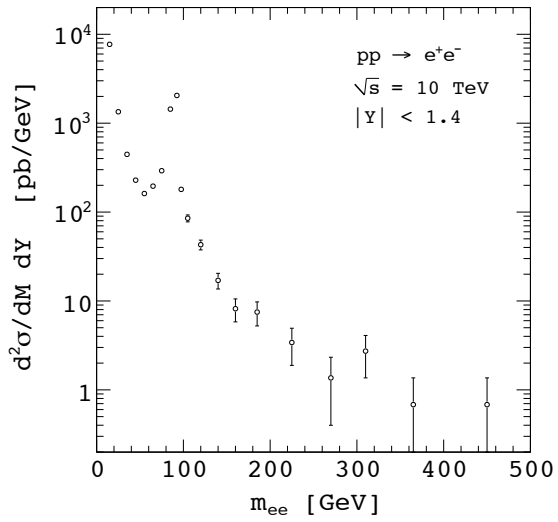

Figure 1.10: Differential cross-section for a $q\bar{q} \to \gamma/Z^* \to e^+e^-$ process.

1.6 Tests and Limits of the Standard Model

We are now in a position where the Standard Model of Particle Physics and the Standard Model of Cosmology can synthesize the understanding of the physical universe.

The theoretical predictions of the SM have been tested and the experimental results found to be in excellent agreement. The predicted and experimental values for some additional parameters of the SM, not previously shown, are summarized in Tab. 1.7.

Variable	Experimental Value	SM Prediction
m_t [GeV]	173.1 ± 1.3	173.2 ± 1.3
m_W [GeV]	80.420 ± 0.031	80.384 ± 0.014
σ_{had} [nb]	41.541 ± 0.037	41.484 ± 0.008

Table 1.7: Experimentally observed values compared to the SM best fit predictions. σ_{had} is the hadronic cross-section in electron-positron annihilation with a CM energy corresponding to the Z boson mass. For details see [5].

One of the most precisely known parameters is the Landé-factor g, related to the magnetic moment of the electron. The agreement between theoretical values and experimental measurements of this factor, is up to eight significant digits. Together with other experiments, one can state that the QED is the most precisely known physical theory.

However, the SM is not complete. One missing piece is the Higgs boson. To date, no experiment was able to find this particle, which would complete the SM. It not only gives rise to the masses of the W and Z bosons, but also serves as the origin of the masses for the fermions.

The SM predicts some important quantities of the Higgs boson, but not the mass. However, with theoretical calculations and the measurement of electroweak parameters an upper limit can be set at $m_H \leq 194\,\text{GeV}$ with 95% CL [5]. This prediction also includes the lower bound from direct searches of $m_H \geq 114.4\,\text{GeV}$ at 95% CL [33].

Only 5% of the universe is made of matter, such as quarks and leptons. We think therefore that another missing element may be so-called Dark Matter (DM) and could account for up to 25% of the universe. DM is believed to play a central role in structure formation and galaxy evolution, and has measurable effects on the anisotropy of the Cosmic Microwave Background Radiation (CMBR). The first indication of DM was made in the early 1933 by the Swiss physicist Fritz Zwicky [34]. He discovered that numerous galaxies in the Coma cluster were moving too fast and the gravitational force was insufficient to balance the outward "centrifugal force" of the matter. All suggesting that galaxies, clusters of galaxies, and the universe as a whole contain far more matter than what is known by now. We believe that the rest of the universe is made up of the so-called Dark Energy (DE). In cosmology DE is the most popular way to explain recent observations that the universe appears to be expanding at an accelerating rate [35].

The universe is made almost entirely of matter and not antimatter. The laws of physics tells us that at the beginning of the universe, there was an equal amount of matter and antimatter. What happened with the antimatter? We do not know, yet.

In the SM there are matter particles, called fermions and particles carrying the force called bosons. The present description treats the fermions and bosons very differently. SUSY (SUper-

SYmmetry) is the new idea that the fundamental theory actually treats fermions and bosons in a fully symmetric way. If nature is indeed supersymmetric, then the supersymmetric particles should exist and some of them could be detected at LHC. One of these new particles, the so-called LSP (Lightest Supersymmetric Particle) could be a good candidate for DM [36].

Despite the success of the SM, it has been agreed upon by a major part of the scientific community that there has to be some new physics beyond the SM, and that this new physics should show up around 1 TeV. The fact that almost all proposed models predict the existence of new particles, gives hope that the upcoming collider experiments at the LHC will shed light on this new domain.

In this chapter the Standard Model of Particle Physics was introduced, with the electroweak theory and the QCD, as two gauge theories describing the particle interactions. At the end of the chapter some experimental parameters were introduced and the limits of the theory were discussed. In the next chapter the collider, LHC, and the multi-purpose detector, CMS, will be described.

Chapter 2

The Collider Experiment

No amount of experimentation can ever prove me right;
a single experiment can prove me wrong.
- Albert Einstein [37]

The Compact Muon Solenoid (CMS) is one of the four major experiments currently being undertaken at the Large Hadron Collider (LHC) at the European Organization for Nuclear Research (CERN). CMS and ATLAS (A Toroidal LHC ApparatuS) are two universal purpose built detectors, designed to cover the whole range of possible high energy particle physics fenomena. The LHCb (Large Hadron Collider beauty) and ALICE (A Large Ion Collider Experiment) are smaller detectors built for specific physics topics. ALICE is a heavy ion detector built to exploit the unique physics potential of nucleus-nucleus interactions and the LHCb experiment is built for precise measurements of the CP violation and rare decays.

In this chapter we start with a brief presentation of the LHC accelerator. Then an explanation of the principles of a high energy particle physics detector follows. Then, the CMS detector will be explained in detail and we will elaborate on the Electromagnetic Calorimeter (ECAL). Lastly, we will highlight the importance of the computing structure for such an experiment.

2.1 Large Hadron Collider

The LHC is the most energetic accelerator in the world and was built in the tunnel of the LEP (Large Electron Positron) collider. The tunnel has a circumference of about 26.7 km and is 100 m underground. It straddles the Swiss and French borders on the outskirts of Geneva, as shown in Fig. 2.1.

On September 11^{th} 2008, the first beams circulated in the LHC. Unfortunately an incident, in the LHC, resulted in a year long repair. On November 23^{rd}, 2009 the first collisions at 900 GeV became available. Fig. 2.2 shows an event display of one of the first colliding events measured with the CMS detector.

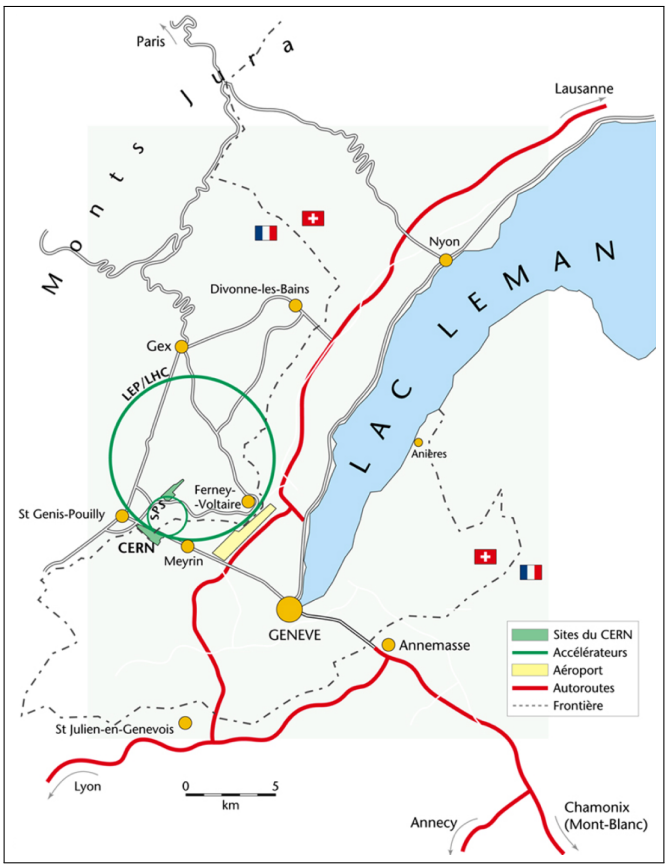

Figure 2.1: Map of the Geneva region and of the LHC [38].

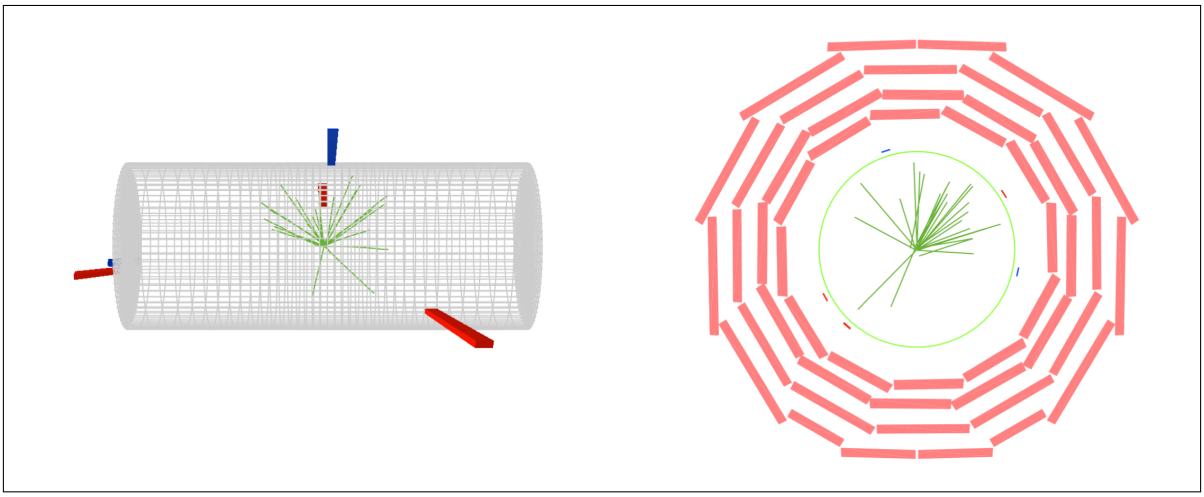

Figure 2.2: First event measured at 900 GeV and no magnetic field with CMS. Left shows the 3D view and right the ρ-ϕ view.

A few months later, on March 30$^{\text{th}}$ 2010, the first collisions at 7 TeV occurred. Fig. 2.3 shows an event display of one such high energy collision event measured and reconstructed with the CMS detector.

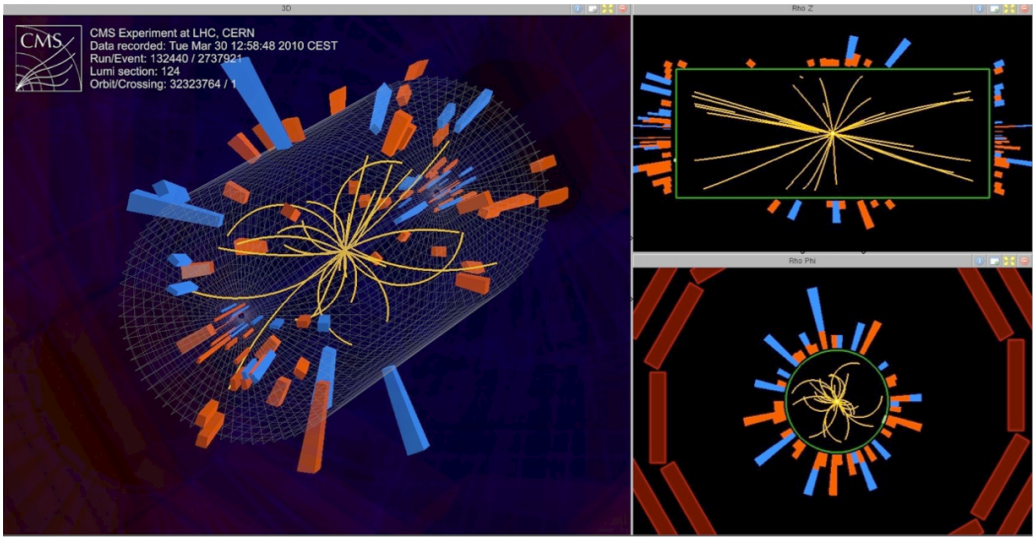

Figure 2.3: A 7 TeV event recorded with CMS. Left shows the 3D view, upper right the ρ-z view and lower right the ρ-ϕ view.

2.1.1 The Machine Parameter

The most important parameters for a collider are the beam energy and the luminosity. The LHC is at the edge of the energy frontier as illustrated in the Livingston plot shown in Fig. 2.4.

The limitation on the energy for a proton accelerator storage ring is the maximum magnetic field to bend the particles, i.e.,

$$\begin{aligned} F_L = qvB &\stackrel{!}{=} \frac{mv^2}{R} = F_C \\ \Rightarrow p &= qBR. \end{aligned} \tag{2.1}$$

Multiplying both sides with c gives

$$\begin{aligned} pc &= qcBR \\ pc &\approx 1.6 \cdot 10^{-19}\,\text{As} \cdot 3 \cdot 10^{8}\,\text{m/s} \cdot B \cdot R \end{aligned} \tag{2.2}$$

With $1\,\text{J} = \frac{1\text{eV}}{1.6 \cdot 10^{-19}}$ the well known relation

$$R\,[\text{m}] \approx \frac{p\,[\text{GeV}]}{0.3 \cdot B\,[\text{T}]} \tag{2.3}$$

is found. Now it is possible to calculate the maximum beam energy. The dipoles do not fill all of the 26.7 km of the ring, but only a fraction of it. This is due to the fact that a lot of other devices

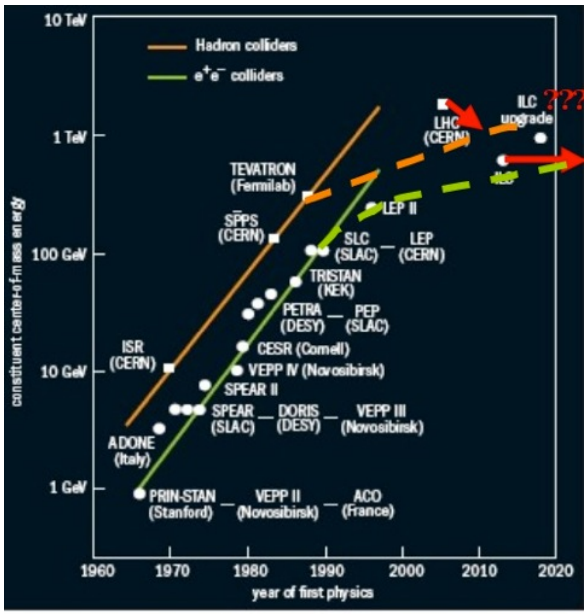

Figure 2.4: Livingston plot showing the energy in the constituent frame of electron-positron and hadron colliders. The energy of hadron colliders has been derated by factors of 6-10, due to the fact that the proton energy is shared among its quarks and gluons [39].

are necessary: injectors, vacuum pumps, multipole magnets, radio-frequency (RF) cavities, high voltage instruments, measurement equipment, and, obviously, the enormous detectors. There are 1 232 dipoles, each one having a magnetic length of 14.3 m, totaling 17 618 m. With the magnetic field of $B = 8.33\,\mathrm{T}$, the maximum energy per beam is 7 TeV.

Once it is possible to reach very high energies in the beams, the luminosity will be maximized. The luminosity is a measurement of the number of collisions that can be produced in a detector per square centimeter and per second. The luminosity $\mathcal{L}$ is

$$\mathcal{L} = \frac{n_b N_1 N_2 f_{rev}}{A_t^{eff}}, \tag{2.4}$$

where

- n_b is the number of bunches in one beam,
- N_i is the number of particles in each bunch ($i = 1, 2$),
- f_{rev} is the revolution frequency and
- $A_t^{eff} = 4\pi\sigma_x\sigma_y$ is the effective[1] transverse area of the beam, where $\sigma_{x,y}$ is the standard deviation of the particle distribution in the beam.

For the LHC the values are listed in Tab. 2.1. The number of collisions per second, achieved

[1] Effective, because the beam profile does not have a sharp edge.

Parameters	Design	Startup [2]
n_b	2 808	1
N_i	10^{11}	10^9
f_{rev}	10^4 Hz	10^4 Hz
A_t^{eff}	10^{-5} cm^2	10^{-2} cm^2
$\mathcal{L}$	10^{-34} cm^{-2}s^{-1}	10^{-24} cm^{-2}s^{-1}

Table 2.1: LHC luminosity parameter for design and startup (first days) condition.

in the design configuration can be calculated. A measurement of the probability that an event occurs, i.e. the collision rate $\dot{N}$, is

$$\dot{N} = \mathcal{L} \cdot \sigma \sim 10^9 \,\text{Hz}, \tag{2.5}$$

where $\sigma = 60$ mbarn [3] is the total inelastic proton-proton cross-section [5].

2.1.2 Machine Components

In an accelerator, particles circulate in a vacuum tube and are manipulated using electromagnetic devices: dipole magnets keep the particles in their nearly circular orbits, quadrupole magnets focus the beam, and accelerating cavities are electromagnetic resonators that accelerate particles and then keep them at a constant energy by compensating for energy losses.

The LHC is not a perfect circle. It is made of eight arcs and eight insertions. The arcs contain the dipole bending magnets Fig. 2.5, with 154 in each arc. An insertion consists of a long straight section plus two (one at each end) transition regions.

A sector is defined as the part of the machine between two insertion points. The eight sectors are the working units of the LHC. Powering of each sector is essentially independent. An octant starts from the middle of an arc and ends in the middle of the following arc and thus spans a full insertion (Fig. 2.6).

Magnets

There is a large variety of magnets in the LHC, including dipoles, quadrupoles, sextupoles, octupoles, decapoles, etc. giving a total of about 9 600 magnets. Each type of magnet contributes to optimizing a particle's trajectory. Most of the correction magnets are embedded in the cold mass of the main dipoles and quadrupoles. The LHC magnets have either a twin aperture (for example, the main dipoles), or a single aperture (for example, some of the insertion quadrupoles). Insertion quadrupoles are special magnets used to focus the beam down to the smallest possible size at the collision points, thereby maximizing the chance of two protons

[3] 1 barn $= 10^{-24}$ cm^2

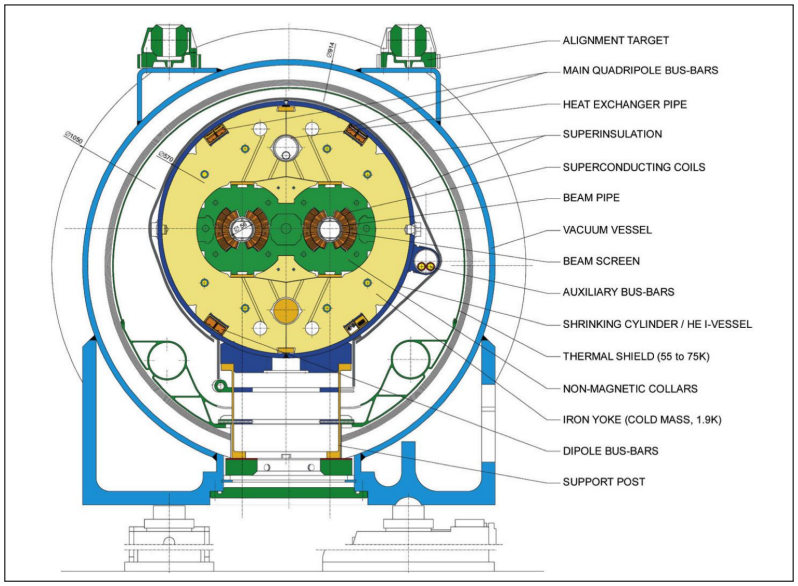

Figure 2.5: Diagram of an LHC dipole magnet [40].

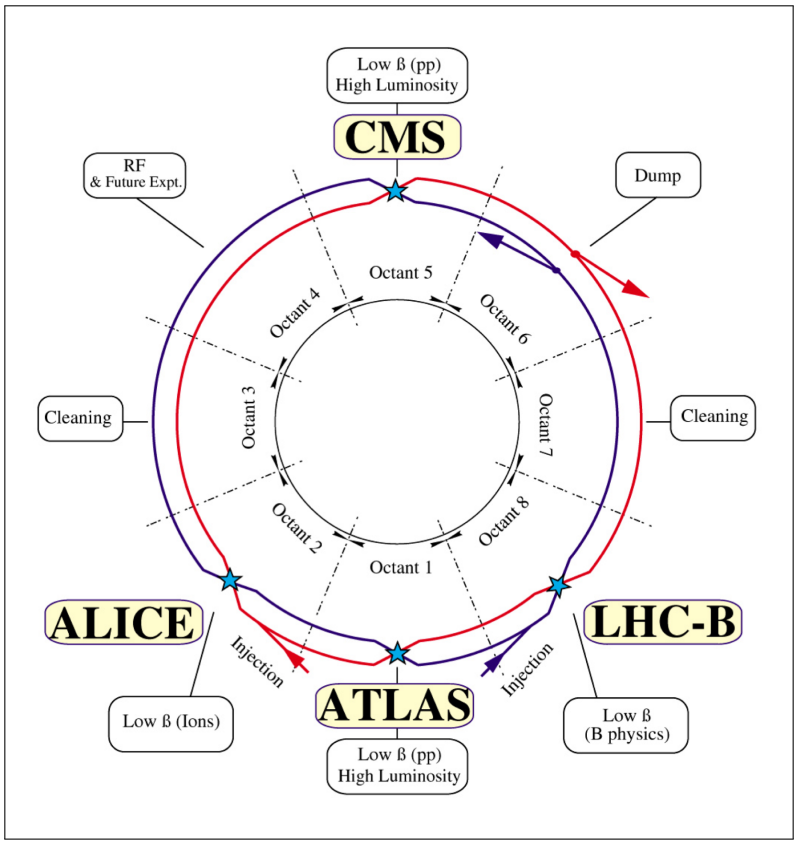

Figure 2.6: LHC layout [41].

smashing head-on into each other. The biggest magnets are the 1 232 dipoles, providing the field of 8.33 T and keep the protons in orbit.

Cavities

The main role of the LHC cavities is to deliver RF power to the beam, during acceleration to the top energy. Superconducting cavities with small energy losses and large stored energy are the best solution. The LHC uses eight cavities per beam, each delivering 2 MV at 400 MHz. The cavities operate at 4.5 K. They also keep the 2 808 proton bunches tightly clustered to ensure high luminosity at the collision points and, hence, maximize the number of collisions.

Collimators

The LHC collimation system protects the accelerator against unavoidable regular and irregular beam loss. Two regions, Interaction Region 3 (IR3) and IR7, are dedicated to beam cleaning. These two cleaning regions house the collimators and will become among the most radioactive areas of LHC.

Dumping System

The LHC beam dumping system is designed to make a fast extraction of the circulating beams from each ring of the collider, with minimal losses. The particles are then transported to external dump blocks, which are located in caverns at the end of a 700 m long vacuum line.

2.2 Generic High Energy Physics Collider Detector

In this section the concept of a high energy physics collider detector will be introduced. A detector has to be able to identify a handful of particles, some of them are charged, some not, and some appear only as so-called jets, i.e. a narrow cone of hadrons and other particles produced by the hadronization of quarks and gluons. In summarizing, it is necessary to identify the following particles:

- electrons and photons,
- hadrons (mainly detected as jets) and,
- muons.

It is impossible to directly "see" a particle. However measuring particles by the way they interact with our detector is feasible, since different particles interact in different ways. In this sense there are two different ways of doing it. The most important signatures of particles are tracker and calorimeter hits. The tracking chambers only measure charged particles. The calorimeters do the opposite: they try to stop everything completely, measuring the energy they absorbed. Therefore the tracker system comes first, and then the calorimeter. With these two components, as illustrated in Fig. 2.7, it is possible to distinguish between photons and electrons. Although both of them are absorbed completely in the calorimeter, only the electrons leave a signature in the tracker. With such a detector only the energy of the particle could be measured.

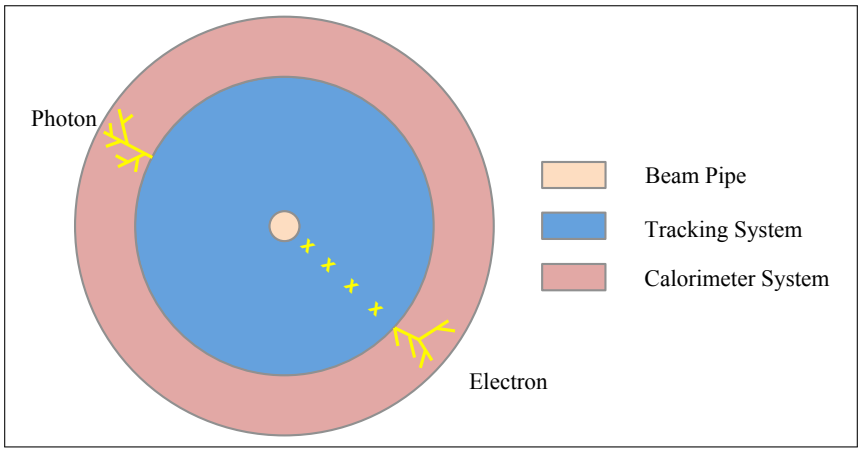

Figure 2.7: Generic particle detector for electromagnetic particles.

To know both the charge of the particle and its momentum one has to measure the trajectory in a magnetic field. This allows one to then calculate the momentum and the charge of the particles. In Fig. 2.8 the bent is insinuated. Thus electrons and positrons, which have the same mass but the opposite charge, can be distinguished. With this detector, the reconstruction of a Z boson decaying into e^+e^- can already be achieved.

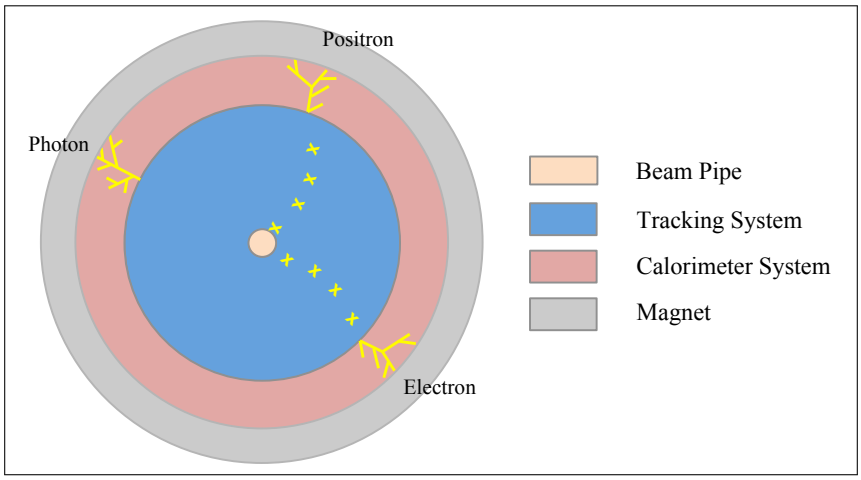

Figure 2.8: Generic particle detector for electromagnetic particles with magnet.

Jets are not only composed of hadrons, but also electrons, positrons and photons can be included. The energy is reconstructed by the calorimeter system and the charge and momentum by the tracker. To be able to distinguish between single isolated electrons and electrons in jets, the calorimeter system is divided into two: an electromagnetic part, for electrons/positrons and photons, and a hadronic part. This distinction is illustrated in Fig. 2.9. Note, the complete calorimeter system is used to reconstruct jets.

The muon, in relation to the detector size, is a long lived particle. That is the reason why the

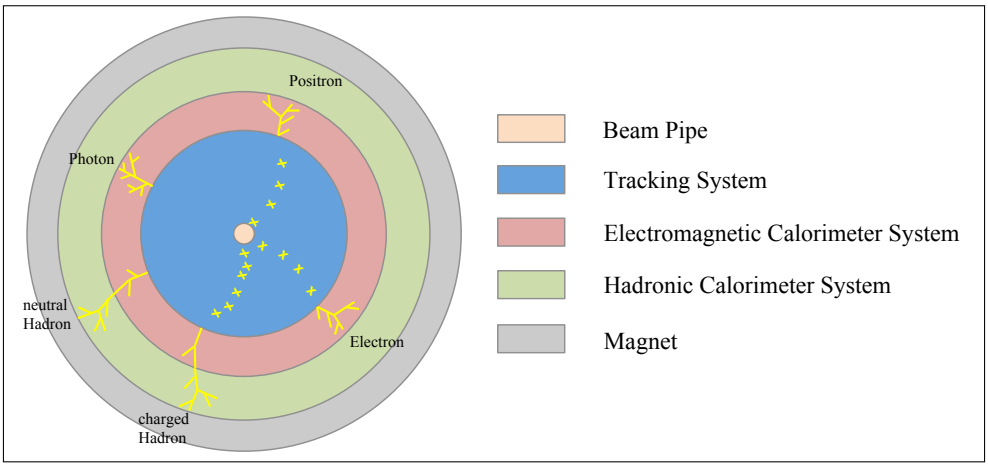

Figure 2.9: Generic particle detector without muon system.

muon system is built on the outermost layer. Particles which leave a signal in this system, are identified as muons. In Fig. 2.10 this is illustrated by a few hits in the muon system.

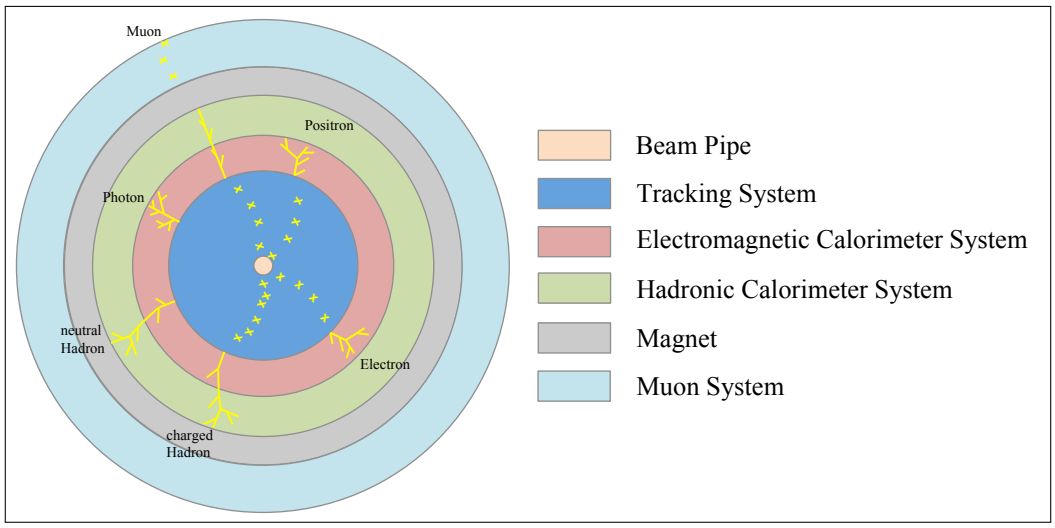

Figure 2.10: Generic particle detector.

The final component in the complete multipurpose detector is a special tracking detector. Some particles live long enough to travel a few milimeters through the detector and then they decay into secondary particles. To be able to reconstruct this so-called secondary vertex, a detector with a very high spatial resolution is needed. This layer lies very close to the beam line and is called the vertex detector, as shown in Fig. 2.11.

To close this section on the generic detector, the concept of missing transverse energy (MET) will be explained. Within the SM there is at least one particle type that does not interact at all with our detector. Even in a perfect detector, the neutrinos can not be detected. The

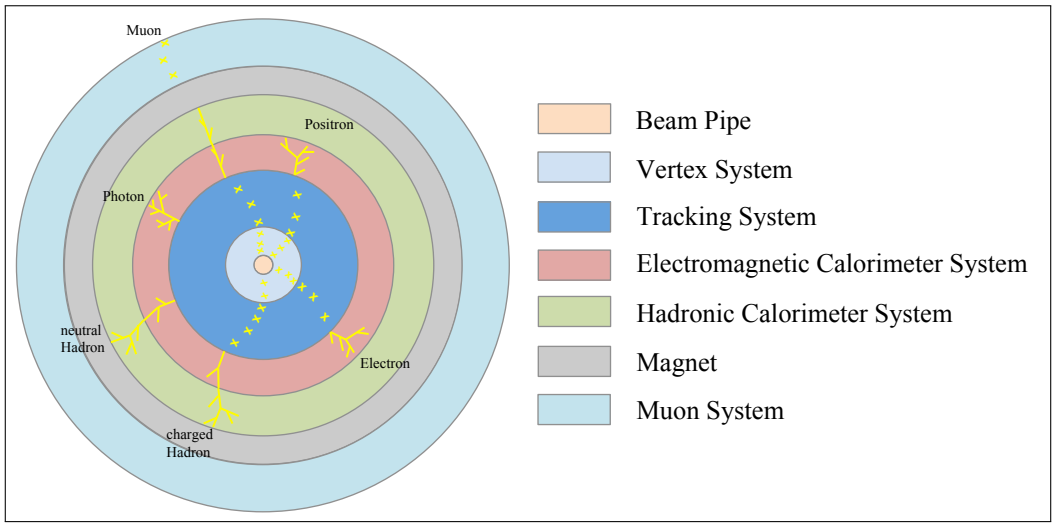

Figure 2.11: Generic particle detector including a vertex detector.

reason for this is that they interact only weakly. Despite this fact, the indirect reconstruction of at least the transverse energy of this particle, if the energy is large enough, is possible with sufficient accuracy. The way this is done is, actually, quite simple. In each event, the initial transverse momentum is zero so all the measured energies and momenta in the transverse plane of the final state can be added up. Thus the opposite vector is computed, i.e.,

$$-\sum_i \vec{E}_t^{\,i} \equiv \vec{\not{E}}_t, \tag{2.6}$$

where $\vec{\not{E}}_t$ stands for MET.

2.3 Compact Muon Solenoid

The CMS and ATLAS detector are called general purpose detectors. As described extensively in the technical proposal [42] and [43] the two detectors are designed differently.

The design was optimized for the detection of the Higgs boson in the "golden" channel, namely, the decay in two Z bosons, producing four isolated leptons with very high momentum, eventually muons or electrons and positrons. Specifically, this means the measurement of the lepton momentum up to 1 TeV, to a precision of at least 10%. This is due to the relation [4]

$$\frac{\Delta p}{p} \sim \frac{1}{BL^2}, \tag{2.7}$$

where B is the magnetic field strength and L is the distance over which the bending of the muon takes place. These requirements have in fact more than one solution:

- very large B, in a compact design in length (CMS) or

[4] In Appendix C a derivation of the formula (2.7) is given.

- large L with smaller magnetic field.

Some of the other design specifications can be derived from this requirement. For example the ATLAS calorimeters can be larger since they do not have to be contained within the solenoid, whereas the CMS electromagnetic calorimeter is chosen so that it can actually fit into the solenoid.

In this section a short overview of the structure of the CMS detectors is given firstly, followed secondly by a section on the magnet. The different parts of the CMS detector are then briefly explained, starting with the innermost layer, then the inner tracking system, and finally ending on the outermost layer, the muon system. Other very important issues for high luminosity experiments are the data acquisition and trigger system; these are elaborated on at the end of the section.

2.3.1 CMS Detector Overview

The overall layout of the CMS detector is shown in Fig. 2.12. The cylindrical structure is divided mainly into two parts: one barrel part and two so-called endcaps, closing the cylinder at both ends.

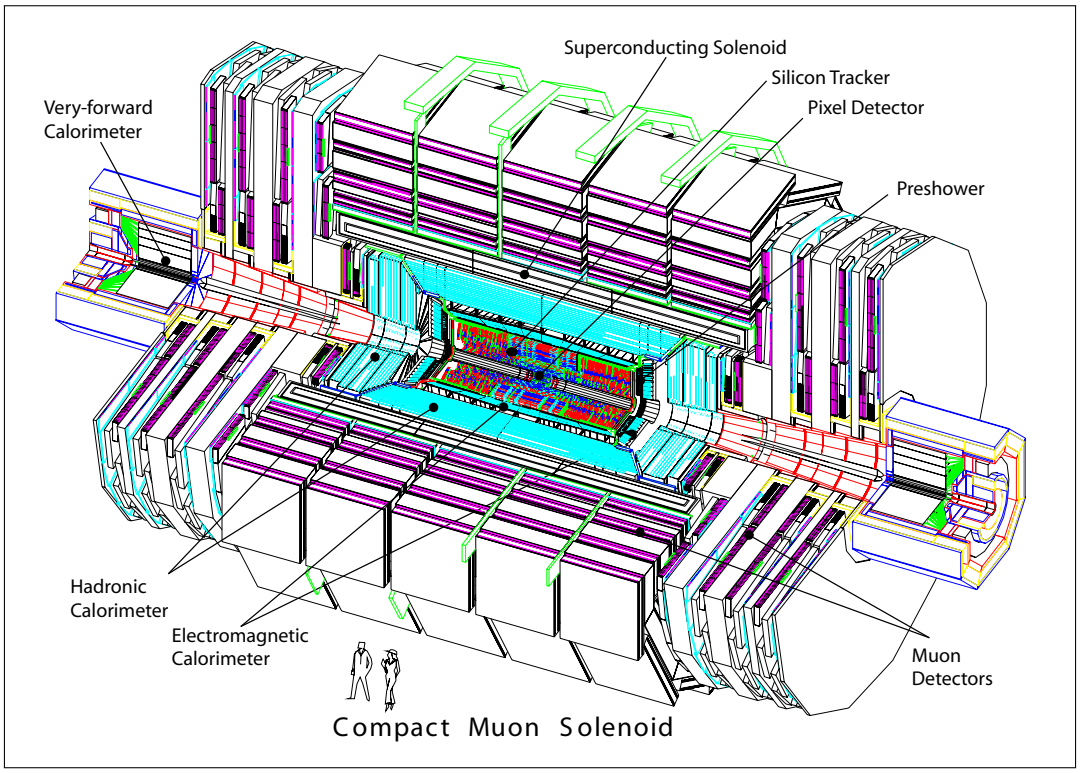

Figure 2.12: A perspective view of the CMS detector [44].

In Fig. 2.13, a cross-section and longitudinal schematic of the CMS is presented. The coordinate system adopted by CMS has the origin centered at the nominal collision point inside the experiment,

- the y-axis points vertically upward, and
- the x-axis points radially inward toward the center of the LHC.
- The z-axis points along the beam direction toward the Jura mountains.
- The azimuthal angle ϕ is measured from the x-axis in the x-y plane, and
- the radial coordinate in this plane is denoted by r.
- The polar angle θ is measured from the z-axis.

In addition to that, it is useful to define a boost invariant quantity [5], the pseudorapidity, which is widely used in high energy physics. This is defined as

$$\eta = -\ln \tan\left(\frac{\theta}{2}\right). \tag{2.8}$$

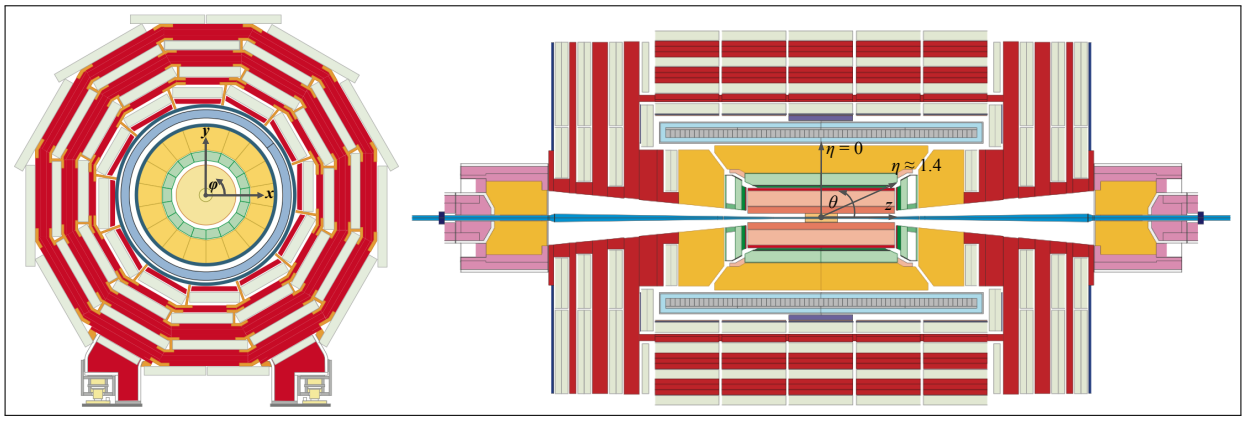

Figure 2.13: Cross-sectional view of CMS (left) and longitudinal view of CMS (right) [44].

Thus the momentum and energy, transverse to the beam direction as denoted by p_t and E_t, respectively, are computed from the x and y components

$$p_t = \sqrt{p_x^2 + p_y^2}, \quad \text{and} \quad E_t = \sqrt{E_x^2 + E_y^2}. \tag{2.9}$$

The above-mentioned variable $\vec{\not{E}}_t$ is the defined imbalance of the energy in the transverse plane.

As the name already suggests, the heart of the CMS is the superconducting solenoid. It is 13 m long and has an inner diameter of 6 m. The nominal magnetic field is 3.8 T, providing a large bending power before the muon bending angle is measured by the muon system. The field outside of the solenoid is large enough to saturate the iron return yoke at 2 T.

The tracker and the calorimeter are inside the magnet coil. The tracker is also built in a

[5] To be precise, only $d\eta$, or $\Delta\eta$ is invariant under Lorentz boosts.

cylindrical shape of 5.8 m length and 2.6 m diameter. CMS uses 10 layers of silicon microstrip detectors, which provide the required granularity and precision to be able to deal with high track multiplicities. 3 layers of silicon pixel detectors are placed close to the interaction region to improve the measurement of the impact parameter of charged particle tracks, as well as the position of secondary vertices.

The ECAL uses lead tungstate ($PbWO_4$) crystals that cover a range up to $|\eta| < 2.5$ in pseudorapidity. The produced scintillation light in the crystals is detected by silicon avalanche photodiodes (APDs) in the barrel region and vacuum phototriodes (VPTs) in the endcap region. To be able to separate single photons from the high rate of $\pi^0 \to \gamma\gamma$, a preshower system is installed in front of the endcaps.

The brass/scintillator sampling hadron calorimeter surrounds the ECAL. The overall CMS detector is about 30 m long and has a diameter of about 15 m. It has a total weight of 14 kt.

2.3.2 Superconducting Magnet

The superconducting magnet was designed to reach a 4 T field. It is 6 m in diameter and 12.5 m in length, with a stored energy of 2.6 GJ at full current. The flux is returned through a 10 kt yoke comprising of 5 wheels and 2 endcaps, composed of 3 disks each. In Fig. 2.14 the superconducting magnet with one wheel is illustrated.

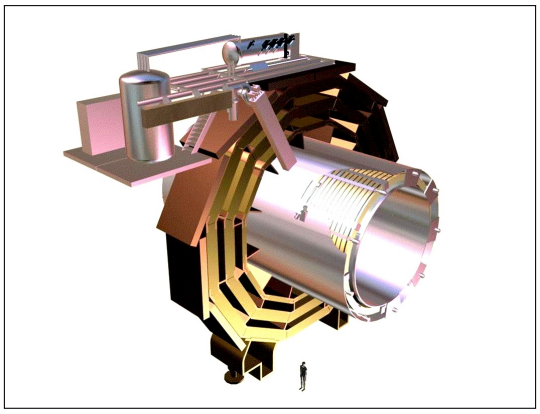

Figure 2.14: View of the CMS superconducting magnet with return yoke [45].

The superconductor is made of reinforced Niobium-Titanium (NbTi) which is used industrially. Its critical temperature is 10 K and can remain superconductive up to 15 T.

2.3.3 Inner Tracking System

The inner tracking system of CMS is designed to provide a precise and efficient measurement of the trajectories of charged particles emerging from the LHC collisions, as well as a precise reconstruction of secondary vertices. A schematic drawing of the CMS tracker is shown in Fig. 2.15. It is composed of a pixel detector and a silicon strip tracker. With an active silicon

area of about 200 m^2, the CMS tracker is the largest ever built.

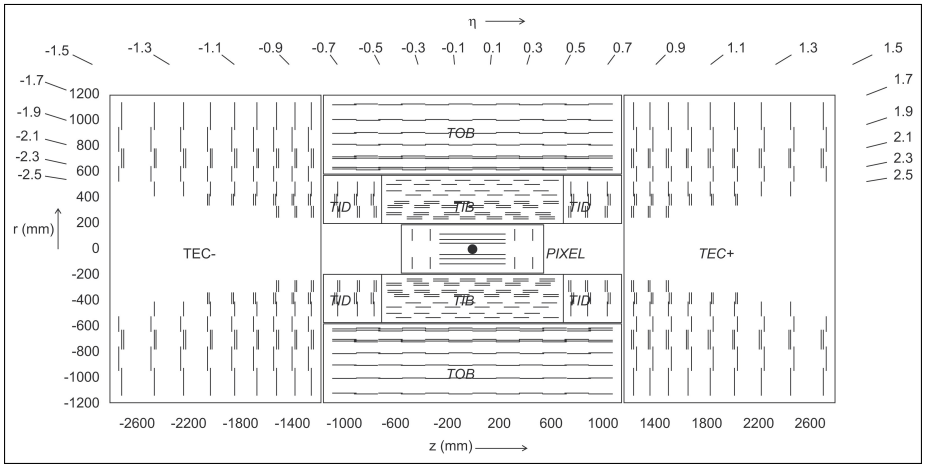

Figure 2.15: Schematic cross-section through the CMS tracker [46].

On the one hand, the tracker is required to have high granularity and fast response. On the other hand, these features imply a high power density of the on-detector electronics which, in turn, require efficient cooling. This is in direct conflict with the aim of minimizing the amount of material to limit

- multiple scattering,
- bremsstrahlung,
- photon conversion and
- nuclear interactions.

A compromise had to be found in this respect. As will be presented in chapter 3, bremsstrahlung and photon conversion are serious issues that have to be considered. In particular, the combination of a hard bremsstrahlung with an immediate photon conversion leads to some problems in the charge reconstruction of electrons. In Fig. 2.16 the material budget in units of radiation length as a function of pseudorapidity η is plotted.

Pixel Detector

The pixel system is the part of the tracking system that is closest to the interaction region. It contributes precise tracking points in r-ϕ and z, and therefore is responsible for a small impact parameter resolution, important for good secondary vertex reconstruction. With a pixel cell size of $100 \times 150\,\mu\mathrm{m}^2$, a 3D vertex reconstruction in space is possible.

The pixel detector is essential for the reconstruction of secondary vertices from $b-$quark decays, in forming seed tracks for the outer track reconstruction and high level triggering. It consists of

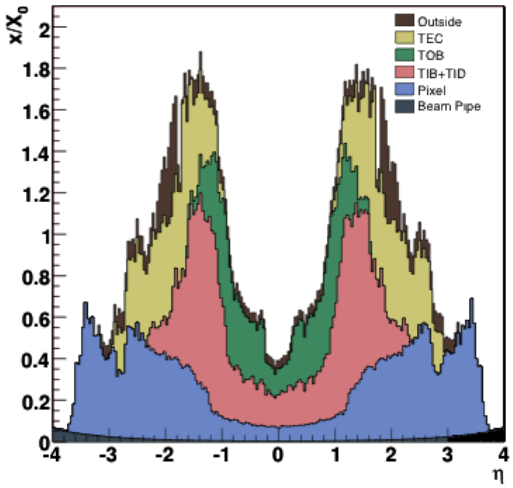

Figure 2.16: Material budget in units of radiation length as a function of η for the different sub-detectors in the inner tracker [46].

three barrel layers (BPix) located at mean radii of 4.4 cm, 7.3 cm and 10.2 cm respectively with two endcap disks (FPix) placed on each end at $z = \pm 34.5$ cm and $z = \pm 46.4$ cm (Fig. 2.17). BPix contains 48 million and FPix contains 18 million pixels, covering a total area of 0.78 m^2 and 0.28 m^2 respectively.

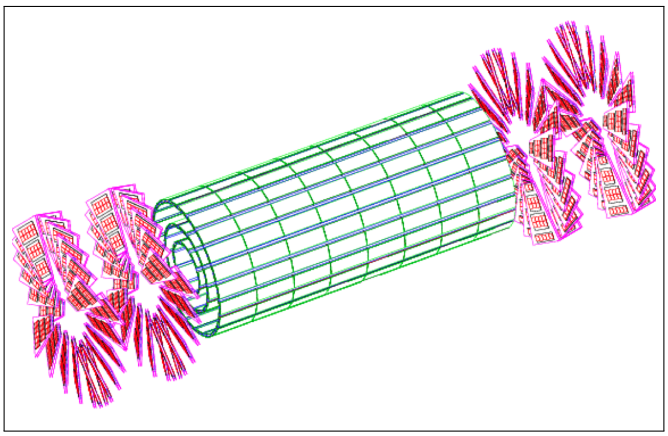

Figure 2.17: Layout of pixel detectors in the CMS tracker [46].

Being so close to the collision, means that the number of particles that pass through is huge. The rate of particles received from the beam line is around 10 million particles per square centimeter per second. Each layer is split into segments like tiny kitchen tiles. On each tile, there is an electronic silicon chip attached. The spatial resolution is in the range of 15-20 μm. In Fig. 2.18 the microscopic structure of the pixel detector is illustrated.

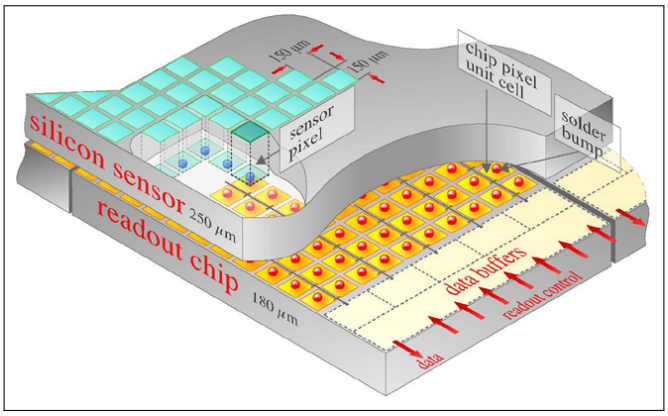

Figure 2.18: Illustration of the microscopic structure of the pixel detector. [47].

Silicon Strip Tracker

The silicon strip tracker is composed of 10 barrel detection layers, the tracker inner barrel (TIB) and the tracker outer barrel (TOB). The system is completed by endcaps which consist of 3 tracker inner disks (TID) plus 9 tracker endcaps (TEC±) on each end of the barrel. In TIB/TID and on the inner 4 rings of the TECs (Fig. 2.15), thin sensors of about 320 μm wafer thickness are used. The TOB and the outer 3 rings of the TECs are equipped with thicker sensors of about 500 μm. The spatial resolution is in the range of 20-60 μm.

The sensor elements in the strip tracker are single sided p-on-n type silicon microstrip sensors. For more information on the inner tracking system refer to [45].

2.3.4 Electromagnetic Calorimeter

The electromagnetic calorimeter of CMS is made of lead tungstate crystals, divided in a central barrel part and into two endcaps. A preshower detector is placed in front of the endcap crystals. The shower signal is amplified by APDs in the barrel and VPTs in the endcaps. One of the driving criteria in the design was the capability to detect the decay in two photons of the postulated Higgs boson.

This required a fast detector with fine granularity. It was achieved by the use of high density crystals. Of course, this capability is enhanced by the good energy resolution provided by a homogeneous crystal calorimeter. The resolution, for incident electrons as measured in a beam test, is shown in Fig. 2.19.

The stochastic (S), noise (N), and constant (C) terms are determined by fitting the measured points to the function

$$\left(\frac{\sigma(E)}{E}\right)^2 = \left(\frac{S}{\sqrt{E}}\right)^2 + \left(\frac{N}{E}\right)^2 + C^2. \tag{2.10}$$

One finds $S = 2.8\%\,(\mathrm{GeV})^{1/2}$, $N = 0.12\,\mathrm{GeV}$ and $C = 0.3\%$.

The layout of the whole ECAL, including the preshower, is shown in Fig. 2.20.

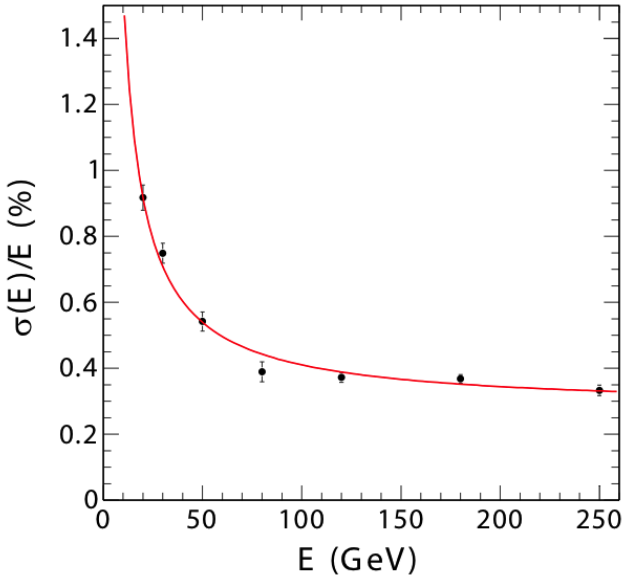

Figure 2.19: ECAL energy resolution, $\sigma(E)/E$, as a function of the electron energy is measured from a test beam [45].

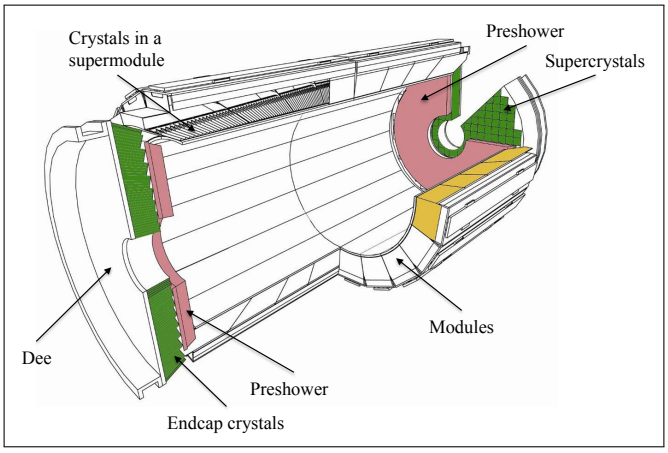

Figure 2.20: Layout of the CMS ECAL showing the arrangement of crystal modules, supermodules and endcaps, with the preshower in front [48].

Lead Tungstate Crystals

The characteristics of $PbWO_4$ crystals, as listed in Tab. 2.2, make thus the perfect choice to operate at LHC.

Parameters	ρ	X_0	R_M	τ_{decay}	λ_{max}
Units	g/cm^3	cm	cm	ns	nm
BGO	7.13	1.12	2.23	300	480
$PbWO_4$	8.3	0.89	2.00	25	425

Table 2.2: Characteristic values of the lead tungstate crystal compared with the L3 calorimeter at LEP, BGO.

The high density (ρ), short radiation length (X_0) and the small Molière radius (R_M) result in a fine granularity and a compact calorimeter. Another important characteristic is the scintillation decay time (τ_{decay}), which is of the same order of magnitude as the LHC bunch crossing time. The crystals emit blue-green scintillation light with a broad maximum (λ_{max}) at around 425 nm. Pictures of barrel and endcap crystals with the photodetectors attached are shown in Fig. 2.21.

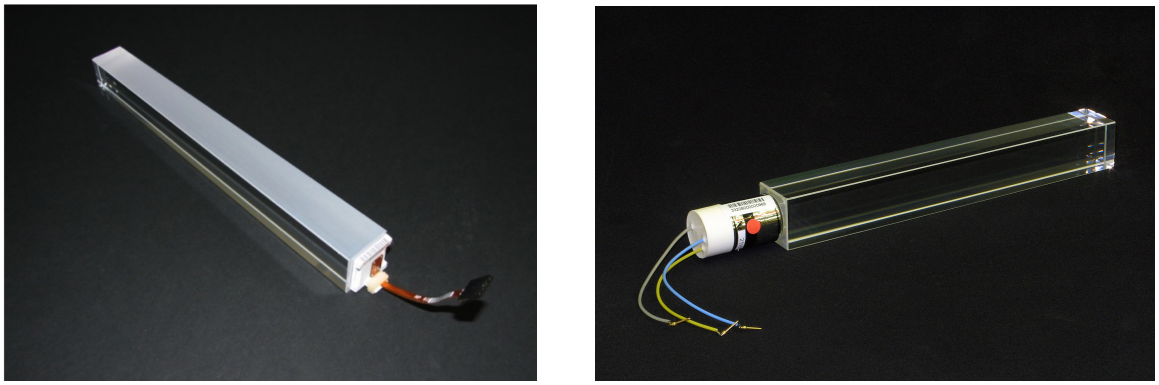

Figure 2.21: Lead tungstate crystals with attached photodetectors. (left) A barrel crystal with APD and (right) an endcap crystal with a VPT [45].

One additional requirement is that the crystals have to withstand high irradiation. Although the crystals performed well in irradiation tests, the radiation produces so-called color centers due to oxygen vacancies and impurities in the lattice. The consequence is a wavelength dependent loss of light transmission, a damage which can be corrected for by monitoring the optical transparency with injected laser light.

ECAL Layout

The ECAL barrel (EB) covers a range of $|\eta| < 1.4442$ and the endcaps (EE) cover $1.566 < |\eta| < 2.5$. The barrel consists of 61 200 crystals, in ϕ, there are 360 crystals and in η, 2×85 crystals.

The endcap is divided into 2 halves, or Dees. Each Dee holds 3 662 crystals totaling 14 648 crystals. In front of the endcaps the preshower detector (ES) is placed in order to be able to separate single photons from the high rate of π^0, within a fiducial region of $1.653 < |\eta| < 2.6$. In Fig. 2.22 the transverse section through the ECAL is shown.

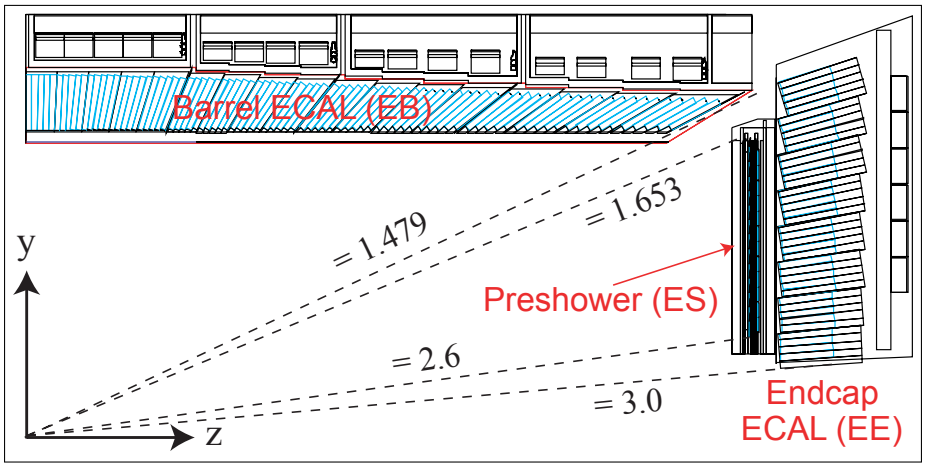

Figure 2.22: Transverse section through the ECAL, showing geometrical configuration [48].

The barrel crystal cross-section corresponds to approximately 0.0174×0.0174 in η-ϕ or $22 \times 22\,\mathrm{mm}^2$ at the front face, and $26 \times 26\,\mathrm{mm}^2$ at the rear. The length of the crystal is 230 mm and corresponds to $25.8\,X_0$. To avoid cracks aligned with particle trajectories, they are mounted such that they do not point to the vertex directly (tilt 3°). 10 crystals are contained in an alveolar structure (submodule). Between 40 and 50 submodules are assembled into modules of different types, according to the position in η. In total there are 34 different crystal shapes. 4 modules are assembled in a supermodule, as shown in Fig. 2.23.

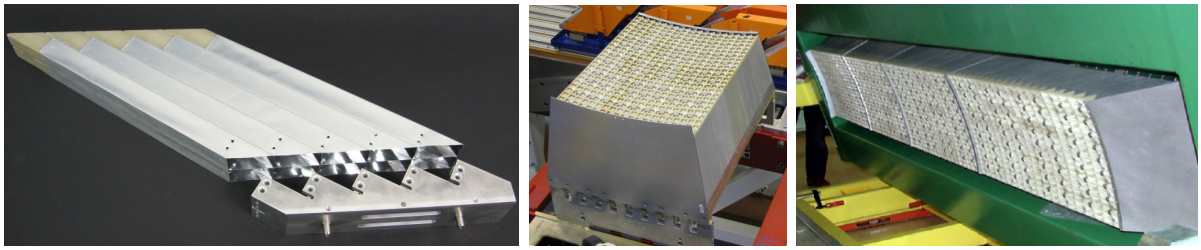

Figure 2.23: ECAL submodule (left), (center) module and (right) supermodule [49].

For the endcap crystals, the cross-section is $28.62 \times 28.62\,\mathrm{mm}^2$ at the front face and $30 \times 30\,\mathrm{mm}^2$ at the rear face. The length of 220 mm corresponds to $24.7\,X_0$. The endcap crystals tilt away from the interaction point, from 2° to 8°. The shapes of the crystals are all identical and they are grouped in units of 5×5, so-called supercrystals. Each Dee contains 138 standard supercrystals and 18 special partial supercrystals on the inner and outer circumference, illustrated in Fig. 2.24.

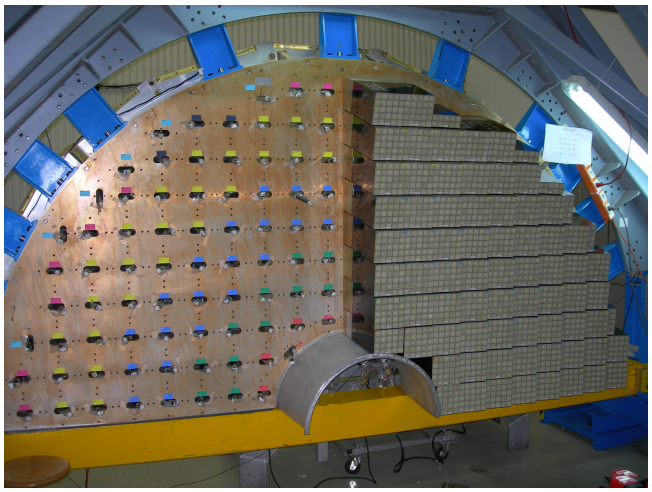

Figure 2.24: Endcap Dee, half equipped with supercrystals [50].

Photodetectors

The configuration of the magnetic field and the expected level of radiation led to two different photodetectors being used, namely:

- avalanche photodiodes in the barrel and
- vacuum phototriodes in the endcaps.

The lower quantum efficiency and internal gain of the VPTs, compared to the APDs, are offset by their larger surface coverage on the back face of the crystals.

The photodetectors in the barrel were specially developed for the CMS ECAL. Each APD has an active area of $5 \times 5\,\mathrm{mm}^2$ and they are mounted pairwise on each crystal. They are operated at gain 50 and read out in parallel. The sensitivity to the nuclear counter effect [6] is caused by the effective thickness of $6\,\mu$m, which translates into a signal from a minimum ionizing particle traversing an APD equivalent to about 100 MeV deposited in the crystal. In Fig 2.25 such a pair of APDs is shown.

VPTs are photomultipliers having a single gain stage. The particular devices were developed specially for CMS. Each VPT is 25 mm in diameter, with an active area of approximately $280\,\mathrm{mm}^2$. One VPT is glued to the back of each crystal and an example of one is shown in Fig. 2.26.

First real Collisions

In November 2009 the first real collisions occurred at 900 GeV CM energy. During the very first run one could already reconstruct the invariant mass of the π^0-meson, by measuring the two photons of the $\pi^0 \to \gamma\gamma$ decay. In Fig. 2.27 the invariant mass of the π^0-meson is plotted

[6] Particles traversing an APD induce an additional energy deposit, so-called nuclear counter effect.

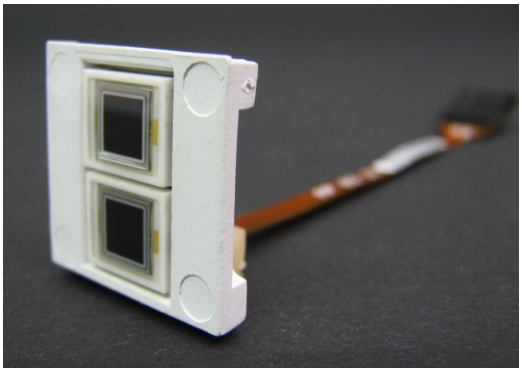

Figure 2.25: Avalanche Photodiodes [51]

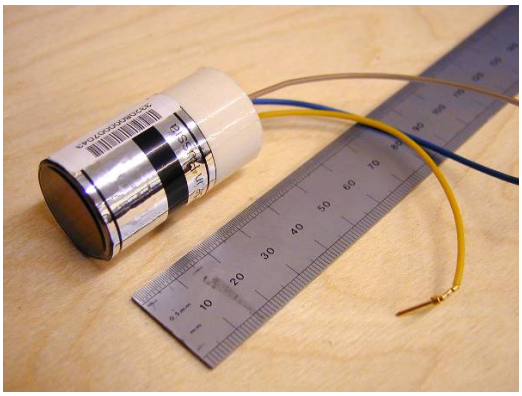

Figure 2.26: Vacuum Phototriodes [52].

and a gaussian fit is performed. The measured invariant mass with the *pre-calibrated* ECAL detector, i.e. the uncorrected cluster energy, is $m_{\pi^0} = 0.121 \pm 0.024\,\text{GeV}$. To select the photons, the following cuts were used:

- Trigger: Minimum bias,
- Photon energy: $E(\gamma) > 0.4\,\text{GeV}$,
- Di-photon energy: $E(\gamma_1) + E(\gamma_2) > 0.9\,\text{GeV}$ and
- Di-photon angle: $\cos(\theta_{12}) > 0.7$.

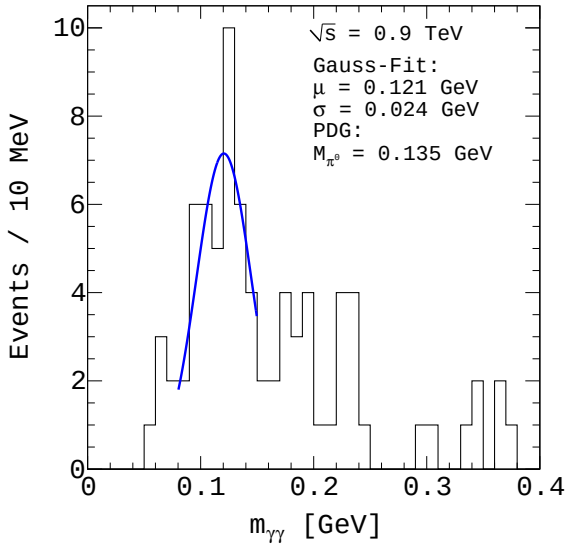

Figure 2.27: Invariant mass of the π^0-meson, measured with the ECAL detector.

Previously we discussed the problem of the large quantity of material in front of the ECAL resulting in a high rate of photon conversions. However, in the CMS collaboration the problem has been studied and it has been shown that it is possible to reconstruct the invariant mass of the π^0-meson in the decay $\pi^0 \to \gamma\gamma$ where one of the photon legs converted. For a detailed description refer to [53]. In Fig. 2.28 the invariant mass of the π^0-meson for such a decay is shown.

2.3.5 Hadron Calorimeter

The hadron calorimeters are particularly important for the measurement of hadron jets and neutrinos or exotic particles resulting in apparent missing transverse energy. The knowledge of the MET and the jet energy is crucial for almost all measured events within CMS. Also in the work presented here, the measurement of the jet spectrum plays an important role, and it would be impossible to do this without a good hadron calorimeter.

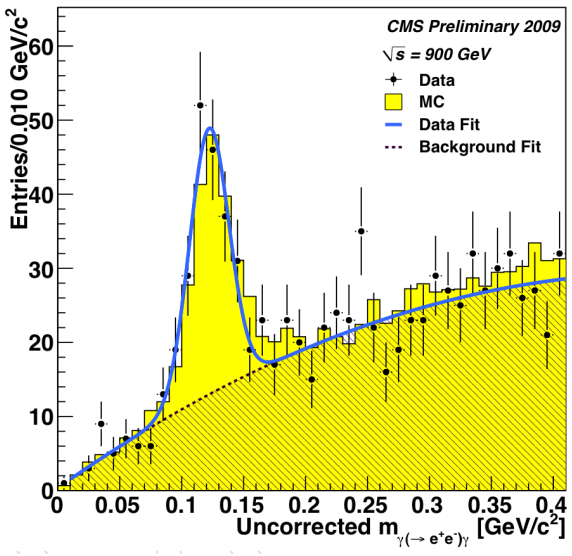

Figure 2.28: Invariant mass of π^0 candidates with one of the photon legs converted: data (black points) are superimposed on the MC expectation (filled yellow histogram). Monte Carlo is normalized to the same number of selected conversion candidates. A fit to the data points, obtained with a gaussian distribution summed with a second order polynomial to describe the combinatorial background component, is also shown [53].

Pions with energies of 150 GeV and 300 GeV were used to measure the response of the combined ECAL and HCAL system. The pion energy resolution obtained, is

$$\frac{\sigma(E)}{E} = \frac{138\%}{\sqrt{E}} + 13\%, \tag{2.11}$$

where E, is in GeV.

The HCAL detector is divided into 4 parts, 2 barrel, HB (HCAL Barrel) and the HO (HCAL Outer), and 2 endcaps, HE (HCAL Endcap) and the HF (HCAL Forward). Fig. 2.29 shows the longitudinal view of the detector.

The HCAL barrel is radially restricted between the outer extent of the ECAL and the inner extent of the magnet coil. This of course constrains the total amount of material which can be mounted, to absorb the hadronic shower. The HB and HE are sampling calorimeter. This means that absorber and scintillation material are put together alternatively. The absorber is made of flat brass plates and the scintillator of fluorescent material that produces a rapid light pulse when the particle passes through. Special optic fibers collect this light and feed it into read-out boxes, where photodetectors amplify the signal.

To ensure adequate sampling depth, the hadron calorimeter is extended outside the solenoid with a so-called tail catcher, the HO. The HO utilizes the solenoid coil as an additional absorber. The layers of scintillator tiles are located in front of the first layer of the barrel muon detector. Scintillation light from the tiles is collected through use of optical fibers.

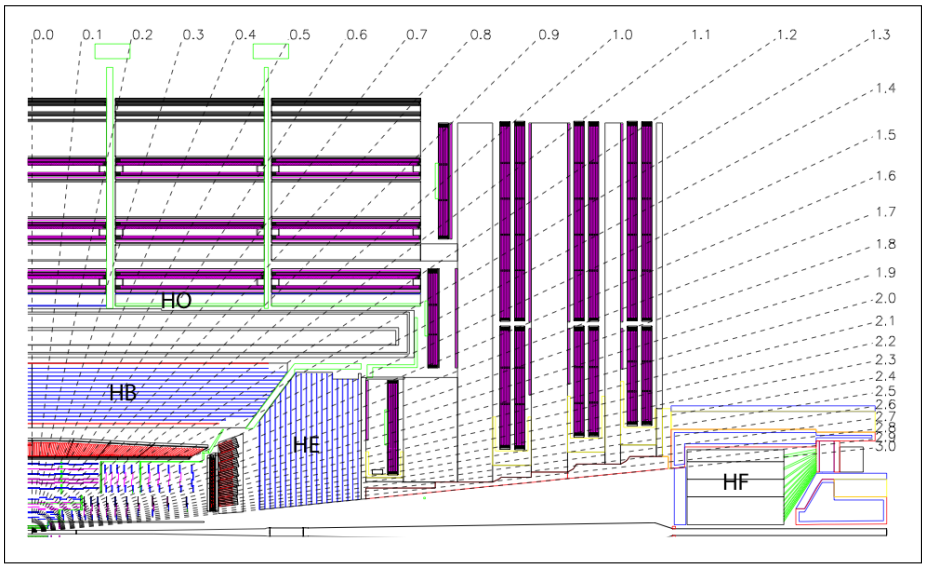

Figure 2.29: Longitudinal view of the CMS detector, showing the location of the HCAL [45].

The HF is a Cherenkov detector, arguably the most radiation resistive detector within CMS, and it experiences unprecedented particle fluxes. This was the principal reason why quartz fibers were chosen as the active medium.

2.3.6 Muon System

With the muon system an excellent mass resolution can be achieved, because the muons are less affected than electrons by radiative losses in the tracker material. For example, the predicted decay of the SM Higgs boson into ZZ, which, in turn, decays into 4 leptons, emphasizes the discovery potential of muon final states and the necessity for wide angular coverage for muon detection.

Due to multiple-scattering in the detector material before the first muon station, the offline muon momentum resolution of the standalone muon system is about 9% for p_t up to 200 GeV. At 1 TeV the standalone momentum resolution varies between 15% and 40%, depending on η. A global momentum fit using also the inner tracker improves the resolution by an order of magnitude at low momenta. At high momenta, both detector parts together yield a resolution of about 5%, as shown in Fig. 2.30.

The CMS muon system is designed to have the capability of reconstructing the momentum and charge of muons over the entire kinematic range of the LHC. CMS uses 3 types of gaseous particle detectors for muon identification. The muon system consists of several layers of aluminum drift tubes (DT) in the barrel region and cathode strip chambers (CSC) in the endcap region, complemented by resistive plate chambers (RPC). In Fig. 2.31 the components are shown.

The DT system measures muon positions in the barrel part of the detector. Each tube contains a stretched wire within a gas volume. When a muon or any charged particle passes through the volume, it knocks electrons off the atoms of the gas. These follow the electric field ending

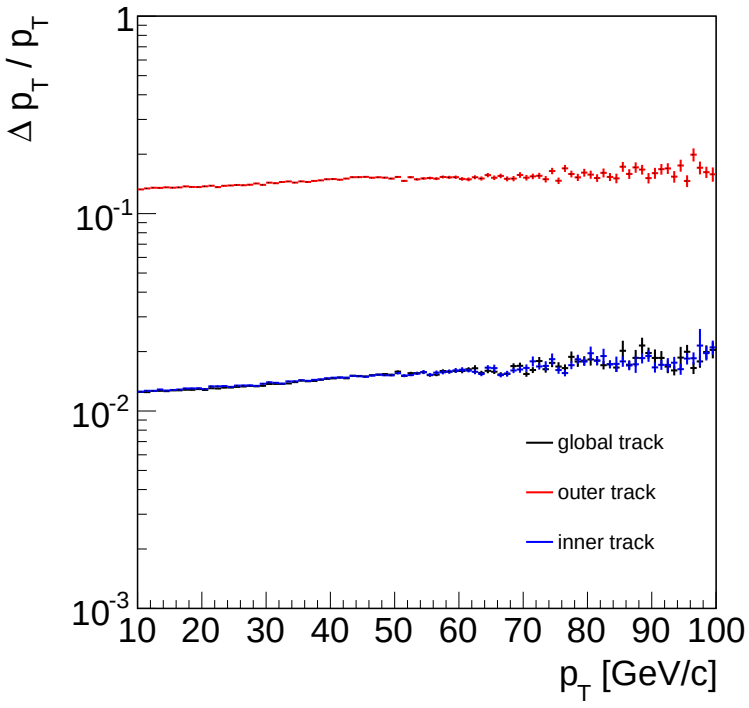

Figure 2.30: Muon resolution for inner and outer track muons and global muons.

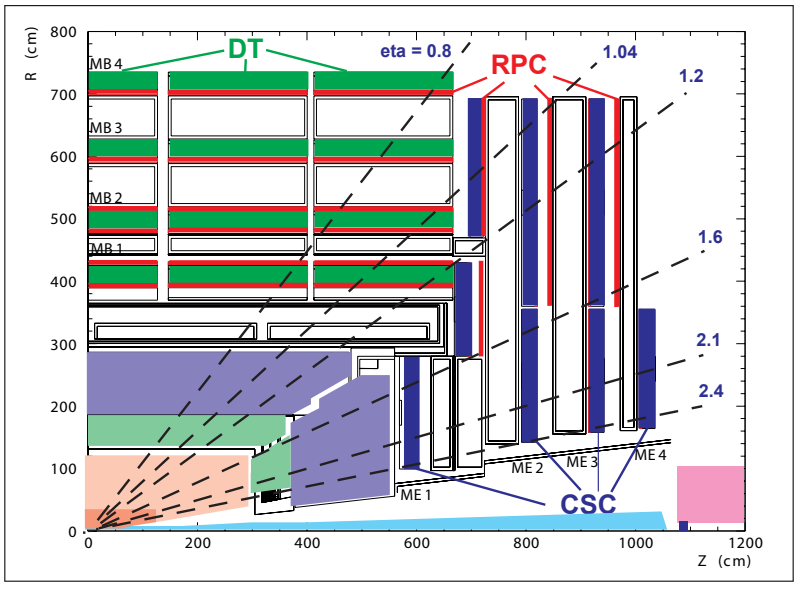

Figure 2.31: Layout of one quarter of the CMS muon system [48].

up at the positively-charged wire. By registering where the electrons hit the wire, as well as by calculating the muon's original distance away from the wire, the coordinates of the muon position can be measured. Each DT chamber, on average $(2 \times 2.5)\,\mathrm{m}^2$ in size, consists of 12 aluminum layers, arranged in 3 groups of 4, each with up to 60 tubes. The middle group measures the z position and the two outside groups measure the r-ϕ coordinate.

The CSCs are multiwire proportional chambers comprised of anode wire planes interleaved among cathode panels. Wires run azimuthally and define a tracks radial coordinate. Strips run lengthwise. When muons pass through, they knock electrons off the gas atoms, which flow to the anode wires creating an avalanche of electrons, also inducing a charge pulse in the strips, at right angles to the wire direction. Because the strips and the wires are perpendicular, we get two position coordinates for each passing particle. In addition to providing precise space and time information, the closely spaced wires make the CSCs fast detectors suitable for triggering. Each CSC module contains six layers enabling it to accurately identify muons and match their tracks with those in the tracker.

RPCs are fast gaseous detectors that provide a muon trigger system parallel with those of the DTs and CSCs. RPCs consist of two parallel plates, a positively charged and a negatively charged one, both made up of a very high resistivity plastic material and separated by a gas volume.

2.3.7 Data Acquisition and Triggering

The trigger and data acquisition (DAQ) system is designed to collect and analyze the detector information. The collision rates of about 40 MHz crossing frequency, or 25 ns of beam crossing interval. This results in a high number of events to store, approximately 1 MBytes of zero-suppressed data in the read-out system. Since it is impossible to store everything, a drastic rate reduction has to be achieved. This task is performed by the trigger system, which is the starting point of the physics event selection process. In CMS the rate is reduced in two steps called level 1 (L1) trigger and high level trigger (HLT), respectively.

The L1 trigger is designed to reduce the incoming average data rate to a maximum of 100 kHz, by processing fast trigger information coming from the calorimeters and the muon chambers, and selecting events with interesting signatures. Therefore, the DAQ system must sustain a maximum input rate of 100 kHz, for a data flow of ~ 100 GBytes/s and must provide enough computing power for the HLT, to reduce the rate of stored events by a factor of 1 000. The rate of events to be recorded for offline processing and analysis is of the order of a few 100 Hz. In CMS all events that pass the L1 trigger are sent to a computer farm (Event Filter) that performs fast physics selections. In Fig. 2.32 the architecture of the DAQ system is shown.

The L1 trigger consists of programmable electronics, whereas the HLT is a software system whose algorithms will evolve with time and experience. The L1 trigger uses roughly segmented data from the calorimeters and the muon system. The L1 trigger is divided into three components, local, regional and global. At the bottom of the L1 hierarchy, the local triggers are based on energy deposits in calorimeter trigger towers and track segments or hit patterns in muon chambers. Regional triggers combine their information. The global calorimeter and global

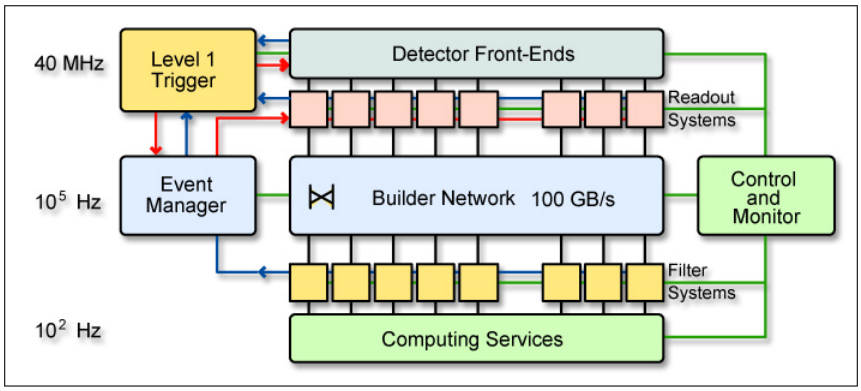

Figure 2.32: Architecture of the DAQ system [48].

muon triggers determine the highest rank and transfer them to the global trigger, at the top of the L1 hierarchy. The architecture of the L1 trigger is illustrated in Fig. 2.33.

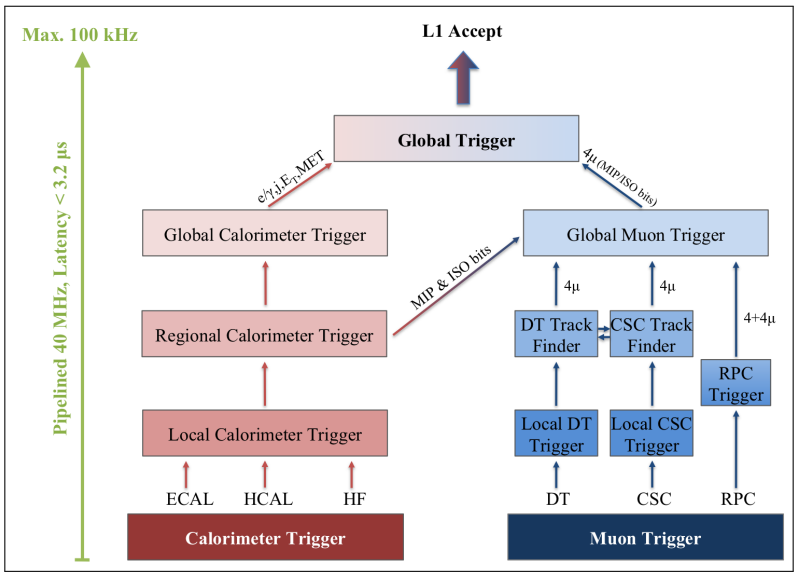

Figure 2.33: Architecture of the level 1 trigger.

Electron L1 Trigger

Three electromagnetic triggers are used at L1. A single isolated trigger, a double isolated trigger and a double trigger at a slightly higher threshold, with the trigger isolation requirement removed. The E_t thresholds used for these 3 triggers are 23, 12 and 19 GeV respectively.

The non-isolated electron [7] identification is based on:

- the energy deposit in the trigger cells,

[7] Hence forth we will denote electrons and/or positrons only as electrons.

- the lateral shower profile and
- the longitudinal shower profile, i.e. the ratio of E_t deposits in the HCAL and ECAL (H/E).

The isolated electron require two additional criteria based on:

- the electromagnetic isolation and
- the hadronic isolation.

In Fig. 2.34, the L1 trigger rate and the efficiency for 120 GeV mass Higgs events decaying into 4 electrons is shown. In this plot, and in the following tables, the signal efficiencies are computed for events where at least 2 of the generated electrons lie inside the fiducial acceptance of the ECAL ($|\eta| < 1.4442$ or $1.566 < |\eta| < 2.5$). In addition, a lower cut of 5 GeV is applied on the p_t of the generated electrons.

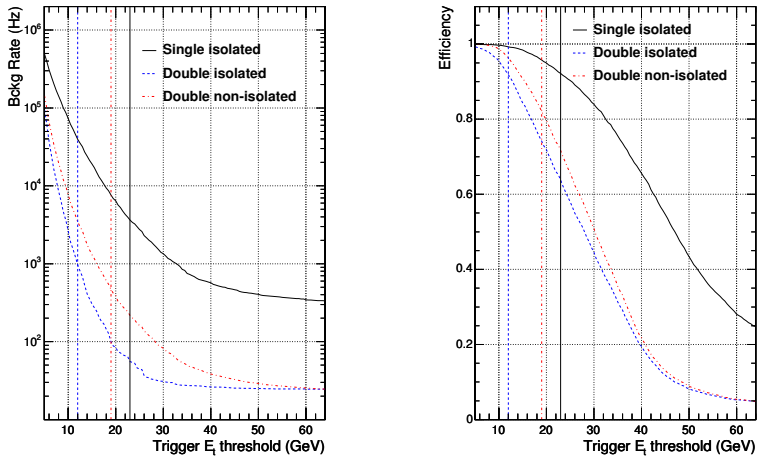

Figure 2.34: L1 trigger rate for jet events (left), efficiency for $H \to 4e$ (right) as function of the trigger thresholds [48].

The L1 trigger rates at luminosity $\mathcal{L} = 2 \cdot 10^{33}\,\mathrm{cm}^{-2}\mathrm{s}^{-1}$ are shown in Tab. 2.3.

Single Isolated	Double Isolated	Double non-isolated	Total
3 400 Hz	1 010 Hz	420 Hz	4 440 Hz

Table 2.3: L1 trigger rates at $\mathcal{L} = 2 \cdot 10^{33}\,\mathrm{cm}^{-2}\mathrm{s}^{-1}$ [48].

The L1 trigger efficiencies for electron $p_t > 5\,\text{GeV}$ are listed in Tab. 2.4.

Signal Process	Single Isolated	Double Isolated	Double non-isolated	Total
$H \to ZZ \to 4e$	90.8%	89.5%	79.5%	96.5%
$Z \to 2e$	93.5%	81.5%	85.1%	97.1%

Table 2.4: L1 trigger efficiency at $\mathcal{L} = 2 \cdot 10^{33}\,\text{cm}^{-2}\text{s}^{-1}$ [48].

Electron High Level Trigger

The HLT selection of electrons proceeds in 3 steps. The first, Level-2, step uses only calorimeter information, the second step, Level-2.5, uses the information from the pixel detectors and in the final step, Level-3, the full tracker information is used.

Level-2 selection

The first step of the HLT selection consists of the verification of the L1 trigger decision. E_t thresholds are applied to reconstructed supercluster matched in η and ϕ with the triggering towers. The E_t thresholds are 23, 12 and 19 GeV for the single isolated, double isolated and double non-isolated L1 triggers respectively.

Level-2.5 and Level-3 selection

The HLT selection for electrons is based on:

- matching of the supercluster position with the pixel hits,
- requiring HCAL and track electron isolation and
- for the single trigger E/p matching between the energy reconstructed in the ECAL and the corresponding track momentum measured in the tracker.

By using these additional HLT selections the trigger rate reduces from a few kHZ to a few Hz depending on the specific cut values.

2.3.8 Computing

Even after going through the trigger system, CMS still produces a huge amount of data that must be analyzed; more than 5 PBytes per year when running at peak performance. To meet this challenge, the LHC uses a novel computing system. This distributed computing and data storage infrastructure is called the worldwide LHC computing grid (WLCG). In "The Grid", tens of thousands of standard PCs collaborate worldwide and result in much more processing capacity than could be achieved by a single supercomputer.

The WLCG is divided into four so-called Tiers (T), T0, T1, T2 and T3.

- At the T0 center at CERN [8] the full collision event data (RAW data) are reconstructed (RECO data) and a primary backup of the RECO data is made.
- The T1 centers, in seven locations around the world [9], rereconstruct the RECO data, using information from the experiment to improve calculations using refined calibration constants.
- The T2 centers, numbering around 40, store the MC samples and the rereconstructed data for further specific analysis tasks.
- In a very last step, a small fraction of the data is sent to the Tier 3 centers, where a final analysis can be done.

In this way information branches out from each tier across the world so that, on a local level, one can study CMS data which is updated on a regular basis by the WLCG, from his/her own computer. In Fig. 2.35 the data flow between the tiers is shown.

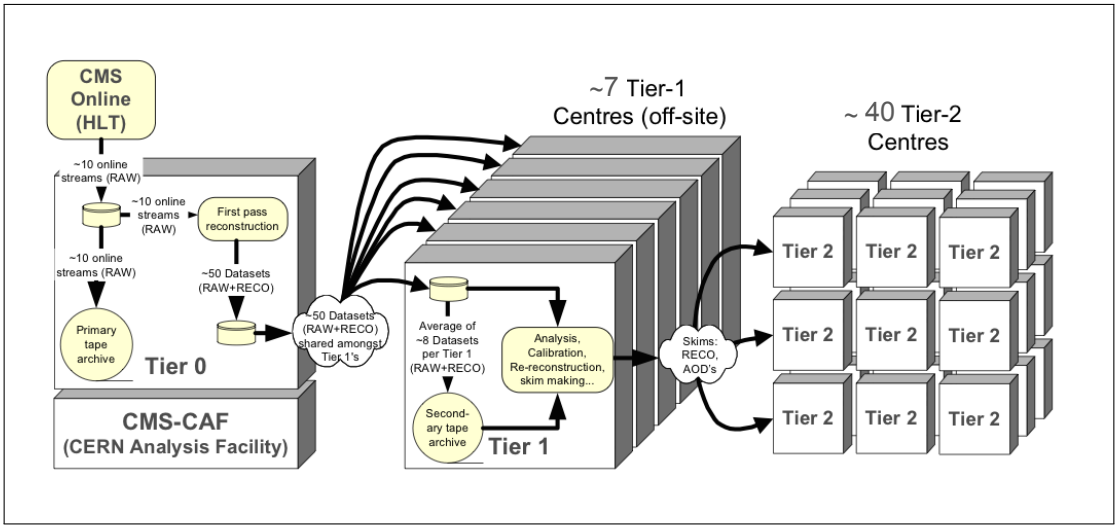

Figure 2.35: Data flow through CMS computing centers, excluding the T3 centers [45].

In this chapter the collider experiment was described, with a focus on the CMS detector. After a generic introduction to high energy particle detectors, the different parts of the CMS detector were described including an explanation of the WLCG. In the next chapter the selection of the $Z \to e^+e^-$ events will be elaborated on, starting with the electron selection, followed by a discussion of the reconstruction of the Z boson.

[8] The CERN analysis facility (CAF) combines flexible CPU resources with rapid access to the entire CMS dataset.

[9] In France, Germany, Italy, Spain, Taiwan, the UK and the US.

Chapter 3

Selection of $Z \to e^+e^-$ Events

The generation of random numbers is too important
to be left to chance.
- Robert R. Coveyou [54]

The selection of isolated high p_t leptons is an important issue in hadron colliders. This is due to the fact that events with such leptons are easy to separate from the huge QCD background. In this thesis, the focus is on isolated high p_t electrons, which are measured mainly with the ECAL detector.

In this chapter the reconstruction chain for Monte Carlo (MC) $pp \to Z \to e^+e^-$ events is described. We start by outlining the event generator, followed by a description of the track and cluster reconstruction. In the third section the electron selection will be discussed, followed by a description of the Z boson reconstruction. Then the single electron efficiency will be measured, using two different techniques: a MC based and a data driven method, the so-called "tag and probe" method. A first look at real data will conclude this chapter.

3.1 Generator Level

Events are generated with PYTHIA6.4 [55], which is a program that can be used to generate high energy collisions. Outgoing particles are produced in the interactions between two incoming particles. In our case the particles interacting are the constituents of the protons, e.g. in LO $q\bar{q} \to \gamma^*/Z \to e^+e^-$. The corresponding Feynman diagram is shown in Fig. 3.1.

3.1.1 Parameters of the Generator

In this brief subsection a few variables for the signal and the background samples are listed. The signal parameters, relevant for our purpose, are described in Tab. 3.1.

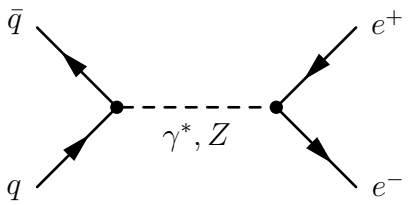

Figure 3.1: Leading order Feynman diagram for $q\bar{q} \to \gamma^*/Z \to e^+e^-$ process.

Parameter	Value	Meaning
pyinit	p, p	proton-proton
COMEnergy	10 000	CM energy is 10 TeV
MSTP(51)	10042	CTEQ6L1 PDF chosen
$Z \to e^+e^-$		
Xsec	1944	Cross-section in pb
FiltEff	1	Filter efficiency (CMS parameter)
MSEL	0	User defined processes
MSUB(1)	1	γ^*/Z production
MDME(182,1)	1	Decay into e^+e^-
CKIN(1)	20	Min. value for $m_{e^+e^-}$ in GeV

Table 3.1: Global and signal parameter set.

For the relevant background two QCD samples and one electroweak sample are used:

- QCD EM Enriched, i.e. high p_t QCD events with an electromagnetic filter applied.
- QCD $b/c \to e$, i.e. high p_t QCD events with a transverse energy filter applied.
- $W \to e\nu$, where a jet fakes an additional electron.

Another potential background comes from $t\bar{t}$, with the t-quark decaying into Wb, shown in Fig. 3.2.

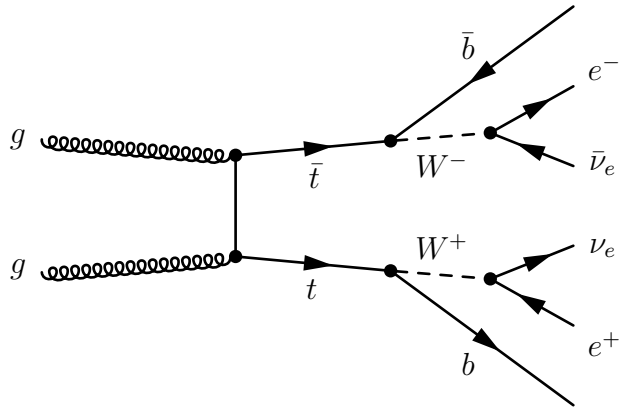

Figure 3.2: Feynman diagram for $gg \to t\bar{t}$ process, decay to Wb and the W's decaying in electron and positron.

The parameters used for the generation of the MC events are listed in in Tab. 3.2, whereas the global parameters: the particle type, CM energy and the used PDF set, were provided in Tab. 3.1. In Tab. 3.3 the number of generated events for the signal and background samples are summarized.

3.1.2 Distributions at the Generator Level

For this analysis we focus on a sample of roughly 2M $Z \to e^+e^-$ events, corresponding to an integrated luminosity of about $\mathcal{L}_{\text{int}} = 1.4\,\text{fb}^{-1}$. A subsample of 20k events has been used to obtain a data like sample, the so-called pseudo data sample corresponds to $\mathcal{L}_{\text{int}} = 10\,\text{pb}^{-1}$. These data sets are denoted as

- Monte Carlo (MC), for $\mathcal{L}_{\text{int}} = 1.4\,\text{fb}^{-1}$ and
- pseudo data (pData), for $\mathcal{L}_{\text{int}} = 10\,\text{pb}^{-1}$.

In all comparison plots the MC sample is normalized to $10\,\text{pb}^{-1}$. These sets were generated with a minimal dielectron mass of 20 GeV and without any restrictions in rapidity and transverse momentum. Fig. 3.3(a) shows the generated mass distribution of these events. Here the e^+e^- pairs were generated before a possible final-state radiation, leading to a sharp mass cut at 20 GeV. Selecting the pairs after the radiation, gives a slightly different Z mass distribution,

Parameter		Value		Meaning
QCD EM Enriched:				
Xsec	$0.4 \cdot 10^{-9}$	$0.1 \cdot 10^{-9}$	$1.9 \cdot 10^{-12}$	Cross-section in pb
FiltEff	0.008	0.047	0.15	Filter efficiency
MSEL	1	1	1	QCD high p_t processes
CKIN(3)	20	30	80	Min. $\hat{p}_t$ for hard interaction
CKIN(4)	30	80	170	Max. $\hat{p}_t$ for hard interaction
QCD $b/c \to e$:				
Xsec	$0.4 \cdot 10^{-9}$	$0.1 \cdot 10^{-9}$	$1.9 \cdot 10^{-12}$	Cross-section in pb
FiltEff	0.00048	0.0024	0.012	Filter efficiency
MSEL	1	1	1	QCD high p_t processes
CKIN(3)	20	30	80	Min. $\hat{p}_t$ for hard interaction
CKIN(4)	30	80	170	Max. $\hat{p}_t$ for hard interaction
$W \to e\nu$:				
Xsec		11 840		Cross-section in pb
FiltEff		0.738		Filter efficiency
MSEL		0		User defined processes
MSUB(1)		2		W production
$t\bar{t}$:				
Xsec		242.8		Cross-section in pb
FiltEff		1		Filter efficiency
MSUB(81)		1		$q\bar{q} \to t\bar{t}$
MSUB(82)		1		$gg \to t\bar{t}$
PMAS(6,1)		172.5		Top quark mass

Table 3.2: Background parameter set for 10 TeV; Cross-section (Xsec), filter efficiency and minimum and maximum $\hat{p}_t$ are listed. Here $\hat{p}_t$ indicates the transverse momentum evaluated in the rest frame of the scattering.

Process	Number of Generated Events	Integrated Luminosity [fb^{-1}]
$Z \to e^+e^-$	2 641 645	1.4
QCD EM Enriched:		
$20 < \hat{p}_t < 30$	22 546 912	$7.0 \cdot 10^{15}$
$30 < \hat{p}_t < 80$	11 329 230	$2.4 \cdot 10^{15}$
$80 < \hat{p}_t < 170$	5 018 579	$1.8 \cdot 10^{16}$
QCD $b/c \to e$:		
$20 < \hat{p}_t < 30$	179 621	$9.4 \cdot 10^{14}$
$30 < \hat{p}_t < 80$	237 667	$9.9 \cdot 10^{14}$
$80 < \hat{p}_t < 170$	197 982	$8.7 \cdot 10^{15}$
$W \to e\nu$	2 153 199	0.25
$t\bar{t}$	529 750	2.2

Table 3.3: Number of generated events with corresponding cross-section for signal and background.

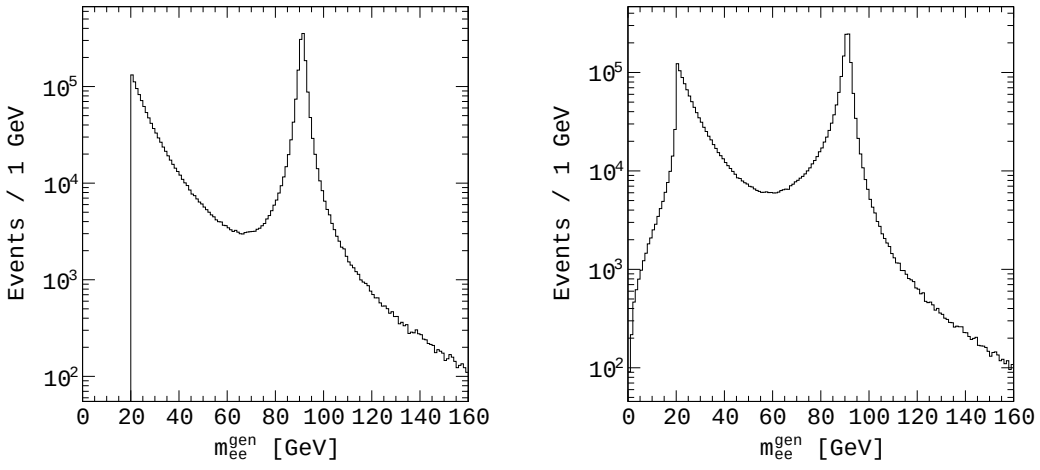

(a) (b)

Figure 3.3: Generated mass distribution of e^+e^- pairs without (a) and with (b) photon radiation.

since the photon radiation leads to a lower invariant mass reconstruction for events with final-state radiation, as shown in Fig. 3.3(b). For this study of resonant Z production, only events with a generated e^+e^- mass near the Z pole, i.e.

$$|m_{ee} - 91.2\,\text{GeV}| < 3 \cdot \Gamma_Z \approx 7.5\,\text{GeV}, \tag{3.1}$$

were considered. In what follows, the generated e^+e^- pairs were generated with final-state radiation, to be consistent with the future real data. In general the radiated photon is collinear to the electron, wherein the reconstructed energy is the sum of the electron energy and the radiated photon energy.

In Tab. 3.4 the remaining number of Z candidates, normalized to $\mathcal{L}_{int} = 10\,\text{pb}^{-1}$ are listed.

Cuts	Z Candidates	
no cut	19 440	100%
$\lvert m_{ee} - 91.2\,\text{GeV}\rvert < 3\Gamma_Z$	8 759	45%
$p_t^e > 20\,\text{GeV}$, $\lvert\eta\rvert < 1.44$	1 858	9.6%

Table 3.4: Number of events on generator level with initial-state radiation.

The generated rapidity distribution of the Z boson is shown in Fig. 3.4. In addition, the rapidity distribution of the potentially accepted Z's, where both generated decay electrons are within the acceptance of the barrel (bb), $|\eta| < 1.44$, are also plotted.

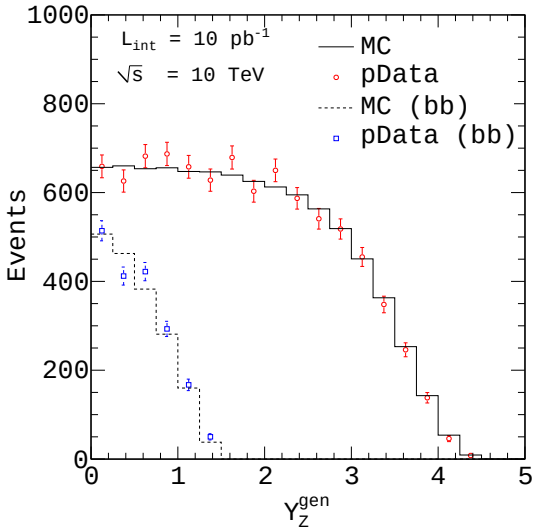

Figure 3.4: Generated rapidity distribution for all Z candidates and for those where both electrons were generated within the ECAL barrel (bb).

For the early data ($\mathcal{L}_{int} = 10\,\text{pb}^{-1}$) it was envisaged to measure the Z with electrons only

in the barrel part of the ECAL ($|\eta| < 1.44$ [1]) and for these electrons to have high transverse momentum, i.e. $p_t > 20\,\text{GeV}$. The reason for focusing only on the barrel for the early phase of the experiment is that electrons in the barrel might be better understood than the one in the endcaps.

3.2 Electron Reconstruction

The reconstruction of electrons and positrons uses information from the pixel detector, the silicon strip tracker and the ECAL. A description of these detectors was given in section 2.3. The measurement of the electron energy in the ECAL is effected by the amount of tracker material in front of the ECAL (Fig. 2.16), and by the presence of a strong magnetic field (cf. section 2.3.2). Electrons traversing the silicon layers of the tracker radiate bremsstrahlung photons depending on the electron energy. The energy reaches the ECAL with a significant spread in the azimuthal direction ϕ. The ECAL clustering, and in particular the building of "superclusters" (clusters of clusters), is designed to take into account the ϕ spread and collect the bremsstrahlung energy. To initiate the building of trajectories in the inner tracker, the supercluster is used. The electron track reconstruction relies on a dedicated gaussian sum filter (GSF) [56], using a specific energy loss model.

3.2.1 Electron Seeding

The reconstruction of electrons in CMS starts by the reconstruction of clusters in the ECAL, which are used to form superclusters to further collect the energy radiated by bremsstrahlung passing the tracker. The η-ϕ geometry of the barrel crystals allows a hybrid algorithm to exploit our knowledge of the lateral shower shape in the η direction (by taking a fixed bar of 3 or 5 crystals in η), while searching dynamically for separated energy in the ϕ direction, where the minimum seed transverse energy is 1 GeV. A more detailed description of the clustering mechanism is given in [57].

3.2.2 ECAL Energy and Position Measurements

The energy collected by the cluster procedure does not agree with the truth energy of the electron. To compensate for this missing energy, a correction factor has to be applied. This correction factor is a function of the measured number of crystals, N_{cry}, which make up the cluster volume. The dependence on N_{cry} can be described by a universal containment correction function $f(N_{\text{cry}})$. The distributions for uncorrected and corrected energies are plotted in Fig. 3.5, where E_{meas} represents the measured quantity and E_{true} is the generated truth energy. Only electrons within the barrel with a $p_t > 20\,\text{GeV}$ are plotted.

An additional problem in measuring the right energy are the tiny gaps between the supermodules. In the gaps a small, but not negligible, amount of energy is lost. This has to be corrected for, by applying an additional correction factor for superclusters having crystals in more than

[1] This fiducial volume is chosen to be slightly smaller than the CMS standard fiducial volume $|\eta| < 1.479$, in order to have some safety margin at the borders of the calorimeter.

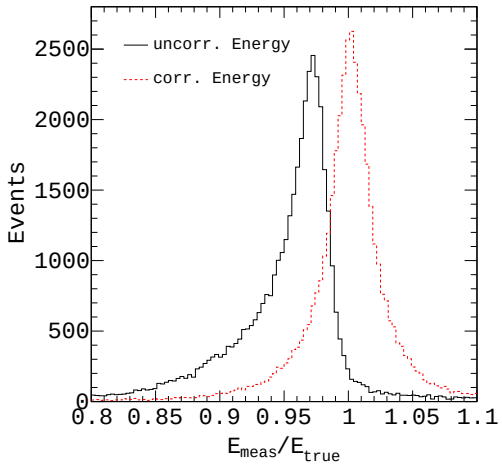

Figure 3.5: Distributions for uncorrected supercluster energy (black line) and corrected (red dashed line).

one supermodule. This issue could not be perfectly solved, as shown in Fig. 3.6, where an efficiency plot as a function of the azimuth angle ϕ is plotted. To amplify this effect all supermodules are folded such that the odd (even) numbered supermodules always cover local ϕ angles from 0 to 20 (20 to 40) degrees. The effect of the gaps is clearly visible at 0°, 20° and 40° and a drop of about 10% is observed.

A position measurement of the shower can be obtained by calculating the energy weighted mean position of the crystals in the cluster, i.e.

$$x = \frac{\sum x_i \cdot W_i}{\sum W_i}, \tag{3.2}$$

where x_i is the position of crystal i, and W_i is the log of the fraction of the cluster energy contained in the crystal, calculated with

$$W_i = W_0 + \log\left(\frac{E_i}{\sum_j E_j}\right), \tag{3.3}$$

where the weight is constrained to be positive, or is otherwise set to zero. W_0, then controls the smallest fractional energy that a crystal can have and still contribute to the position measurement. Its default value is chosen such as to get the best signal over noise ratio [2].

3.2.3 Electron Tracking and Momentum Determination

In order to best handle the effect of bremsstrahlung, superclusters consistent with electromagnetic showers are used to initiate a dedicated electron track building and fitting procedure.

[2]The default value found in MC test is $W_0 = 4.2$, which corresponds to a threshold energy of 1.5% of the maximum energy contained in a crystal of this event. Some other studies with a test beam on the ECAL gave different values (e.g. $W_0 = 3.8$). At the end, with the real data, the value will be optimized.

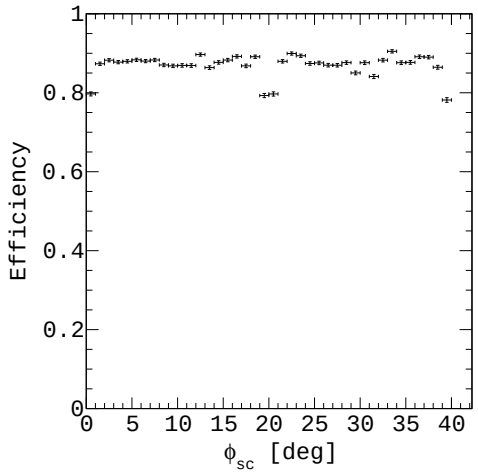

Figure 3.6: Reconstruction electron efficiency as a function of the supercluster ϕ, in which all even and odd numbered supermodules are folded such that the odd (even) numbered supermodules always cover local ϕ angles from 0 to 20 degrees and from 20 to 40 degrees, respectively.

The track finding is based on a combinatorial Kalman filter [3] (KF) [59] with a dedicated Bethe Heitler [60] modeling of the electron energy losses.

The approximation of the energy loss distribution by a single Gaussian in the KF was not sufficient. A non-linear estimator which takes the actual shape of the distribution into account achieves better results. A non-linear generalization of the KF, the Gaussian Sum Filer (GSF) [61], has been applied.

The electron momentum is obtained from the combination of the ECAL and the tracker measurements. Starting from the corrected cluster energy (E), the momentum can be refined by splitting electrons into different classes and performing class dependent corrections. The tracker measurement gives the best result at low energies, as well as in the regions where the precision of the ECAL measurement is poor. In all other cases the ECAL measurement is used. The decisions are based on the energy and on the E/p distribution, which is shown in Fig. 3.7(a) for electrons coming from a $Z \rightarrow e^+e^-$ sample, with a $p_t > 20\,\text{GeV}$. In addition to that an alternative variable $1/E - 1/p$ is shown in Fig. 3.7(b). In principle both distributions contain the same information, although the $1/E - 1/p$ distribution has a better shape to cut on it, with respect to the E/p, thus the fakes can be controlled better, as shown in [62] [4].

To verify this procedure, the momentum and energy resolutions are shown, i.e.

$$\text{Resolution} = \frac{x_{\text{meas}} - x_{\text{true}}}{x_{\text{true}}} \tag{3.4}$$

[3] The KF is a optimal recursive data processing algorithm. Optimal, because it incorporates all information that can be provided to it; recursive, because the KF does not require all previous data to be kept in storage. For a more complete discussion refer to [58].

[4] By now, the official CMS reconstruction algorithm uses E/p.

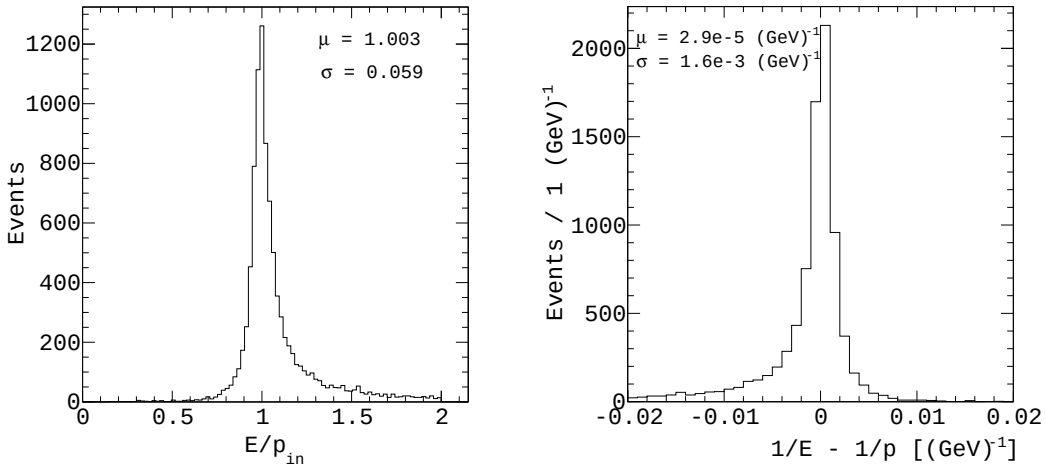

(a) (b)

Figure 3.7: Energy over track momentum (E/p_{in}) in (a) and inverse energy minus inverse track momentum ($1/E - 1/p$) in (b) distribution for electrons with $p_t > 20\,\text{GeV}$ in a $Z \to e^+e^-$ sample.

where x stands for the track transverse momentum (p_t^{trk}) and the supercluster transverse energy (E_t^{sc}). In Fig. 3.8(a) the track p_t resolution with the GSF track finder and in Fig. 3.8(b) the supercluster E_t resolution, after applying the cluster algorithm, are shown. By comparing these two plots, one sees that the supercluster E_t resolution is much better than the track p_t, mostly due to the fact that only track p_t measurements starting at a p_t of 20 GeV are considered.

Combining the track momentum and cluster energy information one obtains the resolution in Fig. 3.9. For the combined measurement a weighted mean is used, that involves the error on the supercluster energy and the error on the track momentum from the GSF fit. In Tab. 3.5 mean (μ) and sigma (σ) for a Gauss fit are listed. The values show, that there is a small overcorrection in the reconstruction.

Detector	μ	σ
GSF Track	-0.068	0.074
ECAL	-0.003	0.025
Combination	-0.002	0.025

Table 3.5: Resolution for track and ECAL cluster based electrons and for the combination.

In the early stages of the reconstruction algorithm there were some problems with the combination of the ECAL and track information. One such problem was encountered in the early days of the CMS reconstruction tools, resulting in a double counting of electrons. This was

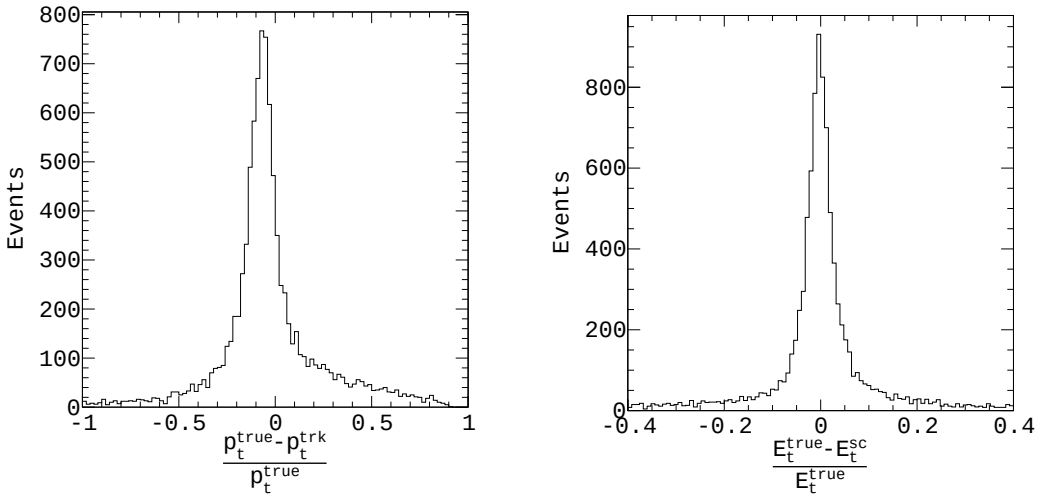

(a) (b)

Figure 3.8: Track resolution measured with the GSF track finder in (a) and energy resolution after the cluster algorithm in (b).

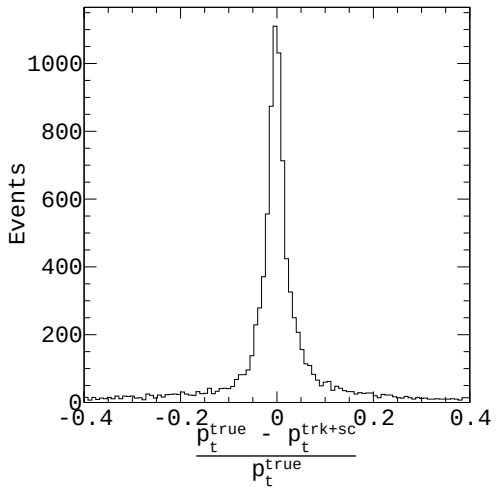

Figure 3.9: Momentum resolution for electrons combining the GSF track finding and the cluster energy information.

due to the fact that the track finder, in some cases, reconstructed two different tracks for the same energy cluster. By examining the $Z \to e^+e^-$ events and plotting the supercluster ϕ and η difference of the reconstructed electrons, one found that in some cases these two electrons were in fact the same particles, as the spike at zero in Fig. 3.10 shows. In the process of the detailed study of the Z boson reconstruction, this problem could be removed.

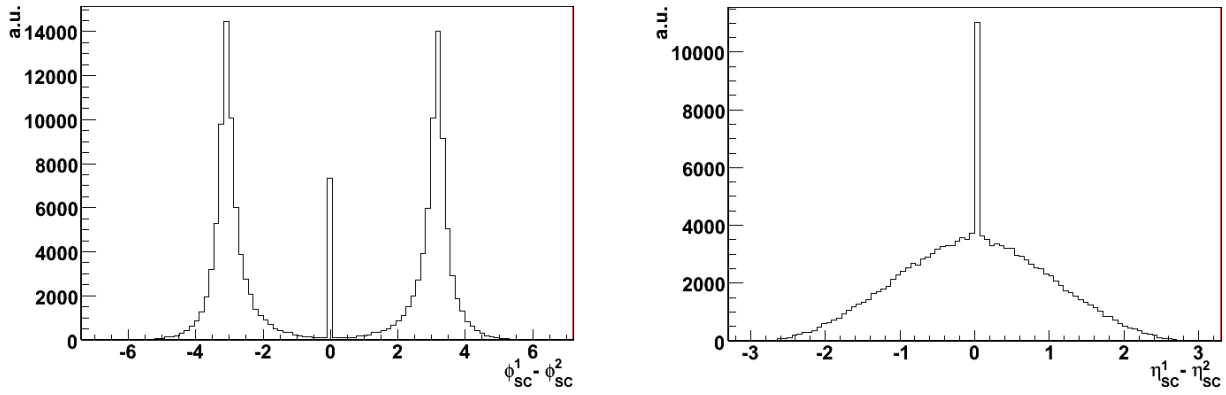

(a) (b)

Figure 3.10: Double counting problem in an early stage of the electron reconstruction in combining the track finder information with the supercluster information. $\Delta\phi$ (a) and $\Delta\eta$ (b) for the first and second electron in the event.

3.3 Isolated Electron Selection at Large p_t

In this section the electron selection will be presented, starting with the so-called electron preselection, which is used to reject mainly pions, faking an electron. To further reduce the fake rate, which arises mostly from electrons in b jets, the electrons are required to be isolated. A more specific selection will then be elaborated on, the so-called electron identification, which is tuned to reject the main backgrounds of the $Z \to e^+e^-$ events. Finally the high level trigger (HLT) for electrons will be discussed.

3.3.1 Electron Preselection

The goal of the electron preselection is to reduce the large amount of low p_t QCD events faking an electron. This is done by applying two cuts on the seeding level:

- $E_t > 4\,\mathrm{GeV}$, where E_t is the supercluster transverse energy and
- $H/E < 0.1$, where H is the energy deposited in the HCAL towers in a cone of radius $\Delta R = 0.15$ centered on the electromagnetic supercluster position and E is the energy of the electromagnetic supercluster.

With the first cut, a huge amount of low QCD jets can be rejected. With the second cut, the more energetic jets can be rejected, by looking at the energy they deposit in the HCAL and the ECAL, with the knowledge that for electrons the energy in the HCAL is small or zero.

Almost all jets are composed of neutral plus charged particles. In such a case, there is no reason for the neutral component to geometrically match the track of the charged particle. Conversely, for an electron, the geometrical matching should be nearly perfect. So, two additional variables combining tracker and ECAL information are used. These two geometrical cuts are:

- $|\Delta\eta_{in}| = |\eta_{\rm sc} - \eta^{in}_{\rm trk}| < 0.02$, where $\eta_{\rm sc}$ is the energy weighted position in η of the supercluster and $\eta^{in}_{\rm trk}$ is the tracker η coordinate of the position of closest approach to the supercluster position, extrapolating from the innermost track position.

- $|\Delta\phi_{in}| = |\phi_{\rm sc} - \phi^{in}_{\rm trk}| < 0.15$, where $\phi_{\rm sc}$ is the energy weighted position in ϕ of the supercluster and $\phi^{in}_{\rm trk}$ is the tracker ϕ coordinate of the position of closest approach to the supercluster position, extrapolating from the innermost track position.

The distributions of these observables, used in the preselection of electrons, are shown in Fig. 3.11 for electrons from $Z \to e^+e^-$ events.

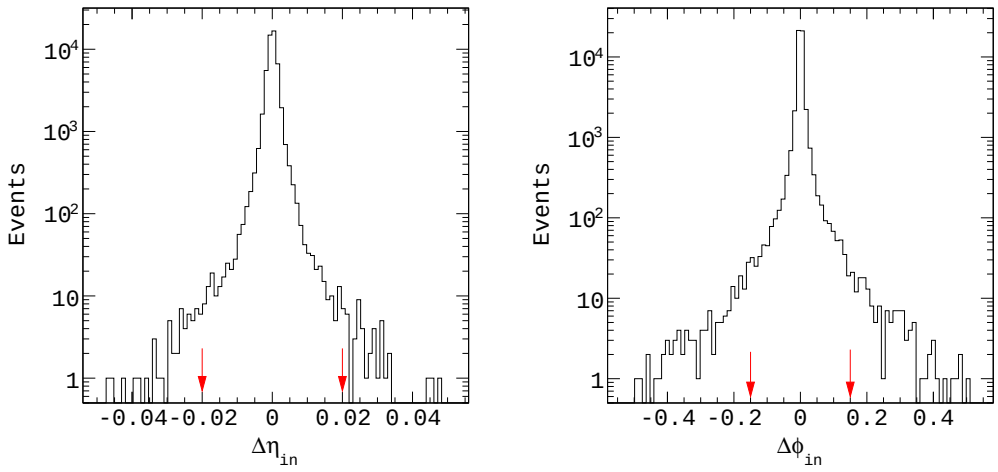

Figure 3.11: Electron preselection distributions for electrons from $Z \to e^+e^-$ events; $\Delta\eta_{in}$ (left) and $\Delta\phi_{in}$ (right); red arrows indicate the cut position.

The efficiency and the fake rate, as a function of η and p_t for electrons in $Z \to e^+e^-$ events, are shown in Fig. 3.12 and Fig. 3.14 respectively. Note that only electrons in the ECAL barrel are considered with a transverse momentum above 20 GeV. The efficiency (ϵ) is defined as

$$\epsilon = \frac{\text{no. of matched reconstructed electrons}}{\text{no. of generated electrons}} \tag{3.5}$$

where the matching between the reconstructed electrons and the generated electrons is done geometrically, with $\Delta R < 0.05$, i.e.

$$\Delta R = \sqrt{(\Delta\eta)^2 + (\Delta\phi)^2} < 0.05, \tag{3.6}$$

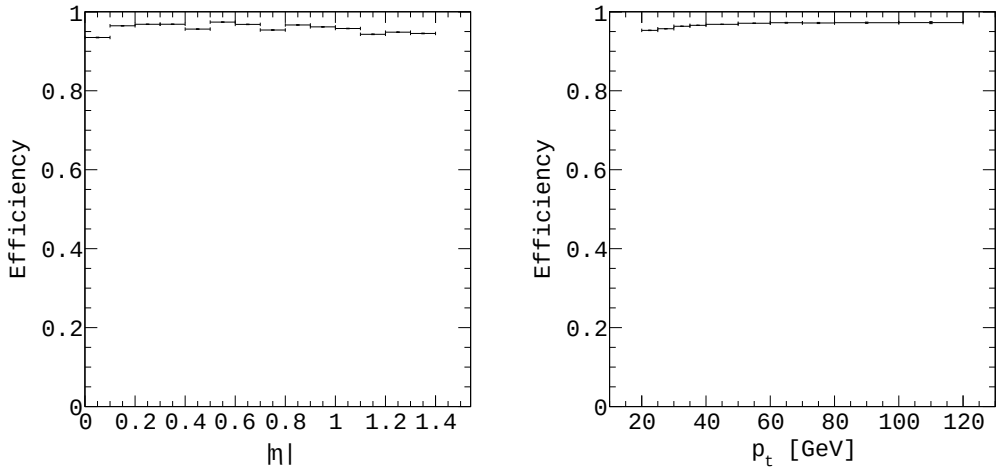

Figure 3.12: Preselection efficiency in η (left) and p_t (right) for electrons within the ECAL barrel and $p_t > 20\,\text{GeV}$.

where $\Delta\eta = \eta_{\text{gen}} - \eta_{\text{reco}}$, same for ϕ. As shown in Fig. 3.13, the threshold ($\Delta R < 0.05$) is small enough to reject fake electrons and big enough to accept real electrons.

The fake rate is defined as

$$\text{Fake Rate} = \frac{\text{no. of not-matched but reconstructed electrons}}{\text{no. of generated jets}}, \tag{3.7}$$

where not-matched electrons is defined as electrons that fail the matching with the generated electrons.

In Tab. 3.6 the efficiency and the fake rate after preselection are summarized. The values are taken from a constant fit on the η distributions.

	Efficiency	Fake Rate
Preselection	0.974 ± 0.015	0.0232 ± 0.010

Table 3.6: Efficiency and fake rate after preselection in η for electrons within the ECAL barrel and $p_t > 20\,\text{GeV}$.

After the preselection the number of fake electrons is of the order of 2% of all generated jets. The efficiency is over 95%, which is already quite promising. This is due to the fact that we are dealing with a hadron collider, where high p_t leptons are rare in comparison to hadronic final state. In the next section we add another tight constraint, the isolation, which will help us to further reduce the fake rate.

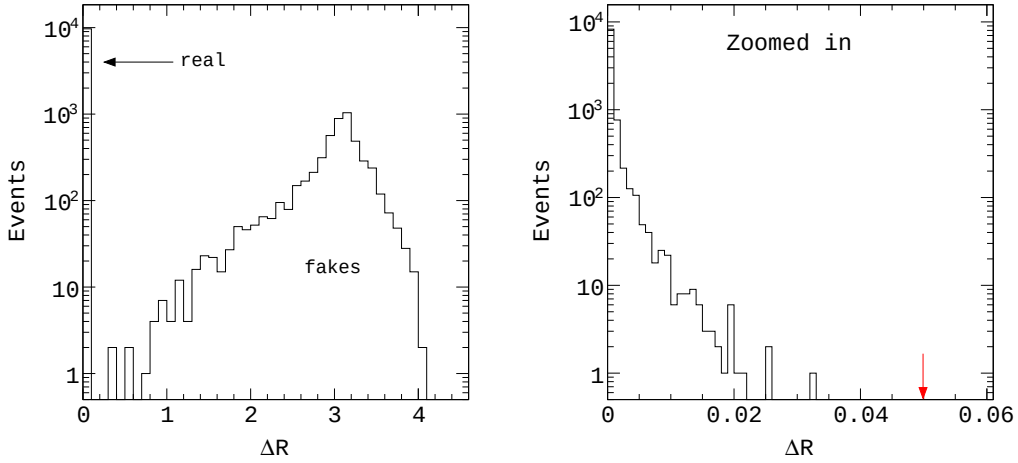

Figure 3.13: Matching variable ΔR used to select real electrons and reject fake electrons. The whole width (left) and zoomed in (right) to the real electrons. The red arrow indicates the threshold.

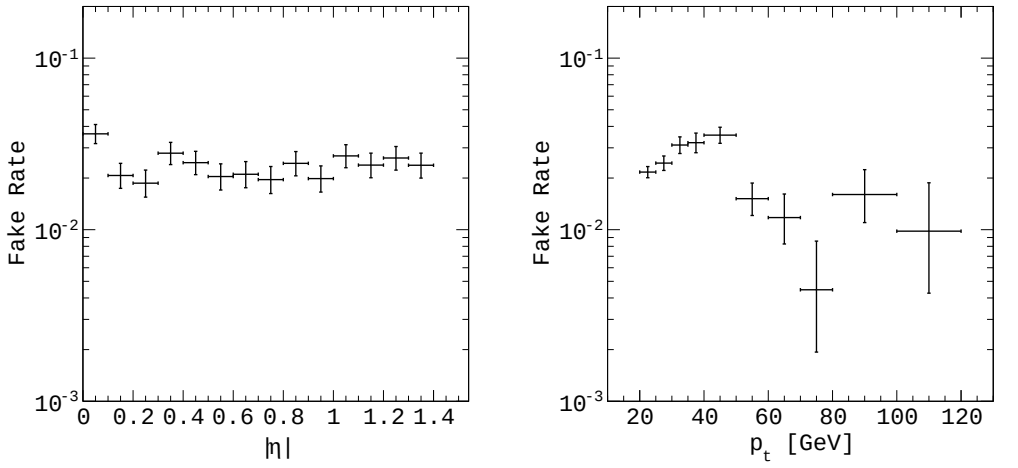

Figure 3.14: Preselection fake rate in η (left) and p_t (right) for electrons within the ECAL barrel and $p_t > 20\,\text{GeV}$ for the inclusive $pp \to \gamma/Z \to e^+e^-$ sample.

3.3.2 Electron Isolation

The most important selection to reject the jet background is the isolation. The electron isolation can be done with three different detector parts, the tracker, the ECAL and the HCAL detector. The isolation variables are p_t or E_t sums in cones (R_{out}) in (η, ϕ) space with inner veto areas (R_{in}) to remove the electron footprint and recover as much radiated energy as possible. The use of an inner cone instead of just adding all track momenta in the outer cone and then dividing by the electron energy, avoids the problem that the electron energy could be mis-measured. A picture of the geometrical set-up is shown in Fig. 3.15. The isolation variable is

$$p_t^{\text{iso}} = \sum_i p_{t_i} \tag{3.8}$$

where p_{t_i} are momenta of tracks in the outer cone around the selected electron [5]. In Tab. 3.7 the relevant values are summarized.

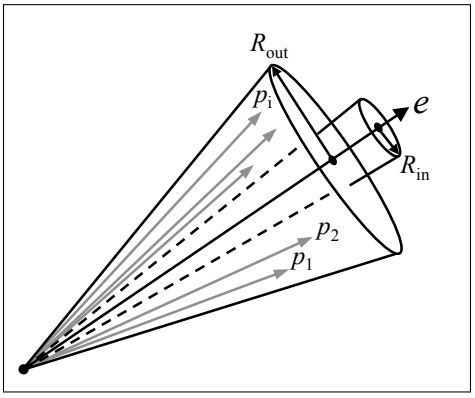

Figure 3.15: Picture of the geometrical set-up for the isolation with inner veto cone (R_{in}) and outer cone (R_{out}).

Variables	Tracker	ECAL	HCAL
ΔR_{in}	0.015	0.045	0.15
ΔR_{out}	0.4	0.4	0.4
$p_{t_{\text{min}}}$ or E_{noise}	1.5 GeV	0.08 GeV	0.9 GeV

Table 3.7: Relevant values for tracker, ECAL and HCAL electron isolation, with ΔR_{in} the inner veto cone and R_{out} the outer cone. The $p_{t_{\text{min}}}$ and E_{noise} are the minimal values for considering a track.

Much effort has been invested to determine the best values for the isolation, whereas the values here are based on a MC study. An example can be found in [63]. For real data, these values

[5] Same for the transverse energy in the ECAL and HCAL detector.

can be considered as a good starting point and of course they can be adjusted.

In Fig. 3.16 the $\sum p_t$ and $\sum E_t$ distributions for the three electron isolation variables for the signal and background are shown. The electron is called isolated, if $\sum p_t$ or $\sum E_t$ is smaller than a certain value.

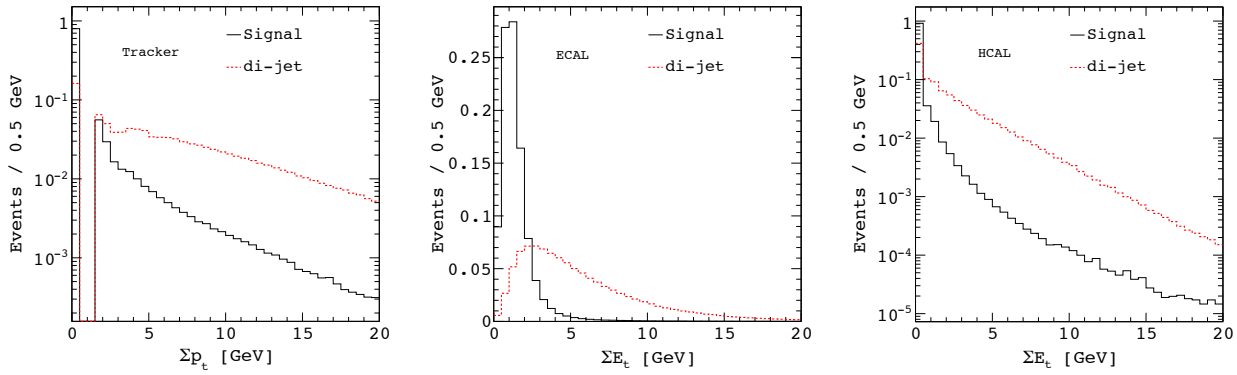

Figure 3.16: $\sum p_t$ and $\sum E_t$ distributions for the electron isolation variables; tracker (left), ECAL (center) and HCAL (right) isolation. Signal and background distributions are normalized to unity.

3.3.3 Electron Identification

For the early data it is convenient to use a cut based analysis, which uses only a few simple and well understood variables. In this section the cut based electron identification will be presented.

The electron identification uses, in principal, the same variables as the preselection, except for a shower shape variable. The geometrical cuts $\Delta\eta_{in}$ and $\Delta\phi_{in}$ and a new calorimeter shower shape variable $\sigma_{i\eta i\eta}$ [6] are used. The latter is the width of the ECAL cluster along the η direction, computed for all the crystals in the 5×5 block of crystals centered on the highest energy crystal of the seed cluster, i.e.

$$\sigma_{i\eta i\eta} = \sqrt{\frac{\sum_i^{5\times5} \left(0.0175 \cdot \eta_i^{\text{xtal}} + \eta_{\text{seed}}^{\text{xtal}} - \bar{\eta}_{5\times5}^{\text{xtal}}\right)^2 \cdot w_i}{\sum_i^{5\times5} w_i}}, \tag{3.9}$$

with $w_i = 4.2 + \ln(E_i/E_{5\times5})$, η_i^{xtal} denote the numbers of the crystal (= xtal), $\eta_{\text{seed}}^{\text{xtal}}$ is the number of the seed crystal and $\bar{\eta}_{5\times5}^{\text{xtal}}$ is the number of the mean crystal in the 5×5 block.

The reason for the use of the crystal number and not the pseudorapidity value, is that $\sigma_{\eta\eta}$ [7] does not perform well near gaps, as shown in [64]. In Fig. 3.17 the electron identification variables

[6] Recently $\sigma_{i\eta i\eta}^{\text{sc}}$ was introduced; it has the same definition of the default $\sigma_{i\eta i\eta}$ variable, but the sum is computed for all the crystals belonging to the electron supercluster. Despite the higher rejection power this variable is probably more sensitive to ECAL noise. On going studies are verifying the actual benefit.

[7] Same definition as for $\sigma_{i\eta i\eta}$, except using pseudorapidity values instead of crystal numbers.

are shown. One sees very clearly that the background is flat, compared to the signal, or in the case of the shower shape variable it is much wider.

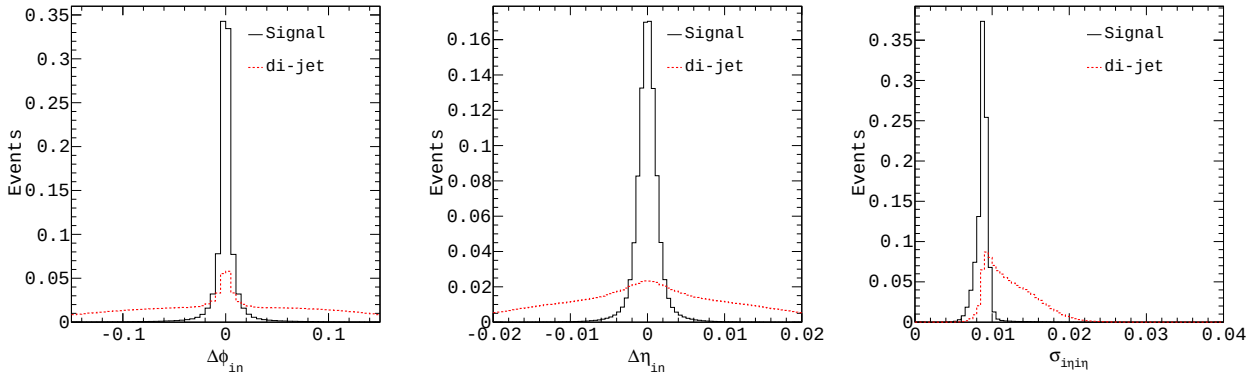

Figure 3.17: $\Delta\phi_{in}$, $\Delta\eta_{in}$ and $\sigma_{i\eta i\eta}$ distributions for the electron identification variables; ϕ matching (left) and η matching variable (center) and shower shape variable (right). Signal and background distributions are normalized to unity.

3.3.4 High Level Trigger

For this selection the following HLT trigger was used: `HLT_Ele15_SW_LooseTrackIso_L1R`, which means, a single isolated (`LooseTrakIso`) electron (`Ele15`) trigger with start-up conditions (`SW`) and relaxed L1 seeding (`L1R`). The selection cuts applied are given in Tab. 3.8.

Variable	Single Electron
E_t	$> 15\,\text{GeV}$
p_t^{iso} or p_t^{iso}/p_t^e	$< 8\,\text{GeV}$ or < 0.5

Table 3.8: HLT cuts for the electron streams; transverse energy (E_t) and isolation variables (p_t^{iso} or p_t^{iso}/p_t^e).

The HLT efficiency will be shown in section 3.5, where isolation, identification and HLT efficiencies will be discussed in detail.

3.4 Z Boson Reconstruction

After having shown the single electron selection in the previous section, it will now be applied to reconstruct the Z boson. In the first section the Z boson reconstruction, will be elaborated on. Then, the electron charge misidentification problem will be briefly discussed. Finally the Z boson background in the mass region will be shown.

3.4.1 Z Reconstruction

The starting point of the Z reconstruction is the dielectron selection, where the preselection shown in section 3.3.1 is used. In addition to the preselection, a transverse momentum ($p_t > 20\,\text{GeV}$) and a pseudorapidity ($|\eta| < 1.44$) cut on the electrons are applied.

The 4-momentum of all electron/positron pairs, in events with more than one electron are added up in all possible ways [8], i.e.

$$P_Z = \sum_{i \neq j} P_{e_i} + P_{e_j}, \tag{3.10}$$

where P is the 4-momentum.

In Fig. 3.18 the invariant Z boson mass distribution, for $\mathcal{L}_{int} = 1.4\,\text{fb}^{-1}$ (MC) and for $\mathcal{L}_{int} = 10\,\text{pb}^{-1}$ (pData) defined in section 3.1, is shown. The MC distribution is normalized to $\mathcal{L}_{int} = 10\,\text{pb}^{-1}$ to be compared with the pseudo data set.

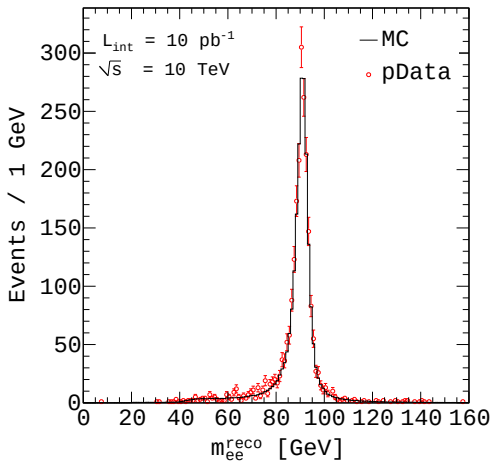

Figure 3.18: The distributions shows the invariant Z boson mass after preselection, for $\mathcal{L}_{\text{int}} = 10\,\text{pb}^{-1}$ (red circles) data like together with the expected distribution $\mathcal{L}_{\text{int}} = 1.4\,\text{fb}^{-1}$ (black line) normalized to $10\,\text{pb}^{-1}$.

The goal of the electron isolation and identification for the Z boson reconstruction, was to use only a few simple and robust variables. It is easy to select the signal, due to the rarity of isolated high p_t leptons in pp collider, which enabled us to keep the number of cut variables to a minimum [65]. In Tab. 3.9 the relevant values for the isolation and identification variables are summarized.

The invariant Z mass peak after these selections is shown in Fig. 3.19, focuses on the mass peak, of main interest here. In Tab. 3.10 the number of reconstructed Z's in the peak ($\sim 3\Gamma_Z$) after the whole selection are listed.

[8] $\binom{n}{2}$, with n number of electron/positron.

Isolation			Identification		
$\sum p_t^{\mathrm{Trk}}$	$\sum E_t^{\mathrm{Ecal}}$	$\sum E_t^{\mathrm{Hcal}}$	$\lvert\Delta\phi_{in}\rvert$	$\lvert\Delta\eta_{in}\rvert$	$\sigma_{i\eta i\eta}$
7.2 GeV	5.7 GeV	8.1 GeV	0.1	0.007	0.01

Table 3.9: Electron isolation and identification criteria for $Z \to e^+e^-$ candidates.

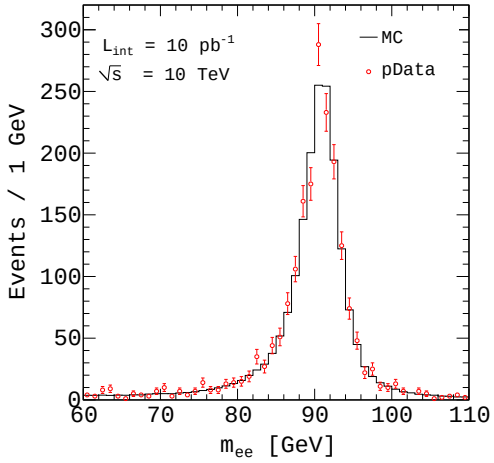

Figure 3.19: Invariant Z boson mass peak, reconstructed with electrons passing the whole selection chain.

Cuts	Z Candidates	%
$p_t > 20\,\mathrm{GeV}$, $\lvert\eta\rvert < 1.44$ (generator level)	1 858	100
Preselection, $p_t > 20\,\mathrm{GeV}$ & $\lvert\eta\rvert < 1.44$ (reconstruction)	1 813	98
HLT, Isolation & Identification (reconstruction)	1 602	86

Table 3.10: Number of Z's in the mass peak ($\sim 3\Gamma_Z$) with and without electron isolation and identification criteria.

One method to verify if the cuts are robust is to vary them and count the number of remaining Z's in the peak. In a robust cut based analysis, the cuts should be chosen such that the number of Z candidates does not depend strongly on the cut value, i.e. small changes (δ) of the variables, have small or no effect on the signal. In Tab. 3.11 the number of Z candidates, after varying the cuts of about $\delta = \pm 5\%$, are listed.

Variable	$\delta = -5\%$	$\delta = 0$	$\delta = +5\%$
$\lvert\Delta\phi_{in}\rvert$	1 803	1 806	1 806
$\lvert\Delta\eta_{in}\rvert$	1 789	1 791	1 794
$\sigma_{i\eta i\eta}$	1 537	1 729	1 778
$\sum p_t^{\mathrm{Trk}}$	1 711	1 716	1 720
$\sum E_t^{\mathrm{Ecal}}$	1 774	1 778	1 784
$\sum E_t^{\mathrm{Hcal}}$	1 808	1 809	1 809

Table 3.11: Number of Z candidates in the mass peak, after varying the cuts of about $\pm 5\%$.

By looking at the values in Tab. 3.11, one can state that $|\Delta\phi_{in}|$ and $|\Delta\eta_{in}|$ are robust, even with $\delta = \pm 10\%$, the number of Z candidates does not change significantly. The most critical cut is the $\sigma_{i\eta i\eta}$, where the number of Z's differ by more than 10%. This implies that the error in counting the number of Z's using these identification cuts will be dominated by the $\sigma_{i\eta i\eta}$ cut. However for the electron identification the shower shape variable is mandatory.

The same has been done with the isolation cut variables and the results are listed also in Tab. 3.11. The values show that the isolation cuts are similarly robust.

Up to now, only events where the electron and the positron fulfill the selection criteria, so-called hard-hard events, were considered. It would be of interest to know how many Z's could be reconstructed by relaxing one (hard-soft) of the two electrons or both (soft-soft) cuts. In Tab. 3.12 the number of additional Z candidates are listed, by relaxing at least one electron. We call an electron relaxed if it fulfills only the electron preselection, i.e. no electron isolation and no electron identification, as described above.

	generated	hard-hard	hard-soft	soft-soft
Number of Z's	1858	1 602	118	23
%	100	86	6.4	1.2

Table 3.12: Number of reconstructed Z events within the mass peak (hard-hard), after relaxing one (hard-soft) or two (soft-soft) electrons, compared with the number of generated Z events with $p_t > 20\,\mathrm{GeV}$ and $|\eta| < 1.44$.

Already in the early phase of the experiment (a few pb^{-1} of integrated luminosity) maximizing the Z boson selection efficiency is no longer a priority. In addition, as demonstrated above, relaxing the cuts does not result in a large increase in the number of Z candidates.

3.4.2 Electron Charge Misidentification

The electron charge misidentification is a problem in the electron reconstruction. The main reason for the electron charge misidentification is due to photon conversion, i.e. an electron emitting very early (1^{st} pixel layer) a hard photon (γ), wherein the photon immediately converts into an electron and a positron. The reconstruction algorithm has two possibilities to reconstruct the track of the electron, as shown in Fig. 3.20.

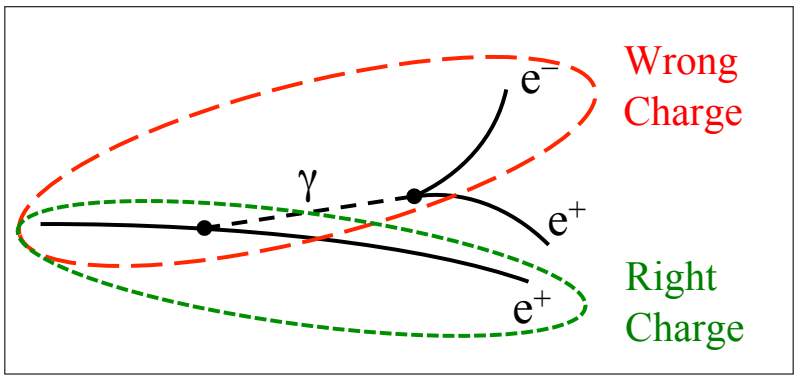

Figure 3.20: Draft of an electron charge misidentification by photon conversion.

With the Z boson mass peak the electron charge misidentification rate can be calculated quickly. Instead of adding up all possible combinations of electron/positron 4-momentum, one adds up only 4-momenta with the same charge. By counting the number of events with an invariant mass in the Z peak region ($\sim 3\Gamma_Z$) and normalizing by the total number of Z events given in Tab. 3.10, one gets the charge misidentification rate [9]. In Fig. 3.21 the invariant Z mass for events passing the whole selection chain, with the additional condition to reconstruct the Z with two same sign electrons, is shown for $\mathcal{L}_{\mathrm{int}} = 10\,\mathrm{pb}^{-1}$.

The number of so-called same sign events in the Z mass region can be compared with the number of events, where at least two electrons were reconstructed, in which one had the wrong charge. To identify if the charge is reconstructed correctly, the electron is matched with the generated electrons, where the charge is known. In Tab. 3.13 these values are compared. For the Z candidates one has to consider that the misidentification rate is not $N_{\mathrm{wrong}}/N_{\mathrm{tot}}$ but $N_{\mathrm{wrong}}/2N_{\mathrm{tot}}$ because in each Z event, there are 2 reconstructed electrons.

This small mis-identification could become important for potential asymmetry measurements with W and Z, especially for W's, where the charge of the electron defines the charge of the W. In addition, the fact that for example the charge of one of the electrons in the full leptonic decay of $t\bar{t}$ or $W^{\pm}W^{\mp}$ events can be misidentified, could be a problem for new physic searches.

[9] Since the rate is quite small, the possibility to have two wrong identifications in one event, is negligible.

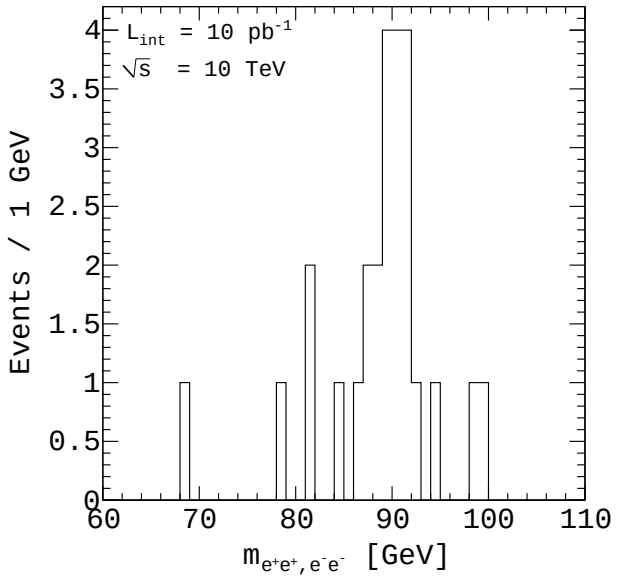

Figure 3.21: Invariant Z mass for events with two same sign electrons.

Variables	N_{wrong}	N_{tot}	%
Same sign Z events in the mass peak ($\sim 3\Gamma_Z$)	34	1 636	1.1
Misidentified electrons	34	4 364	1.2

Table 3.13: Number of same sign Z events in the mass peak, compared with the number of misidentified electrons.

This kind of background is about 25% of all the backgrounds to same sign dielectron SUSY searches [66].

A method was developed to reduce the mis-identification rate for electrons by identifying photon conversions. Conversion candidates are reconstructed using a vertex fit with a three-dimensional conversion constraint. This method improves the electron charge identification, with a reduction in the charge misidentification rate of about 30%, referring to [67].

3.4.3 Backgrounds

Other processes can produce events that mimic the signature of $Z \to e^+e^-$ events in our detector. Some of these have similar final-state event topologies to those of our signal sample and others can fake similar topologies if a non-electron object within the event is misidentified as an electron. We separate the background sources into two main categories: events in which hadronic jets fake an electron and events from other electroweak processes. For the hadronic events, two jets are faking electrons, so-called di-jet events and for the electroweak events, there are generally two processes:

- $W \to e\nu +$ jets, where one jet fakes an electron and

- $\gamma^*/Z \to \tau\tau$, where the τ's decay to electrons, which are identified wrongly as primary electrons.

As shown in [68] the τ background can be neglected, as long as one considers only candidates in the Z mass peak. An additional background, which is a combination of the QCD and the electroweak background, is the $t\bar{t}$ background. Since the top quark decays practically always into a W boson and a b-quark, one gets two opposite sign electrons coming from the W's decaying in the electron channel and at least two jets coming from the quarks. The majority of the fakes will come from the W decaying to electrons and neutrinos, though some fakes will come from the b-quark decaying to electrons. The smallest fraction will be from hadronic jets, faking an electron. In Fig. 3.22 these backgrounds are shown with the Z boson mass distribution. The number of background events within the Z boson mass peak ($\sim 3\Gamma_Z$) is listed in Tab. 3.14.

Process	N_{sel}
$Z \to ee$	$1\,602 \pm 40$
Di-jet	< 0.01
$W + jets$	0.4
$t\bar{t}$	1.1
Total background	1.5 ± 1.2

Table 3.14: Z boson background within the mass peak ($\sim 3\Gamma_Z$).

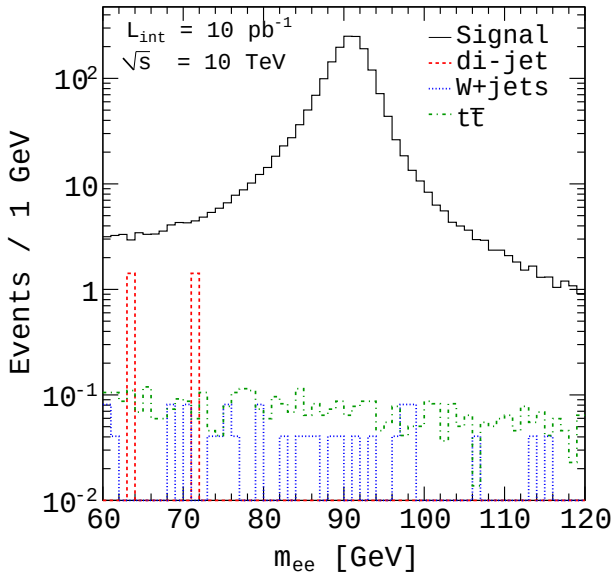

Figure 3.22: Z boson mass distribution with di-jet (red dashed line), W+jet (blue dotted line) and $t\bar{t}$ (green dashed-dotted line) background.

The statistical error on the number of Z candidates within the mass peak for $10\,\mathrm{pb}^{-1}$ is ± 40, therefore the background can be neglected [10].

3.5 Efficiency

In this section, the efficiency measurement will be described. First the purely MC based efficiency will be calculated and then a data driven method of computing the efficiency, the so-called Tag and Probe (T&P) method, will be applied. The data driven method can currently only be studied with MC, i.e. the pseudo data sample.

3.5.1 Monte Carlo

For the MC efficiency one tries to adapt the simplest method. With the generator level information one knows exactly which particle is an electron coming from a Z decay. By comparing the number of electrons which were generated, with the number of electrons which were reconstructed and passed all the selection and identification criteria, one knows the overall efficiency. In order to ensure, the right reconstructed electron is compared with the corresponding generated electron, geometrical matching is done, i.e.

$$\Delta R = \sqrt{(\Delta\phi)^2 + (\Delta\eta)^2}, \tag{3.11}$$

[10] The first data arriving at the moment I'm writing this section, show a very nice agreement between data and MC for real electrons and background electrons, which gives even more confidence in neglecting this small background.

where $\Delta\eta = |\eta_{\text{gen}} - \eta_{\text{reco}}|$, same for ϕ. The MC efficiency (ϵ_{MC}) is then defined as

$$\epsilon_{\text{MC}} = \frac{\text{reconstructed matched electrons, passing all criteria}}{\text{generated electrons}} \tag{3.12}$$

In Fig. 3.23 the electron MC efficiency for the pseudorapidity η and for the transverse momentum p_t is shown.

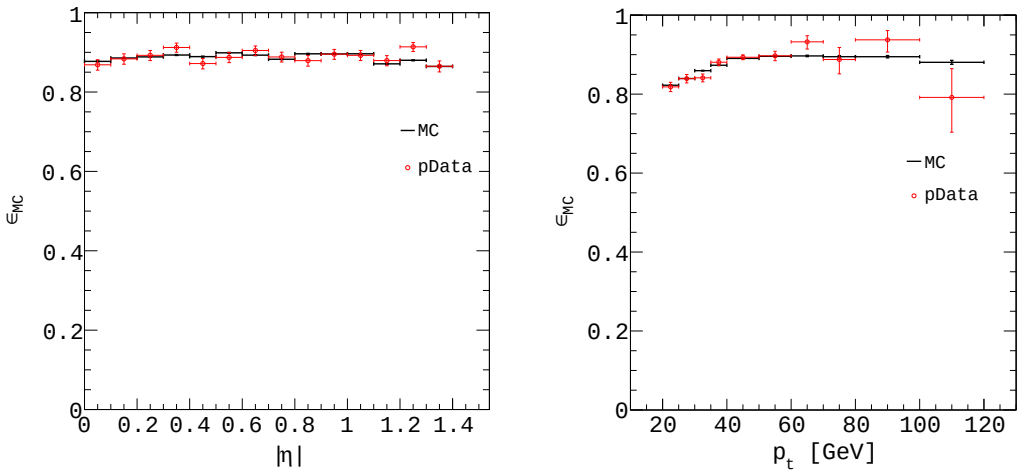

Figure 3.23: Electron MC efficiency for the MC sample (black line) and the pseudo data (red circles) for the pseudorapidity (left) and transverse momentum (right).

The efficiency is obtained, by fitting a constant function to the η distribution,

$$\epsilon_{\text{MC}} = 0.897 \pm 0.015.$$

The preselection efficiency was determined to be 97%. The entire selection reduces the efficiency by 8%. In contrast, the background is negligible.

3.5.2 Tag and Probe

One of the most critical elements in any analysis of early data will be accurate efficiency measurements. Such data reliance on efficiency predictions from MC simulation will produce large systematic errors due to imperfections in modeling the detector response. Therefore, we would like to measure efficiencies from the data itself, with no reference to the simulation. One established data driven approach is the "tag and probe" method.

The method utilizes a known resonance (e.g J/Ψ or Z) to select particles of the desired type, and probe the efficiency of a particular selection criterion on those particles. The "tag" is an object, here an electron, that passes a set of selection criteria. The selection criteria used for the tag are listed in the previous sections. It is important, that the fake rate of passing tag selection criteria is very small ($< 1\%$). In fact the fake rate is negligible as shown in section 3.4.3.

A set of the desired particle type known as "probe" is selected by pairing these objects with tags,

such that the invariant mass of the combination is consistent with the mass of the resonance (here $\sim 3\Gamma_Z$). The efficiency itself is measured by counting the number of probe particles that pass the desired selection criteria (P_{pass}) over the total number of probes counted using the resonance (P_{all}), i.e.

$$\epsilon_{\text{T\&P}} = \frac{P_{\text{pass}}}{P_{\text{all}}} \tag{3.13}$$

The selection criteria are divided in four steps:

- P^1_{all}: $e^{\pm}$ with a ECAL supercluster; P^1_{pass}: $e^{\pm}$ passing the preselection (sc $\mapsto$ reco)
- P^2_{all}: $e^{\pm}$ passing the preselection; P^2_{pass}: $e^{\pm}$ being isolated (reco $\mapsto$ iso)
- P^3_{all}: $e^{\pm}$ being isolated; P^3_{pass}: $e^{\pm}$ passing the identification cuts (iso $\mapsto$ eid)
- P^4_{all}: $e^{\pm}$ passing the identification cuts; P^4_{pass}: $e^{\pm}$ being triggered (eid $\mapsto$ hlt).

The starting point is, of course, the supercluster condition, since there is no electron reconstruction without supercluster. In Fig. 3.24 the supercluster efficiency is shown, i.e. matched electrons with a supercluster over generated electrons and as expected the efficiency is almost 1.

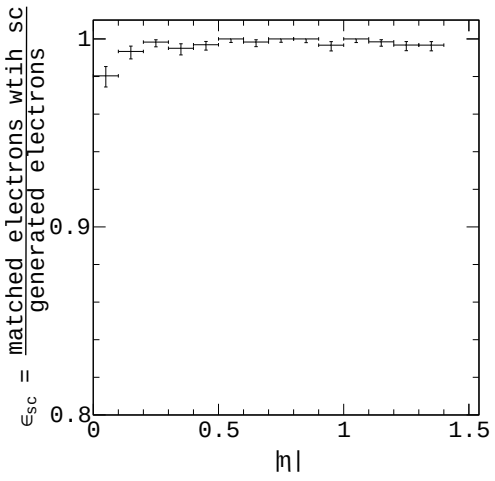

Figure 3.24: Supercluster MC efficiency, i.e. matched electrons with a supercluster over generated electrons.

It is important to be aware of the small bias in the T&P method. The bias causes the T&P efficiency measurement to be lower than the true efficiency. It arises due to the fact, that two scenarios are possible for the probe electron, it can either pass or not pass the tag electron selection. If the probe passes the tag electron selection then we will have a "tag-tag" event. In this case the efficiency of the tag electron to pass the probe criterion is measured. If the probe does not pass the criteria to be a tag we have a "tag-probe" event. Tags in such events do not get their efficiencies counted. Solutions to this bias are explained in [69]. It is also shown in [69] that the effect for not so tight tag conditions, as used here, is quite small.

In Figs. 3.25 and 3.26 the T&P efficiencies for the four steps are shown and compared with the MC efficiency, where instead of using the Z boson mass peak, a matching with the generated electrons is used.

The electron T&P efficiencies for the four steps are listed in Tab. 3.15, by fitting in first approximation a constant to the η distributions, even if not all the distributions are actually constant. However the error due to this approximation is small as one can see in the table below.

	$\mathrm{sc} \mapsto \mathrm{reco}$	$\mathrm{reco} \mapsto \mathrm{iso}$	$\mathrm{iso} \mapsto \mathrm{eid}$	$\mathrm{eid} \mapsto \mathrm{hlt}$
Efficiencies	0.985 ± 0.008	0.970 ± 0.011	0.975 ± 0.005	0.976 ± 0.018

Table 3.15: Electron T&P efficiencies for the four steps, by fitting a constant on the η distributions.

For electrons the total efficiency can be found, by multiplying the four sequential measurements, i.e.

$$\epsilon_{\mathrm{total}} = \epsilon_{\mathrm{reco}} \times \epsilon_{\mathrm{iso}} \times \epsilon_{\mathrm{eid}} \times \epsilon_{\mathrm{hlt}}. \tag{3.14}$$

The total electron T&P efficiency is

$$\epsilon_{\mathrm{total}} = 0.910 \pm 0.022.$$

in agreement with the MC efficiency of $\epsilon_{\mathrm{MC}} = 0.897 \pm 0.015$, where the reconstructed electron is compared/matched with the generated electron.

3.6 First Data

In this section a few comparison plots for the first real data events are shown. After having collected almost $5\,\mathrm{nb}^{-1}$ some real measured electron distributions can be compared with MC, whereas we are still looking on minimum bias events. The first real Z boson was also detected within these few events and will be shown in this section.

3.6.1 First Real Electrons

Within these few nb^{-1} of integrated luminosity, about 4 000 electrons with $p_t > 10\,\mathrm{GeV}$ were collected. However, these electrons are manly fake electrons produced in minimum bias events. To compare the electrons of minimum bias events with MC, the following data sample was used:

`/MinimumBias/Commissioning10-GOODCOLL-Jun14thSkim_v1/RECO`.

containing 125 M events from run 131511 to run 135802. The `GOODCOLL` offline skim performs an OR between the following requirements:

- presence of crossing bunches, of the collision trigger and veto on beam background from beam halo and splash events.

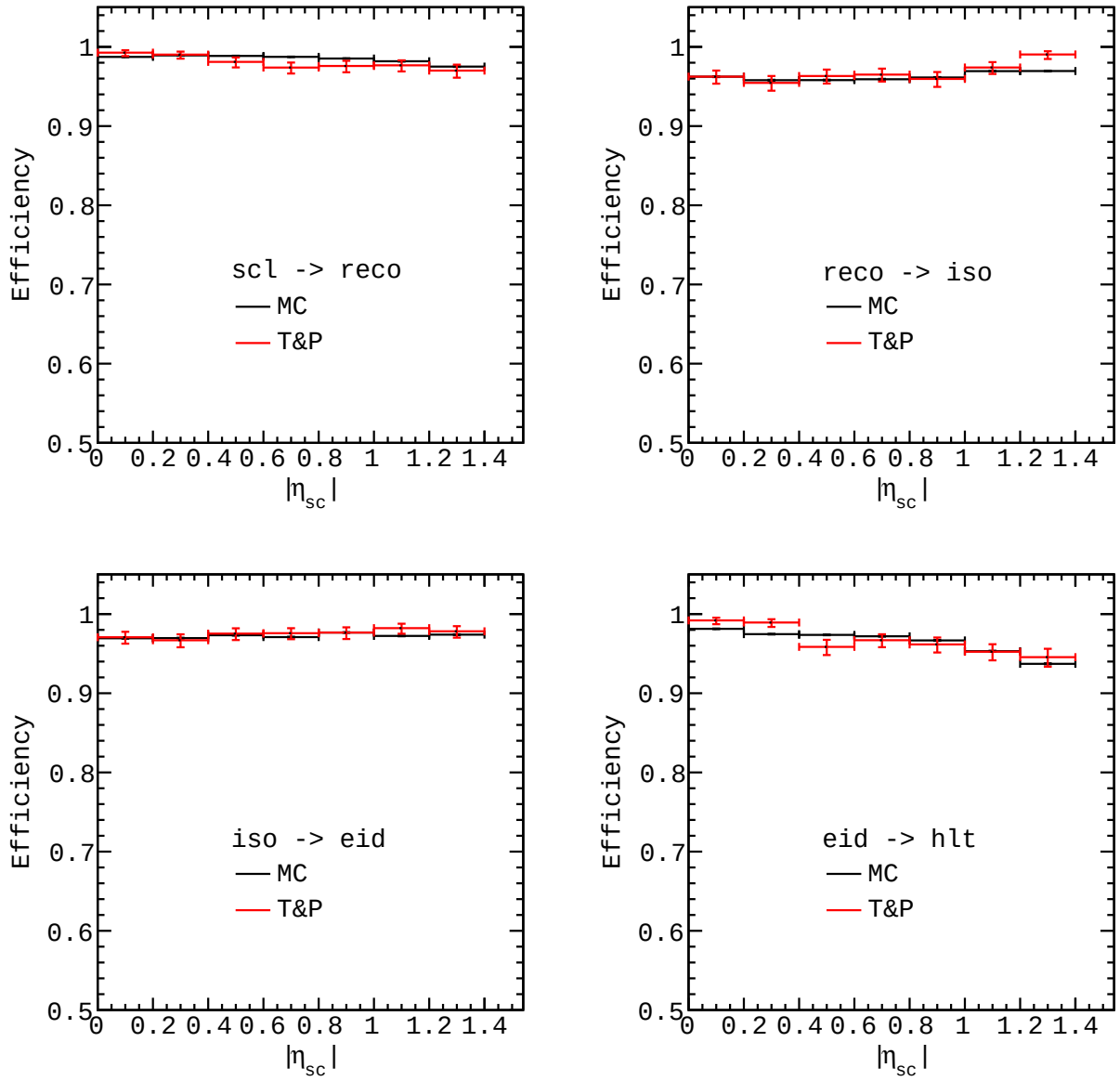

Figure 3.25: Electron reconstruction efficiency measurements as a function of the supercluster η in $Z \to e^+e^-$ sample for the four steps.

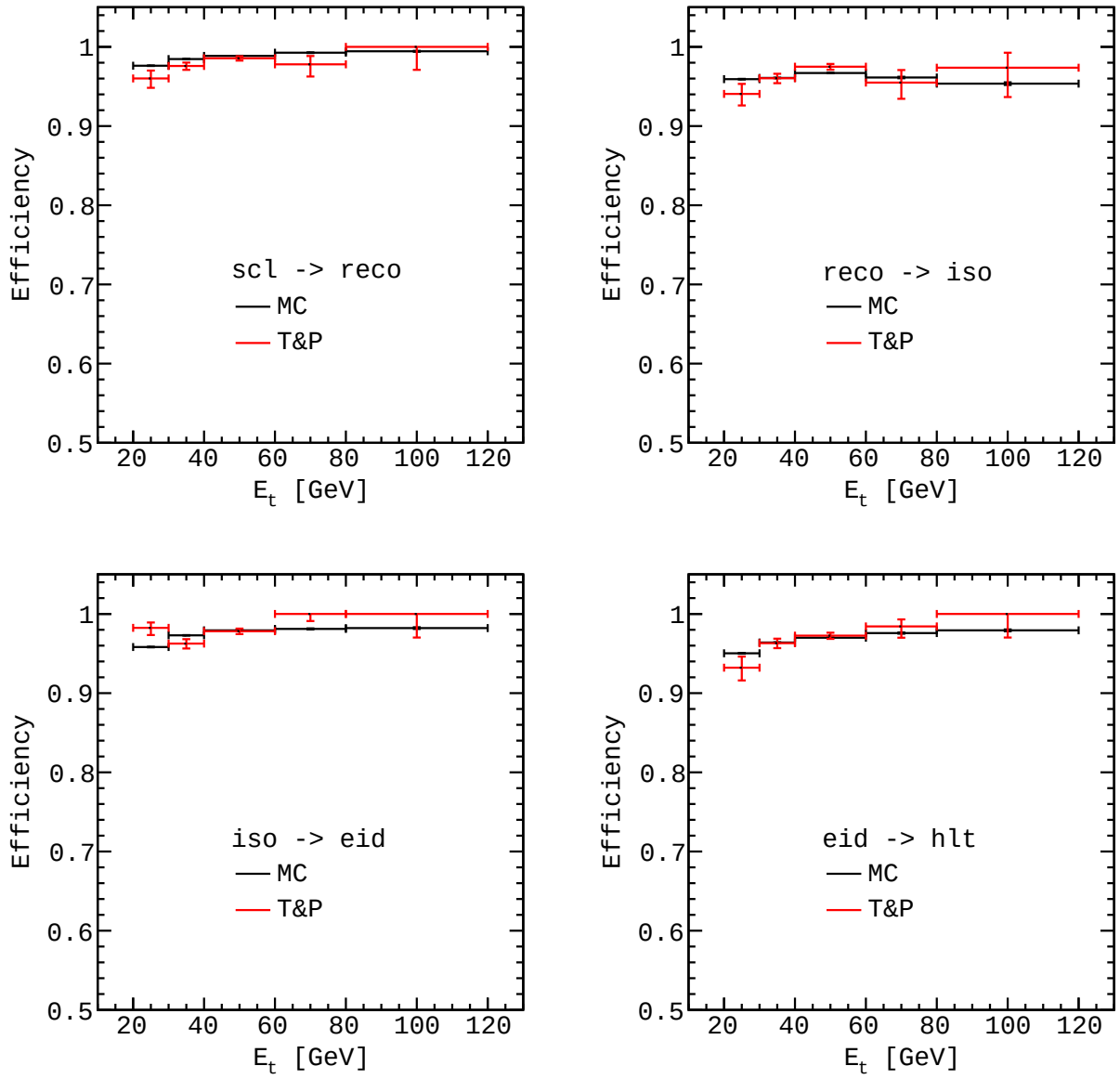

Figure 3.26: Electron reconstruction efficiency measurements as a function of the supercluster E_t in $Z \to e^+e^-$ sample for the four steps.

- presence of a good vertex, with more than 4 tracks attached to it.

Electron are reconstructed offline by applying the described electron reconstruction. With one difference, the minimal electron transverse momentum is 10 GeV and not 20 GeV.

First the three identification variables $\Delta\eta_{in}$, $\Delta\phi_{in}$ and $\sigma_{i\eta i\eta}$ will be compared with an appropriate MC sample. In Fig. 3.27 these variables are shown.

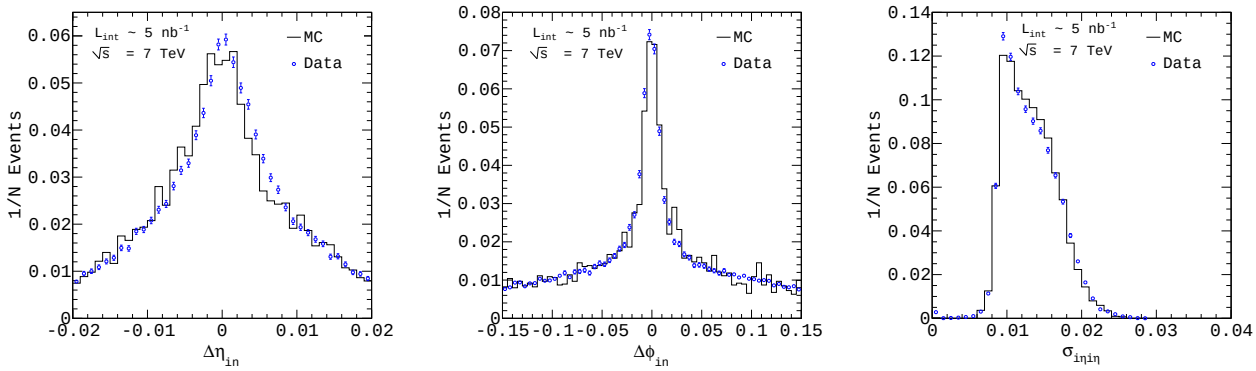

(a) (b) (c)

Figure 3.27: Electron selection variable distributions for data (blue circle) and MC (black line).

The agreement is already quite good for these variables. The shape looks much different to what was shown in Fig. 3.17 for electrons. This is due to the fact that these are mainly fake electrons.

The next important variables are the isolation variables. In Fig. 3.28 the track, ECAL and HCAL isolation are shown [11].

The agreement is quite good and allows the comparison of p_t and η distributions for electrons passing the whole selection, i.e. identification and isolation. In Fig. 3.29 these variables are plotted. These plots show already that the agreement between simulation and MC for electrons within the barrel is good.

3.6.2 First Real Z Event

On April, 25^{th} 2010 the first Z candidate has been measured within CMS. With the CMS standard event display the electron and the positron (blue) are nicely visible in the ρ-ϕ plane of the detector (Fig. 3.30). The upper particle, reconstructed with a positive charge, is surrounded by high p_t tracks. The lower particle, reconstructed with a negative charge, is isolated.
The relevant parameters of the positron and electron and also the cut variables for these two particles are listed in Tab. 3.16.

The comparison of these values with the discussed selection shows that the electron is in the

[11] The color of the data points is blue, to distinguish clearly from the pseudo data points, which are red.

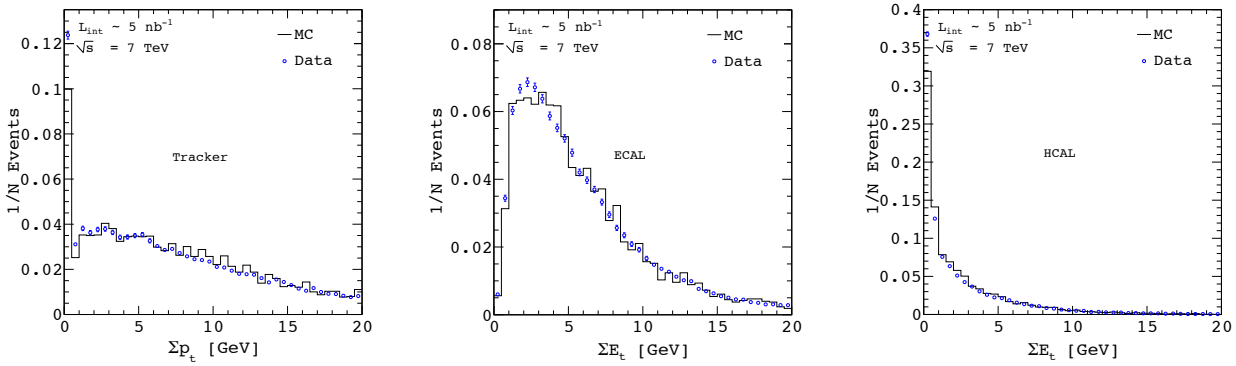

(a) (b) (c)

Figure 3.28: Electron isolation variable distributions for data (blue circle) and MC (black line); track (a), ECAL (b) and HCAL isolation in (c).

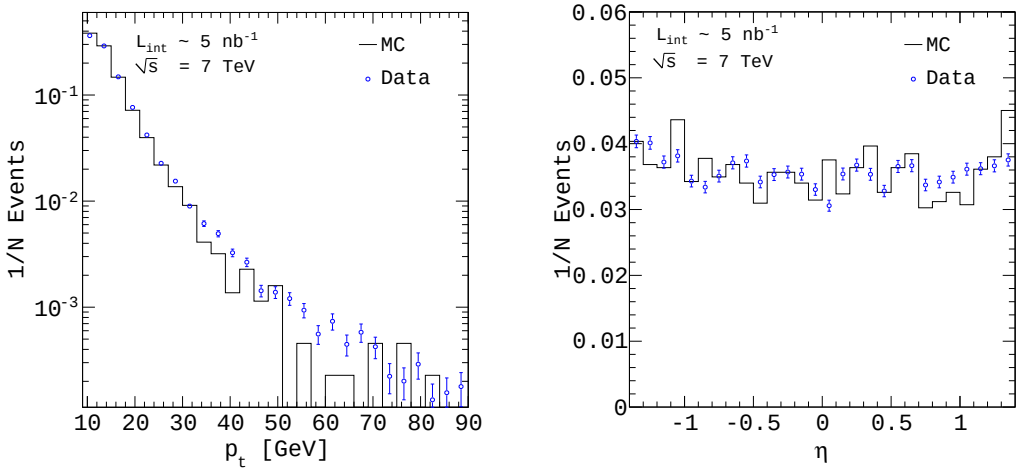

(a) (b)

Figure 3.29: Electron distributions for data (blue circle) and MC (black line); p_t (a) and η in (b).

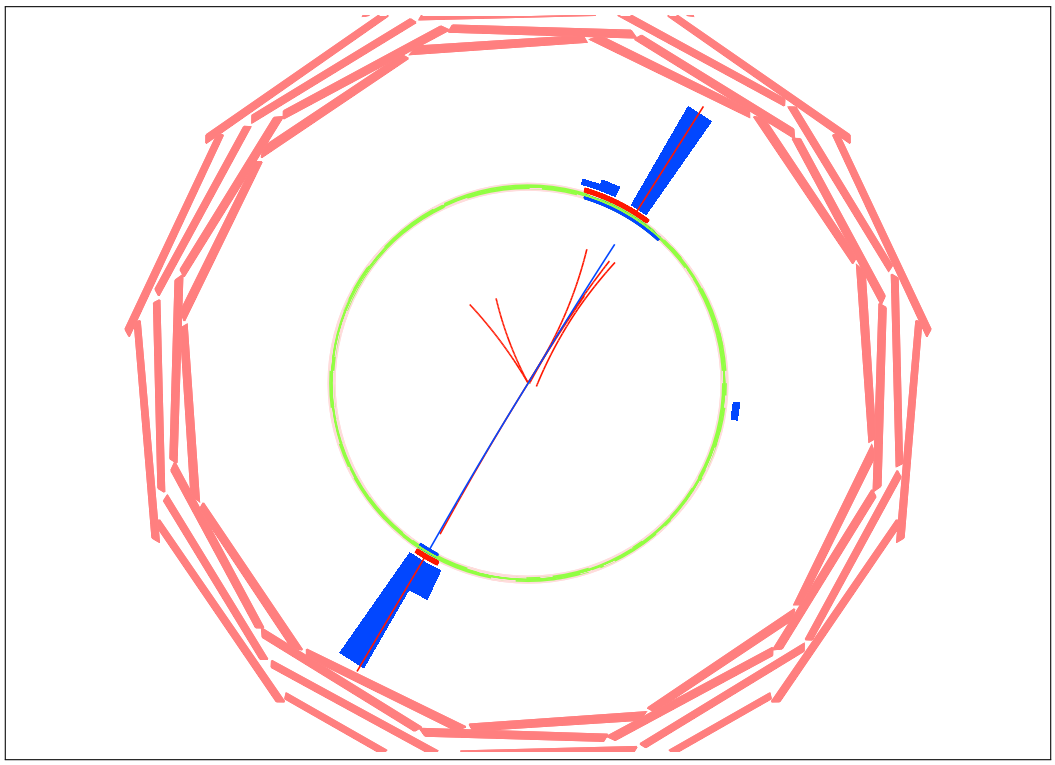

Figure 3.30: Event display of the first reconstructed Z boson candidate within CMS. Event shown in the cross-sectional view of CMS.

Variables	Positron	Electron
p_t [GeV]	34.0	31.9
η	1.80	0.0976
ϕ	59.1°	−122°
Identification:		
$\lvert\Delta\phi_{in}\rvert$	0.0135	0.0125
$\lvert\Delta\eta_{in}\rvert$	0.00163	0.00139
$\sigma_{i\eta i\eta}$	0.0245	0.00870
Isolation:		
$\sum p_t^{\mathrm{Trk}}$ [GeV]	8.97	0
$\sum E_t^{\mathrm{Ecal}}$ [GeV]	0.745	0.663
$\sum E_t^{\mathrm{Hcal}}$ [GeV]	0	0

Table 3.16: Relevant parameters of the electron and the positron for the first Z event. The invariant mass of the Z boson is $m_{ee} = 91.16\,\mathrm{GeV}$ and its transverse momentum $p_t = 2.11\,\mathrm{GeV}$.

barrel and fulfills all selection criteria, i.e. it is reconstructed with the presented selection. The positron instead is reconstructed in the endcap and is not isolated. In principal this event would not be reconstructed from the presented selection. Since the LHC is still running on a low instantaneous luminosity cuts are relaxed, to collect some more interesting events. Once the instantaneous luminosity reaches the design parameters such a procedure is no more possible, since the background would increase enormously.

By adding the 4-momenta of the positron and the electron one gets the 4-momentum of the Z boson. The invariant mass of the Z boson is then $m_{ee} = 91.16\,\text{GeV}$ and the transverse momentum $p_t = 2.11\,\text{GeV}$.

In this chapter the selection of the $Z \to e^+e^-$ events was shown. It was demonstrated, that a simple and robust electron selection can be used to reconstructed the Z boson and reject sufficiently the background. For further physics measurements the efficiency was calculated using a MC method as well as a data driven method. In the next chapter the different measurements using the reconstructed Z boson will be shown, starting from some Z boson distributions, followed by the measurement of the integrated luminosity and the cross-section.

Chapter 4

Physics Measurements

The greatest obstacle to discovery is not ignorance
it is the illusion of knowledge!
- Daniel J. Boorstin [70]

In this last chapter a few measurements using the reconstructed Z boson, with an integrated luminosity $\mathcal{L}_{\text{int}} = 10\,\text{pb}^{-1}$ of pseudo data at 10 TeV, will be presented. These measurements with the Z boson observables can eventually be performed directly with real LHC pp collision data at 7 TeV CM energy.

Accurate measurements of these observables can be considered as a crucial preparation for the many new physics research areas and for detailed studies of SM processes envisaged for the coming years, using data with an integrated luminosity above $1\,\text{fb}^{-1}$ at 7 TeV and at 14 TeV CM energy. In contrast to other known processes, like $pp \to W \to e\nu$, the decay products of the Z boson can be reconstructed very precisely. In addition, to minimize systematic uncertainties on the W measurement, one uses the ratio of the W spectrum with the Z spectrum.

By simply counting the number of Z candidates, one can either calculate the cross-section by using the experimental value of the integrated luminosity or use the theoretical value of the cross-section to calculate the integrated luminosity. The cross-section measurement will be a first experimental test of the SM and, as such, will tell us if the theoretical extrapolations to LHC energies are valid. The luminosity is a crucial parameter for high energy physics experiments, as elaborated on in section 2.1.1.

Some Z boson observables will firstly be shown, such as the Z boson mass, the spectrum and the rapidity. Secondly, the results of the counting measurement will be presented, namely the cross-section and the luminosity measurement. Thirdly, the Z transverse momentum and the Z rapidity measurement will be shown for an integrated luminosity of $10\,\text{pb}^{-1}$ at 10 TeV [1].

[1] Corresponding to $\mathcal{L}_{\text{int}} = 25\,\text{pb}^{-1}$ at 7 TeV, which is the maximum energy used in the LHC for 2010 and 2011. Unfortunately the decision to run at 7 TeV was made only in early 2010, and thus occurred too late to adapt my analysis to the new conditions. However, there is negligible differences in term of kinematics for the

4.1 Z Boson Distributions - Use of Direct Observables

In this section the Z boson observables are shown. These observables are the invariant mass, the p_t and the rapidity. We start with the invariant mass of the Z boson, which easily indicates if the overall calibration is right. This is followed by the Z boson spectrum. At the end of this section, the rapidity distribution will be presented.

4.1.1 Invariant Z Boson Mass and Energy Calibration

In this entire section, Z candidates are only considered, if the electrons pass the isolation and identification cuts described in section 3. In addition to that only candidates with a reconstructed dilepton mass within $3\Gamma_Z$ around the Z boson mass, taken as 91.2 GeV, are used.

Starting with the reconstructed and selected electron candidates, defined in section 3.3, the invariant mass of all electron-positron pairs with opposite charge is calculated and shown in Fig. 4.1 for the pseudo-data.

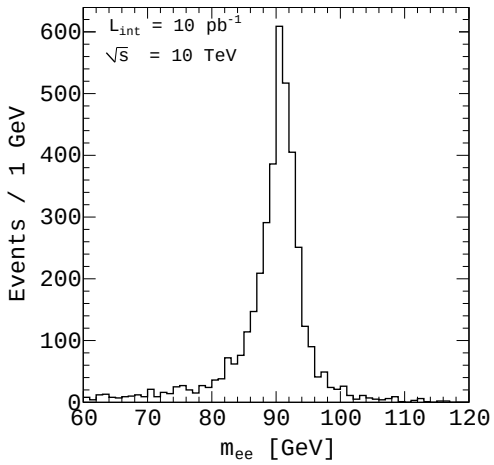

Figure 4.1: Invariant mass distribution for electron-positron pairs with opposite charge and a integrated luminosity of 10 pb^{-1} at 10 TeV.

By first approximation the invariant Z boson mass shows how well the detector is calibrated. The expected Z boson mass is roughly 91 GeV, as shown in Fig. 4.2 for the ideal curve. By introducing an electron mis-measurement, the smearing (scaling) of the new energy (E_{new}) is

$$E_{\mathrm{new}} = 1.01(0.99) \cdot E_{\mathrm{rec}}, \tag{4.1}$$

with E_{rec} the reconstructed energy. The momentum is scaled accordingly and the direction of the electron is thus unchanged. The mean values of the distributions are shifted, as shown in Fig. 4.2 for the red dashed and blue dotted curve. If the overall calibration turns out to be right, but the resolution is worse, then the mass distribution will be wider.

analyzed process.

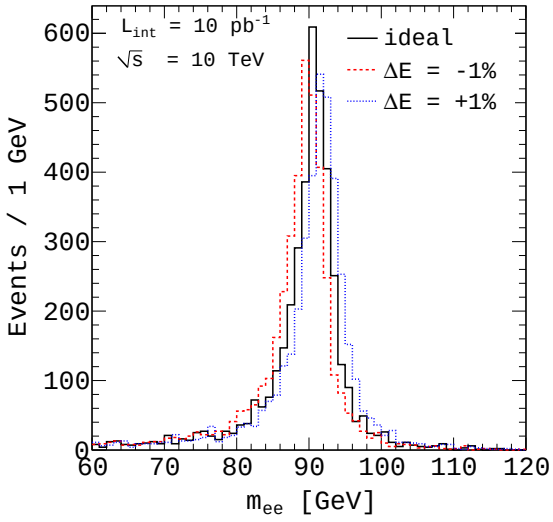

Figure 4.2: Invariant Z boson mass distribution for an ideal detector (black line) and using mis-measured electron energies with $\Delta E/E = \pm 1\%$; with -1% (red dashed line) and $+1\%$ (blue dotted line).

In principle one can use the Z boson invariant mass to calibrate the detector, provided that the reconstructed and the generated mass differ by a few GeV. In Fig. 4.3, the difference between the generated and reconstructed dielectron mass distribution is shown for the MC sample corresponding to $1.4\,\text{fb}^{-1}$ at 10 TeV and shows that the difference is less than 2 GeV. In Tab. 4.1 the mean values for the ideal detector and for the mis-calibrated detector are listed. The shift of the Z mass is, as one would expect, equal to the mis-calibration.

Mis-calibration	Mean m_{ee} [GeV]	%
ideal	90.9	100
-1%	89.7	98.7
$+1\%$	91.9	101.1

Table 4.1: Mean values of the invariant Z mass (m_{ee}) for an ideal detector and for the mis-calibrated detector, using an energy mis-measurement of $\Delta E/E = \pm 1\%$.

We now vary the reconstructed electron energy in just one ECAL supermodule from $\pm 1\%$ to $\pm 10\%$, i.e. the energy and momentum of the electrons within the ECAL supermodule-7 [2] are measured with an error (ΔE). In Fig. 4.4 the mean invariant Z boson mass as a function of the supermodule (SM) is shown for the pseudo data sample. The SM is defined by the direction of the electron. Even in a early stage of the experiment, with an integrated luminosity of $10\,\text{pb}^{-1}$, one is able to identify mis-calibrated supermodules.

[2] Randomly chosen one supermodule.

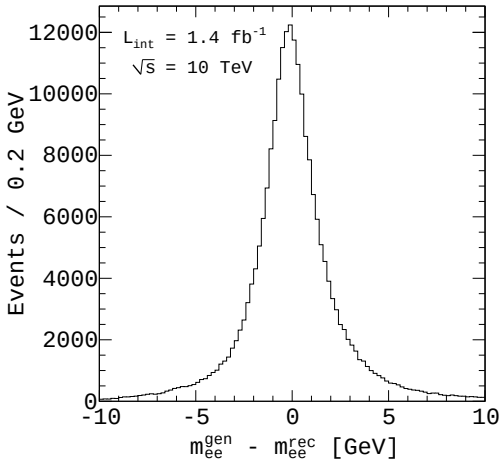

Figure 4.3: Difference between the generated (gen) and reconstructed (rec) dielectron mass distribution for electron-positron pairs.

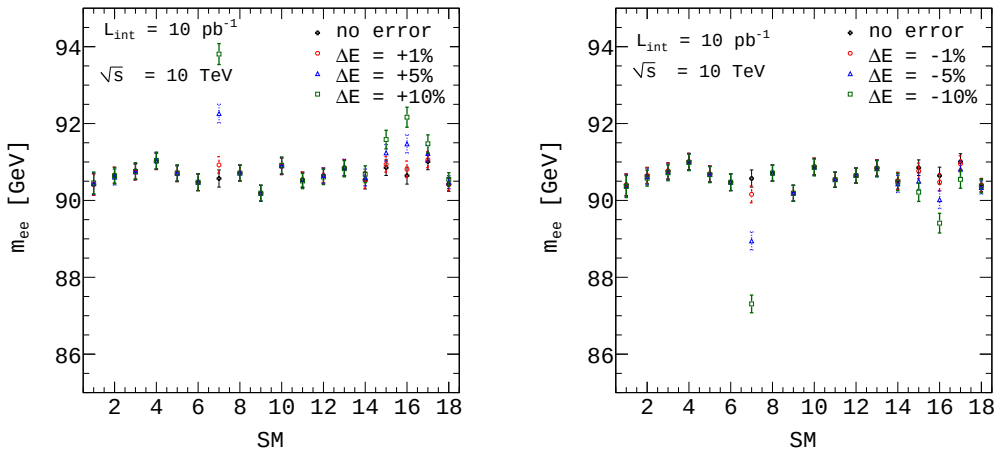

(a) (b)

Figure 4.4: Mean of the Z boson mass for each supermodule with electron energy mismeasurement in ECAL supermodule 7 of $+\Delta E$ in (a), $-\Delta E$ in (b).

More precisely, for a mis-calibration of $\pm 5\%$ and greater, the mass shift for SM-7 is clearly visible. There are some more supermodules that are shifted slightly. This is due to the fact that in most of the cases (low Z p_t) the electron and the positron are almost back-to-back, i.e. $|\phi_e - \phi_p| \sim 180°$, where $\phi_{e/p}$ is the ϕ-position of the electron/positron. The supermodule which is exactly on the opposite side of SM-7 is SM-16.

By a variation of different supermodules with different errors on the energy measurement of $\pm 1\%$, one will not see a shift of the mean value, but a wider mass distribution.

This shows that the Z invariant mass can be used to calibrate or verify the detector calibration with data. Thus, with only $10\,\mathrm{pb}^{-1}$ one should be able to achieve a calibration accuracy of almost 1% and a supermodule to supermodule calibration better than 5%.

We now consider a comparison between pseudo data and MC of the Z boson observables: p_t and rapidity spectrum. Later, in section 4.3, the efficiency corrected measurement and the discussion of these observables will be presented.

4.1.2 p_t Spectrum of the Z Boson

The p_t spectrum of $Z \to e^+e^-$ events can be measured directly and accurately from the four vectors of the reconstruction of both charged electrons. In contrast, the transverse momentum of the W is not directly accessible, due to the escaping neutrino. Thus, one makes use of the transverse momentum balance in $W^\pm \to l^\pm\nu$ events where one jet is present. In particular, the p_t of the jet balances that of the W boson and approximates it. The quality of this approximation can be tested with reconstructed Z events. The test relies on a well reconstructed Z spectrum. Accordingly, we first show the excellent agreement between the reconstructed and the generated Z spectrum.

To verify if the Z boson p_t is well reconstructed and to assess with which precision one can measure it, the difference between the generated and the reconstructed Z p_t is measured and shown in Figs. 4.5(a) for Z $p_t < 30\,\mathrm{GeV}$ and 4.5(b) for Z $p_t > 30\,\mathrm{GeV}$, for $1.4\,\mathrm{fb}^{-1}$ at $10\,\mathrm{TeV}$. By applying a gaussian fit, one finds that $\sigma_{p_t<30\,\mathrm{GeV}} < 400\,\mathrm{MeV}$ and $\sigma_{p_t>30\,\mathrm{GeV}} < 690\,\mathrm{MeV}$. This shows how excellently the Z boson momentum can be reconstructed.

To increase even further the precision of the low p_t measurement, a novel method was presented in [71] and is briefly discussed in Appendix D.

With an integrated luminosity of $10\,\mathrm{pb}^{-1}$ and a CM energy of $10\,\mathrm{TeV}$ the accuracy of the Z boson high p_t spectrum is dominated by statistical error. This is clearly evident in a comparison of the pseudo data with the MC data, shown in Fig. 4.6.

For the pseudo data sample the number of events with $p_t > 100\,\mathrm{GeV}$ is, for some bins, less than 1, which means that all the p_t considerations can be done only for $p_t < 100\,\mathrm{GeV}$. In Tab. 4.2 the number of Z candidates for different Z p_t bins are listed for the pseudo data sample, $\mathcal{L}_{\mathrm{int}} = 10\,\mathrm{pb}^{-1}$, and for the MC sample, $\mathcal{L}_{\mathrm{int}} = 1.4\,\mathrm{fb}^{-1}$.

Probably the best hard-process to study the low p_t QCD radiation, is actually $pp \to Z \to e^+e^-$. In Fig. 4.7 the low Z p_t spectrum for the pseudo data set is compared with the MC sample,

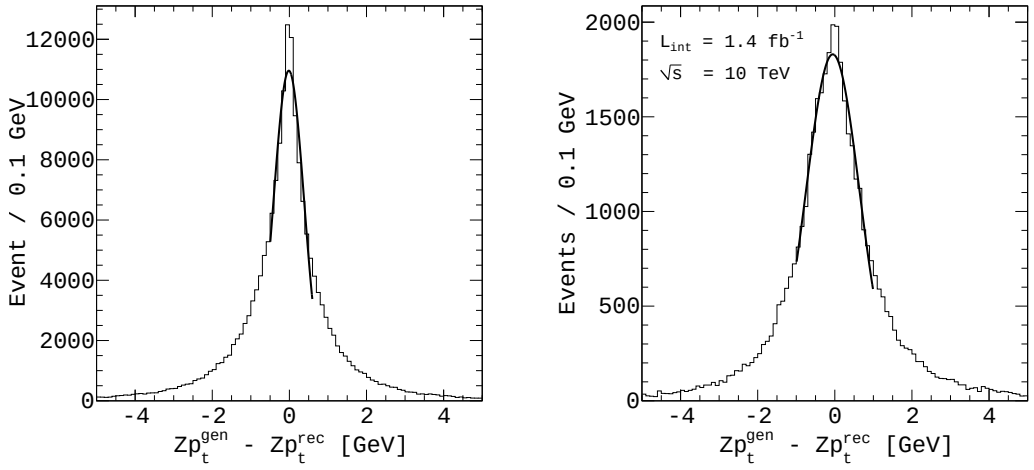

(a) (b)

Figure 4.5: Difference of the Z boson p_t for generated and reconstructed momentum with $10\,\mathrm{pb}^{-1}$ integrated luminosity, for $Zp_t < 30\,\mathrm{GeV}$ (a) and $Zp_t > 30\,\mathrm{GeV}$ (b).

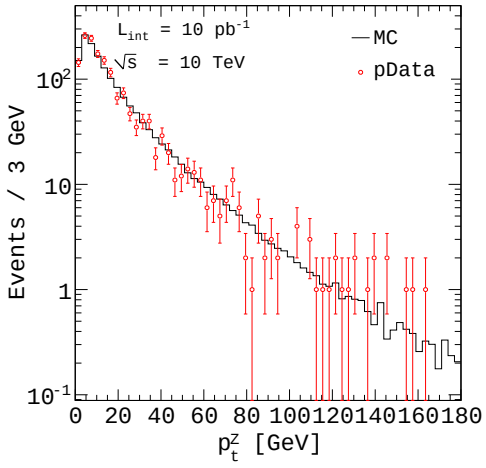

Figure 4.6: Z boson spectrum for events passing the whole selection; pseudo data (red circles) and MC (solid black line) are compared.

$\mathcal{L}_{\mathrm{int}}$	$p_t^Z < 30\,\mathrm{GeV}$	$30\,\mathrm{GeV} < p_t^Z < 100\,\mathrm{GeV}$	$p_t^Z > 100\,\mathrm{GeV}$
$10\,\mathrm{pb}^{-1}$	1 312	260	30
$1.4\,\mathrm{fb}^{-1}$	174 039	36 566	4 179

Table 4.2: Number of Z candidates after selection for different Z p_t bins and for an integrated luminosity of $10\,\mathrm{pb}^{-1}$ and $1.4\,\mathrm{fb}^{-1}$.

normalized to $10\,\mathrm{pb}^{-1}$; once with a binning of 300 MeV (left) and for 1 GeV (right).

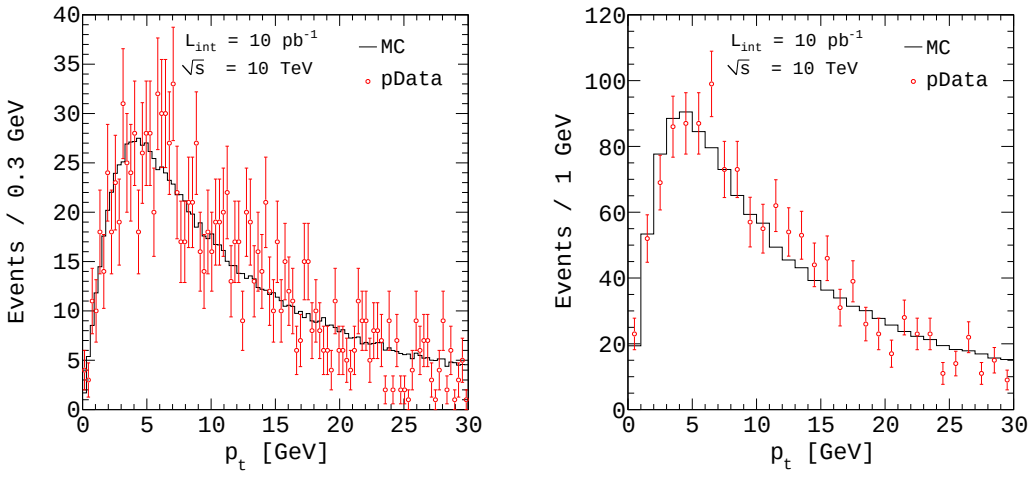

(a) (b)

Figure 4.7: Low Z p_t spectrum for Z candidates passing the whole selection; pseudo data (red circles) and MC (solid black line) are compared. Events per 300 MeV in (a) and per 1 GeV in (b).

One can state, looking at Fig. 4.7, that the statistical significance is already quite good with $10\,\mathrm{pb}^{-1}$ and a CM energy of 10 TeV. One has to emphasize here again, that this is practically the only process to achieve an accurate measurement of low p_t QCD radiations.

4.1.3 Rapidity Spectrum of the Z Boson

As discussed later the Z boson rapidity (Y) is an important quantity, which allows us to look directly at the structure of the protons. That is why a good understanding of the rapidity is mandatory. Already with $10\,\mathrm{pb}^{-1}$ at 10 TeV the shape of the rapidity distribution done with the pseudo data sample agrees well with the MC data sample, as shown in Fig. 4.8. Note the statistical significance is already quite good. A detailed discussion on this observable will be presented in section 4.3.

4.2 Cross-Section or Integrated Luminosity

In this section, the results of the counting experiment will be presented. It is important to note that by counting the number of Z candidates within a given data taking period, one can either calculate the cross-section by using the experimental value of the integrated luminosity or use the theoretical value of the cross-section to calculate the integrated luminosity.

The number of Z candidates decaying into electrons (N_Z) is

$$N_Z = \mathcal{L}_{\mathrm{int}} \cdot \sigma \tag{4.2}$$

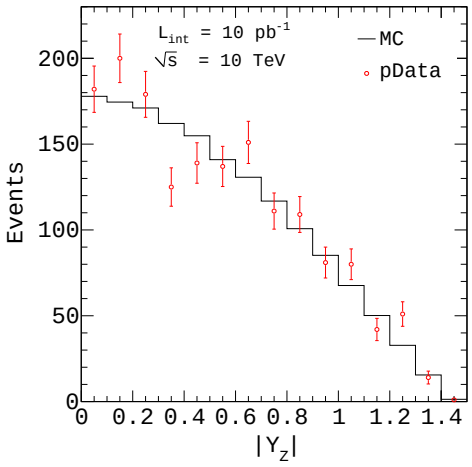

Figure 4.8: Z boson rapidity distribution for Z candidates passing the whole selection; pseudo data (red circles) and MC (solid black line) are compared.

where $\mathcal{L}_{\text{int}}$ is the integrated luminosity and σ is the production cross-section. The number of Z candidates is restricted to the

- detector acceptance, i.e. electron/positron within the barrel, and
- well defined invariant mass peak, i.e. $|m_{ee} - 91.2\,\text{GeV}| < 7.5\,\text{GeV}$.

By counting these candidates one gets the value N_Z with an accuracy of about 3%, considering only the statistical error ($\sqrt{N_Z}$). The systematic uncertainty will be discussed later in this section.

To calculate one of the other quantities, one needs either the integrated luminosity $\mathcal{L}_{\text{int}}$ or the cross-section σ. By knowing one of these values, one can calculate the other. In a early phase of the experiment the integrated luminosity has an uncertainty much larger than the counting accuracy. It has been estimated to $\pm 11\%$ referring to [72].

Different from the luminosity, the cross-section comes from theoretical calculations. The production of Z bosons decaying into electrons, is a theoretically well understood reaction at the LHC. The cross-section has been calculated already to NNLO accuracy [73]. Uncertainties in the calculation come from the imperfect knowledge of the PDFs, from α_s and from the QCD scale. It has been estimated that the total Z cross-section can be predicted with an accuracy of about 5% [74].

The theoretical uncertainties come from different PDF assumptions, different strong coupling constant (α_s) values and MC approximations. This is discussed in the following.

Uncertainty on the Parton Distribution Functions

Firstly, two groups of PDF sets have been considered:

- the CTEQ [75]

- the MRST/MSTW group [76].

One of the main inputs for generating pp events are the PDF sets. These have been varied using the MC generator Pythia6.4. These sets use LO fits and LO α_s, except for CTEQ6l, which is a LO PDF fit with a NLO α_s. In Tab. 4.3 the PDF sets used with the value for the strong coupling constant (α_s) and the Z boson cross-section (σ_Z) are listed. In addition, the ratios between CTEQ5l and the other CTEQ PDF sets and MRST2001lo with MSTW2008lo is computed; for α_s and σ_Z.

PDF Set	Description	α_s	Ratio (α_s)	σ_Z [pb]	Ratio (σ_Z)
CTEQ5l	LO fit	0.127	100.0%	1082	100%
CTEQ6l	LO fit / NLO α_s	0.118	93%	1024	95%
CTEQ6ll	LO fit / LO α_s	0.130	102%	1090	101%
MRST2001lo	LO fit	0.130	100%	1066	100%
MSTW2008lo	LO fit	0.139	107%	1131	106%

Table 4.3: Comparison for the strong coupling constant (α_s) and the cross-section (σ_Z) for different PDF sets. Ratio refers to CTEQ5l and MRST2001lo values. For more information on the PDF sets refer [77].

There is an obvious correlation between the coupling constant and the cross-section. A higher α_s implies a higher probability for initial state radiation. Since the cross-section as a function of the CM energy is a steeply falling function, as shown in Fig. 1.10, the $q\bar{q}$ pair with lower energies (due to the radiation) have a higher probability to produce a dilepton state.

The variation of the cross-section for these LO PDF sets is around $\pm 5\%$. These investigations have been done with LO PDF's, as the entire MC chain is also based on LO calculations. We expect that the differences between the PDF's will become smaller when consistent higher order simulations can be done in the future.

Uncertainty on the Monte Carlo Generators

The Monte Carlo generator used in the whole analysis was Pythia6.4, but of course it is by far not the only generator available. Now, we compare some MC generators. Four multi-purpose event generators were selected:

- Pythia 6.4 (default) and 8.1 [78],

- Sherpa 1.2.1 [79] and

- Herwig++ 2.0 [80].

The fifth generator used was a matrix element generator, namely MadGraph [81]. For the hadronization Pythia6.4 was used. For more details on the different generators, refer to the associated references.

For all generators the same PDF set, namely CTEQ5l, was used. Accordingly the strong coupling constant α_s is the same, as listed already in Tab. 4.3. Now the cross-sections σ_Z for the process $pp \to Z \to e^+e^-$, where the Z boson mass considered lies within $|m_Z - 91.2\,\text{GeV}| < 7.5\,\text{GeV}$, are compared for the different generators. These values are listed in Tab. 4.4 and the ratios of the results from the different generators to that from Pythia6.4 are also provided.

Generator	σ_Z [pb]	Ratio
Pythia6.4	1 081	100%
Pythia8.1	1 096	101%
Sherpa	1 170	108%
Herwig++	1 110	103%
MadGraph	1 132	105%

Table 4.4: Z boson cross-section (σ_Z) for different MC generators, including ratio with Pythia6.4.

Between Pythia6.4, 8.1, Herwig++ and MadGraph the differences are within the theoretical uncertainty of 5% estimated previously. For Sherpa, the difference is slightly larger. We expect that the difference between the MC generators will become smaller when higher order simulations can be done in the future.

Varying MC generators and PDF sets has shown that for the process $pp \to Z \to e^+e^-$, the differences in LO are small and the theoretical uncertainty of 5% is reasonable.

Next the necessary detector quantities to get either the cross-section or the integrated luminosity are described and calculated.

4.2.1 Detector Quantities

The relation in Eq. (4.2) is for an ideal, i.e. perfect detector, which is able to cover the full acceptance and to detect every particle. Of course in reality this is not true, as such a detector does not exist. This leads to the consequence that the number of Z candidates has to be corrected by two detector related quantities:

- the detector efficiency ϵ_Z and
- the detector acceptance $\mathcal{A}_Z$.

The efficiency tells us how many produced Z candidates, within the detectable range, are *found* and the acceptance takes into account that the detector does not cover the full range.

The efficiency can be measured with data, in this case pseudo data. Here the tag and probe results from section 3.5.2 are used. This implies that the uncertainty on the efficiency is related to the number of considered Z candidates. The uncertainty will be of the order of a few percent. In contrast the acceptance is based on MC and thus the error is much smaller. The uncertainty will be a few permille.

Detector Efficiency for Z Candidates

The event efficiency for detecting a Z boson is basically the square of the electron efficiency. By comparing efficiencies from four different selection steps, we are able to better understand the source of discrepancies between the data and MC. Three of the steps are combined, the so-called offline efficiency [3], i.e.

$$\epsilon_{\text{offline}} = \epsilon_{\text{reco}} \times \epsilon_{\text{iso}} \times \epsilon_{\text{eid}} = 0.932, \tag{4.3}$$

where the three indices stand for electron reconstruction, isolation and identification. The fourth is the so-called online efficiency, i.e.

$$\epsilon_{\text{online}} = 1 - (1 - \epsilon_{\text{hlt}})^2 = 0.999. \tag{4.4}$$

The ϵ_{online} is the event efficiency to pass the single electron trigger (ϵ_{hlt}). This trigger can be fired by one or both electrons, so the trigger efficiency is practically one minus the probability for both electrons to fail the single electron trigger. The values are taken from section 3.5.2.

With these definitions, the Z candidate efficiency is

$$\epsilon_Z = \epsilon^2_{\text{offline}} \times \epsilon_{\text{online}}. \tag{4.5}$$

This value can be calculated with the tag and probe method described in section 3.5.2 using real data. Here, we used the pseudo data to calculate the efficiency. One obtains

$$\epsilon_Z = 0.868 \pm 0.027. \tag{4.6}$$

This value means that in almost 87% of the cases, a produced Z candidate, with two electrons decaying in the barrel, is reconstructed. This high efficiency is mainly due to the fact that in hadron colliders, high energetic isolated leptons are very rare and hence easy to detect. The error of 3% is purely statistical and corresponds to the counting uncertainty.

Detector Acceptance for Z Candidates

In contrast to the efficiency, the acceptance is purely computed with simulated data, due to the fact that the acceptance is just a geometrical quantity. The acceptance $\mathcal{A}_Z$ is defined as the ratio of all accepted Z candidates (N^{acc}_{ee}) with all generated Z candidates (N^{acc}_{ee}). The number of all accepted Z candidates fulfils the following electron constraints

- both electrons within the barrel ($|\eta^{sc}| < 1.44$),

[3] The values are taken from the tag and probe efficiency, calculated in section 3.5.2.

- both electrons with the transverse energy of $E_t^{sc} > 20\,\text{GeV}$

and the invariant Z boson mass lies within

- $|m_{ee} - 91.2\,\text{GeV}| < 7.5\,\text{GeV}$.

Thus the acceptance is

$$\mathcal{A}_Z = \frac{N_{ee}^{\text{acc}}}{N_{ee}^{\text{tot}}}, \tag{4.7}$$

Using the huge MC sample, one obtains

$$\mathcal{A}_Z = 0.0956 \pm 0.0002. \tag{4.8}$$

Note the error on the efficiency and on the acceptance are purely statistical. Systematic uncertainties on these quantities can be neglected compared to the huge uncertainty on the integrated luminosity. But of course the main goal should be to get the number of Z candidates as precise as possible. This implies also that the error on the correction factors ϵ_Z and $\mathcal{A}_Z$ have to be as small as possible. By using very robust and simple electron identification cuts we achieved to get a small systematic uncertainty on the efficiency. The systematic uncertainty on the acceptance can be measured by varying PDF sets and Monte Carlo generators. In [82] they observed a variation smaller than 2%.

4.2.2 Integrated Luminosity

To calculate the integrated luminosity in the experiment one has to count the number of Z candidates (N_Z^{obs}) and subtract the background (N_Z^{bkg}). This difference has to be corrected by the efficiency (ϵ_Z) and the acceptance ($\mathcal{A}_Z$) and then one obtains

$$\mathcal{L}_{\text{int}} = \frac{N_Z^{\text{obs}} - N_Z^{\text{bkg}}}{\mathcal{A}_Z \cdot \epsilon_Z \cdot \sigma_{\text{theo.}}}. \tag{4.9}$$

In section 3.4.3 the values for N_Z^{obs} and N_Z^{bkg} were shown. They are

- $N_Z^{\text{obs}} = 1602 \pm 40(\text{stat.})$ and
- $N_Z^{\text{bkg}} = 1.5 \pm 1.2(\text{stat.})$.

The error on the experimental values are the statistical error on the number of observed Z candidates, which is 2.5% and the error on the efficiency, which is about 3%. With the efficiency ($\epsilon_Z = 0.868$) and the acceptance ($\mathcal{A}_Z = 0.0956$), and with the MC cross-section of $\sigma_{\text{theory}} = 1\,944\,\text{pb}$, one obtains for the integrated luminosity

$$\mathcal{L}_{\text{int}} = 9.92 \pm 0.40\,(\text{stat.}) \pm 0.50\,(\text{theo.})\,\text{pb}^{-1}, \tag{4.10}$$

where the error on the cross-section is ±5%, which is based on the previously discussed theoretical uncertainty. Obviously if we would analyze real data, one would use the NLO cross-section calculation. Here we are comparing this result with the MC predictions.

The error on the luminosity appears to be ±6.5%, with a statistical error of 4% and a theoretical error of 5%. This can be compared to the uncertainty in the integrated luminosity achieved in the actual experiment, which has been estimated to be ±11% [72].

4.2.3 $Z \to e^+e^-$ Cross-Section

For the calculation of the measured cross-section (σ_{meas}) the same procedure is used, as for the integrated luminosity. The $Z \to e^+e^-$ cross-section is calculated with

$$\sigma_{\text{meas}} = \frac{N_Z^{\text{obs}} - N_Z^{\text{bkg}}}{\mathcal{A}_Z \cdot \epsilon_Z \cdot \mathcal{L}_{\text{int}}}. \tag{4.11}$$

Of course, we use the same values as in the previous section, except for the integrated luminosity, which is $\mathcal{L}_{\text{int}} = 10\,\text{pb}^{-1}$. With these values, the cross-section is

$$\sigma_{\text{meas}} = 1\,928 \pm 78\,\text{pb (stat.)}, \tag{4.12}$$

where the error is statistical, without any systematics, and are about 4%. The biggest contribution to the systematic uncertainty arises from the measurement of the integrated luminosity, which has been estimated to be ±11% [72]. By adding this uncertainty the cross-section is

$$\sigma_{\text{meas}} = 1\,928 \pm 78\,\text{(stat.)} \pm 193\,\text{(syst.)}\,\text{pb}. \tag{4.13}$$

This shows that the error on the cross-section measurement, $\Delta\sigma_{\text{meas}} \sim 11\%$, is, already in an early stage of the experiment, dominated by the systematic uncertainty of the luminosity.

In Tab. 4.5 the different error contributions are listed; namely the

- statistical error on the Z counting (ΔN_Z),
- theoretical uncertainty on the cross-section ($\Delta\sigma_{\text{theo}}$) and
- systematic uncertainty on the integrated luminosity ($\Delta\mathcal{L}_{\text{int}}$).

Errors	ΔN_Z	$\Delta\sigma_{\text{theo}}$	$\Delta\mathcal{L}_{\text{int}}$
Values	3%	5%	11%

Table 4.5: Statistical and systematic errors for the relevant quantities, number of Z candidates ΔN_Z, cross-section $\Delta\sigma_{\text{theo}}$ and integrated luminosity $\Delta\mathcal{L}_{\text{int}}$.

Additional uncertainties estimated in the actual experiment have been published recently in [82].

The error on the Z counting depends strongly on the amount of data and will be small as soon as one has collected millions of Z candidates. The theoretical uncertainty on the cross-section will not change dramatically in the near future. The error on the integrated luminosity can be minimized by using, for example, the Z counting. It is important to stress again that in a early stage of the experiment, with an uncertainty on the integrated luminosity of about ±11%, the calculation of the cross-section is not the first priority. Instead one should use the counting experiment to calculate the luminosity.

To avoid the huge uncertainty on the luminosity, an alternative calculation could be the ratio of the W production cross-section with the Z cross-section. This would have one big advantage with respect to the single cross-section measurements, namely many systematic errors would cancel out. Especially the huge uncertainty on the luminosity could be neglected.

To avoid even more systematic uncertainties, like the one on the efficiency, one has to apply the same electron selection for W bosons (*hard*) and for Z bosons (*soft*). This has been studied in [62]. As the W decays only in one electron, in principle one could apply the *hard* selection only on one electron and the *soft* on the other. This would increase the efficiency for a few percent. However having a huge efficiency is not a goal and has no real advantage, except the number of selected events is very small, which is not the case for W and Z events.

4.3 Measuring the Z Transverse Momentum and Rapidity Spectra

In this section the measurement of the differential cross-sections $\mathrm{d}\sigma/\,\mathrm{d}p_t$ and $\mathrm{d}\sigma/\,\mathrm{d}Y$ will be shown. Both using an integrated luminosity of $10\,\mathrm{pb}^{-1}$ at $10\,\mathrm{TeV}$.

As shown in the previous section, the measured observables have to be corrected by the acceptance and the efficiency, i.e.

$$\frac{\mathrm{d}\sigma}{\mathrm{d}p_t}(i) = \frac{N_Z^{\mathrm{obs}}(i) - N_Z^{\mathrm{bkg}}(i)}{\mathcal{A}_Z(i) \cdot \epsilon_Z(i) \cdot \mathcal{L}_{\mathrm{int}}} \quad \text{and} \quad \frac{\mathrm{d}\sigma}{\mathrm{d}Y}(i) = \frac{N_Z^{\mathrm{obs}}(i) - N_Z^{\mathrm{bkg}}(i)}{\mathcal{A}_Z(i) \cdot \epsilon_Z(i) \cdot \mathcal{L}_{\mathrm{int}}}, \tag{4.14}$$

where i stands for the value in bin i. Using the same definition for the acceptance as derived in section 4.2.1, the acceptance as a function of the Z p_t and the rapidity (Y) are shown in Fig. 4.9(a) and Fig. 4.9(b) respectively, with the MC sample of $1.4\,\mathrm{fb}^{-1}$.

In these two plots one sees nicely the kinematic of the process reproduced. For low Z p_t the electrons are expected in the forward region, but these electrons are not selected. That is why the acceptance decreases for low transverse momenta. The opposite happens for high Z p_t where the electrons are expected in the central region, thus the acceptance increases.
For rapidity values around zero, the electron and the positron are both in the selected region (barrel). For high Z p_t the electrons get boosted, and so they are no longer back-to-back. For these events and for rapidity values near 1.4, one particle is selected and the other not. An illustration of this fact is shown in Fig. 4.10. This has the consequence that the acceptance for the rapidity decreases.

The efficiency is defined as reconstructed Z candidates over the generated candidates. The reconstructed candidates are all events, where the electron/positron pairs fulfils all selection criteria, i.e. preselection, isolation and identification and, the Z boson mass lies within $|m_{ee} - 91.2\,\mathrm{GeV}| < 7.5\,\mathrm{GeV}$. These candidates are compared with the generated Z candidates with the same mass constraint and where the electron/positron pairs are within the barrel and have a transverse energy of $E_t > 20\,\mathrm{GeV}$. The efficiency as a function of the Z p_t and the rapidity (Y) are shown in Fig. 4.11(a) and Fig. 4.11(b) respectively, with the MC sample of $1.4\,\mathrm{fb}^{-1}$ at $10\,\mathrm{TeV}$.

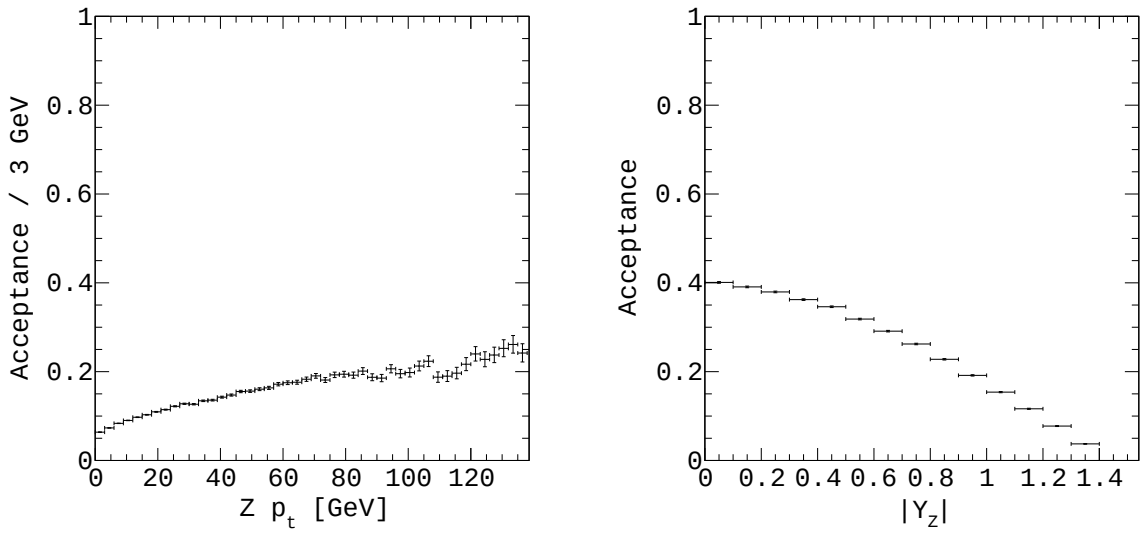

(a) (b)

Figure 4.9: Acceptance as a function of the transverse momentum of the Z boson (Z p_t) in (a) and as a function of the rapidity (Y_Z) in (b), determined from the MC sample of 1.4 fb^{-1}.

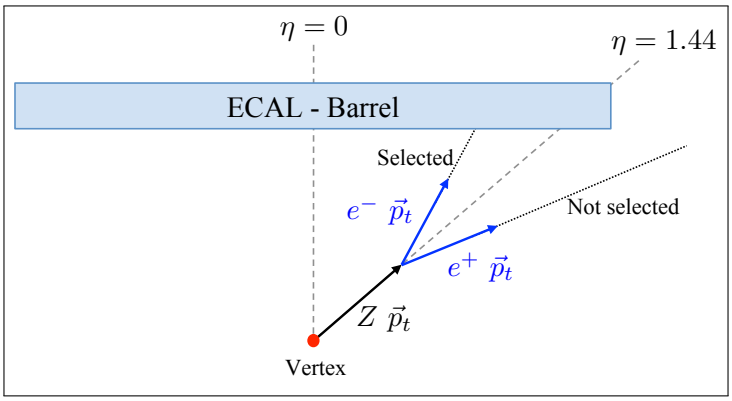

Figure 4.10: Illustration of the acceptance for high Z p_t electrons around the edge of the barrel.

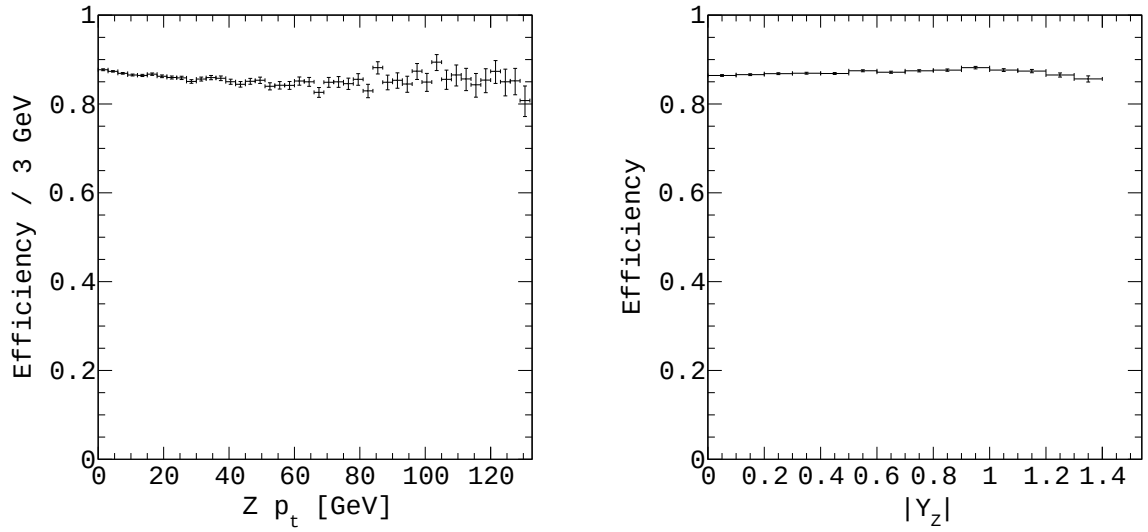

(a) (b)

Figure 4.11: Efficiency as a function of the transverse momentum of the Z boson (Z p_t) in (a) and as a function of the rapidity (Y_Z) in (b), determined from the MC sample of $1.4\,\mathrm{fb}^{-1}$.

4.3.1 Measuring the Z Transverse Momentum Spectrum

We can now present the differential cross-section as a function of the Z boson transverse momentum in Fig. 4.12(a) for the entire spectrum and in Fig. 4.12(b) for the low p_t. The differential cross-section ($\mathrm{d}\sigma/\,\mathrm{d}p_t$) is measured with the pseudo data, corresponding to $10\,\mathrm{pb}^{-1}$ at 10 TeV and compared with the truth differential cross-section of the generated information using the normalized MC sample, corresponding to $1.4\,\mathrm{fb}^{-1}$ at 10 TeV.

This measurement can be used to tune the simulation and to control the theoretical prediction. In addition, the low p_t distribution is the best way to measure low Q^2 QCD effects, which is crucial for the understanding of low p_t jets.

We showed that the transverse momentum of Z bosons can be measured with great precision. In contrast, for W bosons the measurement of the transverse momentum requires the use of the missing transverse momentum and thus the hadron and jet activity in the selected events. Consequently, and especially at transverse momenta smaller than 30 GeV, the precision of the W p_t spectrum will, at best, be very limited. However, at higher transverse momenta of the W boson, its p_t spectrum can be approximated with acceptable accuracy, using the reconstructed jet transverse momentum. In combination with the corresponding measurement of the Z p_t spectrum, this approach can eventually be used to constrain directly the PDFs at high Q^2 and to test the MC models for many electroweak phenomena.

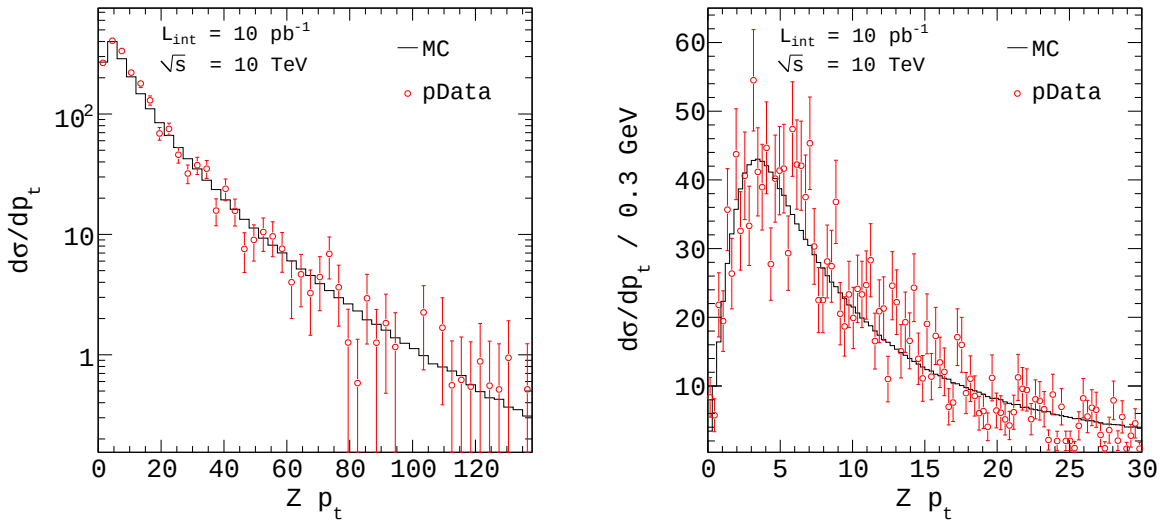

(a) (b)

Figure 4.12: Differential cross-section as a function of the transverse momentum ($\mathrm{d}\sigma/\,\mathrm{d}p_t$) measured with the pseudo data, corresponding to $10\,\mathrm{pb}^{-1}$ at 10 TeV (red circle) and compared with the normalized MC sample, corresponding to $1.4\,\mathrm{fb}^{-1}$ at 10 TeV (black line); for the entire p_t spectrum in (a) and for the low p_t in (b).

4.3.2 Measuring the Z Rapidity Spectrum

We now consider the rapidity. The differential cross-section as a function of the Z boson rapidity is shown in Fig. 4.13. The differential cross-section ($\mathrm{d}\sigma/\,\mathrm{d}Y$) is measured with the pseudo data, corresponding to $10\,\mathrm{pb}^{-1}$ at 10 TeV and compared with the truth differential cross-section of the generated information using the normalized MC sample, corresponding to $1.4\,\mathrm{fb}^{-1}$ at 10 TeV.

This result shows very well that the statistical uncertainty is small enough to compare the measured distribution with the theoretical prediction, in this case the generator information.

As derived in section 1.5.3, the following relation is very useful to tune the MC generators:

$$\frac{\mathrm{d}^2\sigma}{\mathrm{d}p_t\,\mathrm{d}Y} \propto x_1 f_1(x_1, Q^2) x_2 f_2(x_2, Q^2), \tag{4.15}$$

where x_i are the Bjorken scale variables[4] and f_i the proton structure functions. The shape of the distributions is proportional to the structure functions. That is the reason why we divide the Z p_t spectrum into three parts:

(a) $0\,\mathrm{GeV} < p_t^Z \leq 20\,\mathrm{GeV}$,

(b) $20\,\mathrm{GeV} < p_t^Z \leq 50\,\mathrm{GeV}$ and

[4]As we are only considering electrons in the barrel the x_i predictions are very limited. For a complete consideration one has to extend the analysis also in the forward region.

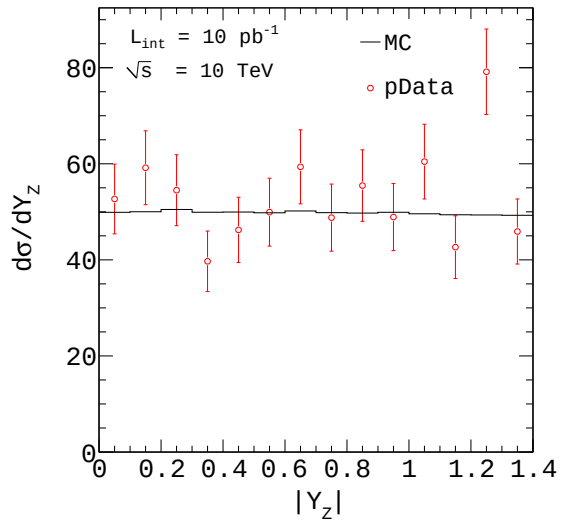

Figure 4.13: Differential cross-section as a function of the rapidity ($\mathrm{d}\sigma/\,\mathrm{d}Y$) measured with the pseudo data, corresponding to $10\,\mathrm{pb}^{-1}$ at 10 TeV (red circle) and compared with the normalized MC sample, corresponding to $1.4\,\mathrm{fb}^{-1}$ at 10 TeV (black line).

(c) $50\,\mathrm{GeV} < p_t^Z \leq 80\,\mathrm{GeV}$.

In Figs. 4.14(a)-4.14(c) these rapidity distributions are shown. The agreement is much better for low Z p_t than for higher Z p_t mostly due to the lack of statistics. This shows that for Z $p_t < 20\,\mathrm{GeV}$ the shape of the distribution can be used to compare data with different PDF sets. The best matching PDF set will be used to compare further theoretical values, i.e. the outcome of MC generators.

It is important to stress that the shape of the boson rapidity distribution is, as just mentioned, strongly dependent on the choice of PDF's. In Fig. 4.15 the ratio of the rapidity distribution for different PDF sets are shown, whereas the default set is CTEQ5l [5].

One sees that the difference for the Z boson rapidity $Y < 3$, where the statistical error is still small, are about 5%. This plot is done only on generator level with a dataset corresponding to an integrated luminosity of $100\,\mathrm{pb}^{-1}$.

This dependence of the rapidity on the PDFs is due to the fact that the shape of the Z boson rapidity (Y) distribution is proportional to the Bjorken scale variable x_i. As derived in section 1.5.3 the relations are

$$m^2 = x_1 x_2 s \quad \text{and} \quad Y = \frac{1}{2} \ln\left(\frac{x_1}{x_2}\right).$$

[5] At CDF in Run I [83] the shape of the rapidity distribution for $Z \to e^+e^-$ was measured. The good agreement observed between the measured shape of Y with that obtained from simulation using CTEQ5l PDF's motivates the selection of this PDF set for our event generation.

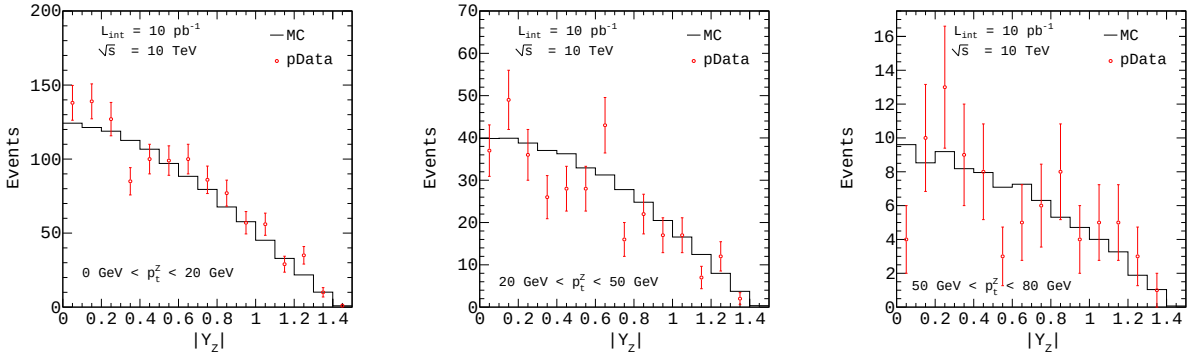

(a) (b) (c)

Figure 4.14: Z boson rapidity distributions for three different p_t^Z cuts; $0\,\text{GeV} < p_t^Z \leq 20\,\text{GeV}$ (a), $20\,\text{GeV} < p_t^Z \leq 50\,\text{GeV}$ (b) and $50\,\text{GeV} < p_t^Z \leq 80\,\text{GeV}$ (c); pseudo data (red circles) and MC (solid black line) are compared.

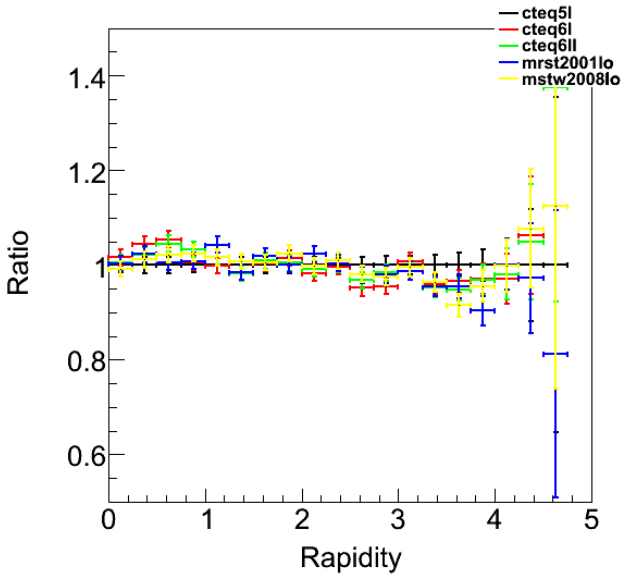

Figure 4.15: Ratio of the Z boson rapidity distribution for different LO PDF sets.

where $s = 4E^2$ with E the CM energy of the collider. Using this two relations one finds

$$x_1 = \frac{m}{\sqrt{s}} e^{Y} \quad \text{and} \quad x_2 = \frac{m}{\sqrt{s}} e^{-Y} \tag{4.16}$$

To date, x_i were measured up to a CM energy of about 2 TeV. With the LHC it will be possible to measure x_i up to a CM energy of about 14 TeV, which means an increase on the kinematic range of almost one order of magnitude. In Fig. 4.16 the kinematic ranges for different colliders are shown, whereas for the LHC the range is based on the design energy and not on the energy of 7 TeV, used now.

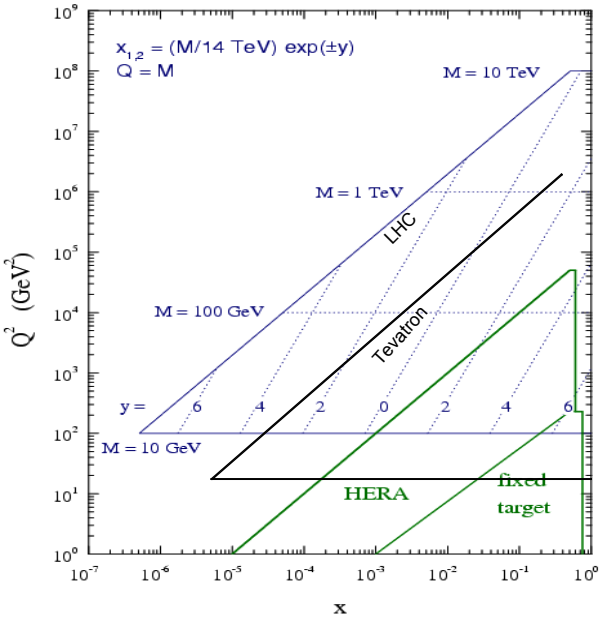

Figure 4.16: Kinematic ranges for different colliders [77].

The Bjorken x_i variable becomes small for large Y_Z. Since the Z boson rapidity is correlated with the pseudorapidity of the electrons which are restricted to the barrel, the x_i do not reach very small values. However, in Fig. 4.17 the variable x_1 is compared to the pseudo data and the MC Z candidates, whereas the pseudo data x_1 is computed via the Z boson rapidity (see Eq. (4.16)) and the MC x_1 is calculated with the generated quarks (q), antiquarks ($\bar{q}$), i.e.

$$x_1 = p_z^q / P, \tag{4.17}$$

with P the proton momentum and p_z^q the quark or anti-quark momentum in the positive z direction.

The agreement between the generated quark and the reconstructed Z boson for the Bjorken x_1 is excellent. With more data and using the entire detector range one will be able to extend the range of x_i from nearly 1 down to 10^{-6}.

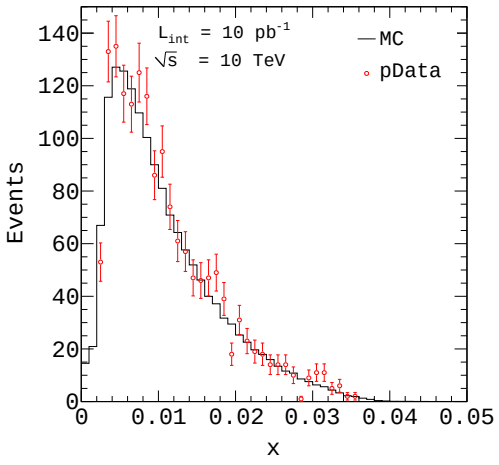

Figure 4.17: Bjorken x_1 distribution using generator information such as initial quark momentum for MC and reconstruction information such as Z boson rapidity for the pseudo data; pseudo data (red circles) and MC (solid black line) are compared.

4.4 Jet Transverse Momentum Measurement

Hadronic jets, which originate from the fragmentation of quarks and gluons into hadrons, can be defined as bundles of charged and neutral particles. Various jet finding algorithms exist, which try to reduce the sensitivity to detector and fragmentation uncertainties for detailed measurements of jet multiplicities and the related QCD parameters. For the purpose of the analysis described in this chapter the so-called SISCone5 [6] jet finding algorithm [84] is used.

Generated jets are reconstructed at the generator level using the energy directly of the associated stable particles. In contrast, the measurement of the jets on the detector level, the so-called reconstructed jets, are based on the associated electromagnetic and hadron calorimeter clusters. It is further required that the reconstructed jet directions are found within the acceptance of the electromagnetic barrel and endcap calorimeters with an $|\eta_{\text{jet}}| < 2.5$.

In order to assess how many jets are simultaneously produced with a Z boson, the so-called jet multiplicity is shown. The jet multiplicity is the number of jets within an event. Here only jets with a $p_t > 30\,\text{GeV}$ are considered. The jet multiplicity is plotted in Fig. 4.18 for the generated and reconstructed jets, for events with an invariant Z boson mass within $3\Gamma_Z$, i.e. $|m_Z - 91.2\,\text{GeV}| < 7.5\,\text{GeV}$.

As we would expect, the zero bin dominates the distribution, which means that $\sim 80\%$ of the events are 0-jet events and $\sim 12\%$ are 1-jet events. The focus is on 0-jet and 1-jet events. In 1-jet events the kinematics are such that the jet momentum is balanced by the Z boson momentum. This means that by measuring the Z spectrum for 1-jet events, one measures directly the 1-jet spectrum. This will be shown later in this section.

[6] SISCone is the seedless infrared-safe cone jet algorithm. It is collinear- and infrared-safe to all orders of pQCD.

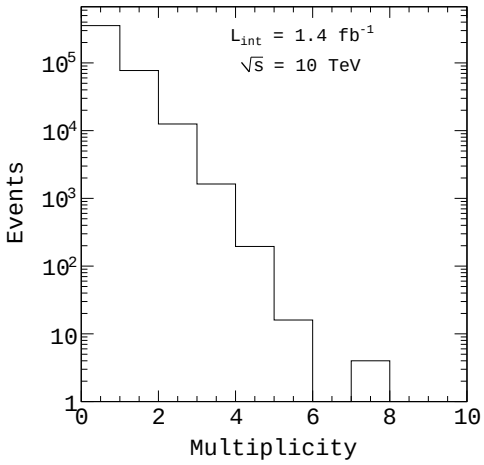

Figure 4.18: Jet multiplicity for events with the reconstructed Z boson mass within $3\Gamma_Z$ for $1.4\,\mathrm{fb}^{-1}$.

For all events with an invariant Z boson mass within $3\Gamma_Z$, the generated jet p_t and the reconstructed jet p_t is shown in Fig. 4.19. One sees that the two distributions are in good agreement, meaning that the jet reconstruction algorithm works fine. What is not measured here is the jet momentum below 30 GeV. This instead can be measured with the help of the Z boson. Being able to measure the jet spectrum is, as already mentioned, crucial for the measurement of the W spectrum, since the W spectrum can only be measured by using the jet measurement. The easiest cases to handle are events, where one jet balances the W p_t. In these events, the jet spectrum shows directly the W p_t. The Z boson spectrum can then be used to test this procedure, due to the fact that the Z p_t can be measured with excellent precision.

The Z p_t distribution for different jet bins, i.e. for the 0-jet, 1-jet and the >1-jet bin, show the dependence between the jet activity and the Z p_t. As the Z boson gets only a momentum if there is a jet, it is obvious that for 0-jet the Z p_t is very small, and for 1-jet, the Z p_t gets bigger. Of course one would expect that the Z p_t is zero for 0-jet events. The reason that the distribution is not zero is that jets are only considered with a $p_t > 30\,\mathrm{GeV}$, which means that all jets below 30 GeV are not considered as jets, while they will still contribute to the Z p_t. The Z boson spectrum for these different bins are shown in Fig. 4.20, for the MC sample of $1.4\,\mathrm{fb}^{-1}$.

The number of Z candidates for the >1-jet bin is dominated by statistics and therefore for an integrated luminosity of $10\,\mathrm{pb}^{-1}$, no prediction can be made. For the 1-jet bin, the results are slightly better and so a comparison with the jet distributions is feasible. In Fig. 4.21 the Z boson p_t for the 1-jet bin is compared with the jet p_t spectrum for events with one jet. The plot in Fig. 4.21 is for $\mathcal{L}_{\mathrm{int}} \approx 1.4\,\mathrm{fb}^{-1}$.

One can see very clearly that for $p_t > 30\,\mathrm{GeV}$ the agreement between the Z spectrum distribution and the jet distribution is excellent. For low jet $p_t < 30$, where there are no reconstructed jets, the best thing to do is to use the Z p_t for low transverse momentum jets.

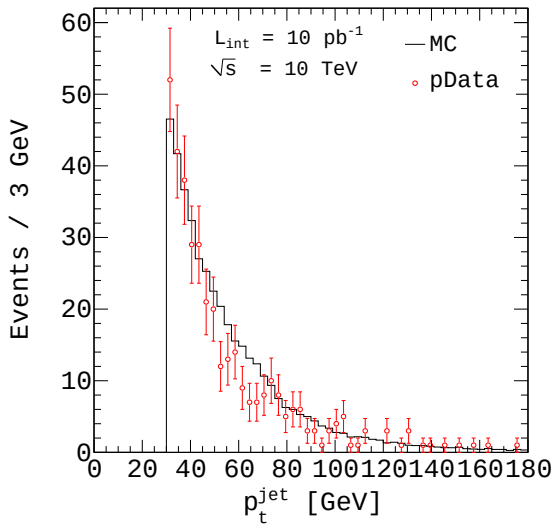

Figure 4.19: Jet p_t for events with a reconstructed Z boson mass within $3\Gamma_Z$; for $1.4\,\mathrm{fb}^{-1}$ (black line) and for $10\,\mathrm{pb}^{-1}$ (red circle).

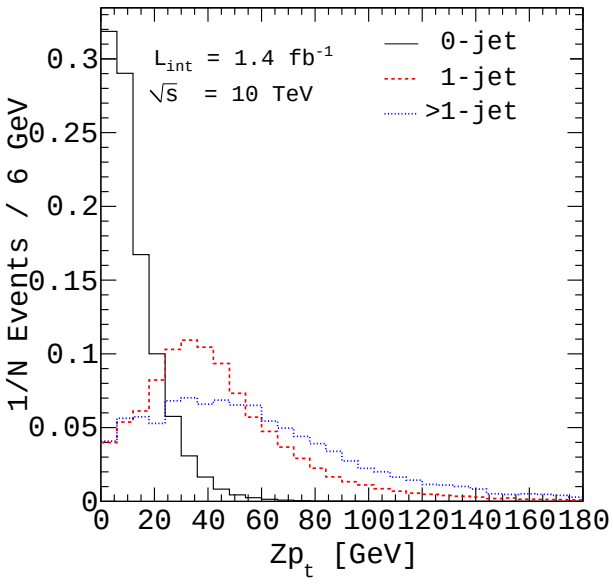

Figure 4.20: Z boson spectrum for the 0-jet (black line), 1-jet (red dashed line) and the >1-jet bin (blue dotted line); the distributions are normalized to one.

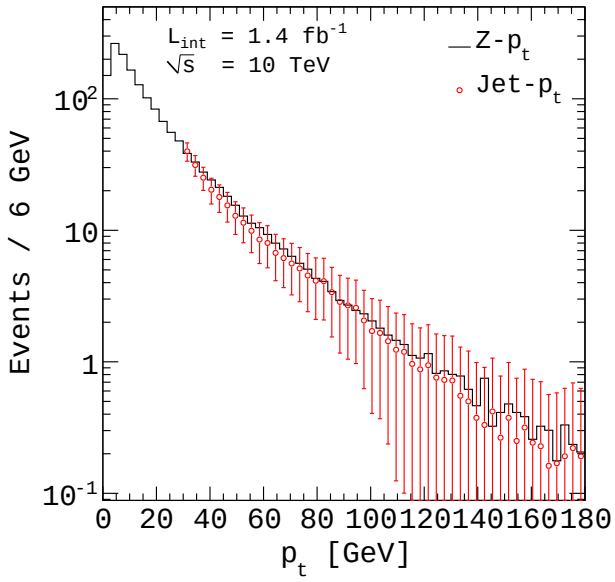

Figure 4.21: Z boson spectrum compared with the jet spectrum for events with only one jet, done for $\mathcal{L}_{\text{int}} \approx 1.4\,\text{fb}^{-1}$.

Using the $W^{\pm} \to e^{\pm}\nu$ events the spectra of the observed jet p_t and the generated W boson p_t are compared in Fig. 4.22 [7]. Again, the generated spectrum was taken from a large statistical sample and the reconstructed jets from a pseudo data sample of $25\,\text{pb}^{-1}$. It is evident that the jet p_t spectrum matches the one of the W boson well above 30 GeV.

To compare the p_t distributions in more detail, Fig. 4.23 shows the ratio of the p_t distributions of jets and W bosons from Fig. 4.22. The binning was chosen such that sufficient statistics in every p_t bin up to 200 GeV is obtained. The single entries of the ratio distributions are denoted as "correction-factors".

It is evident that the transverse momenta of the jets and the W bosons do not match perfectly. The reason is the imperfect measurement of the jet p_t. It is important to mention that the correction-factors presented here were produced using the full statistics of each 2 million $W^{\pm} \to \ell^{\pm}\nu$ sample, corresponding to $\mathcal{L}_{\text{int}} \approx 340\,\text{pb}^{-1}$.

Once data are available, these Monte Carlo corrections-factors can be used to obtain the correct W p_t spectrum from the measured jet p_t spectrum. In particular, the single entries of the measured jet p_t spectrum will be divided by the corresponding Monte Carlo correction-factor.

In this chapter some relevant Z boson distributions were shown, including the transverse momentum and the rapidity distribution, from which the transverse Z boson momentum was then compared with the jet transverse momentum. Two fundamental measurements were shown:

[7] The plots 4.22 and 4.23 are taken from [85]. This note was done with 7 TeV CM energy and a pseudo data sample of $25\,\text{pb}^{-1}$, thus comparable with the rest of the analysis.

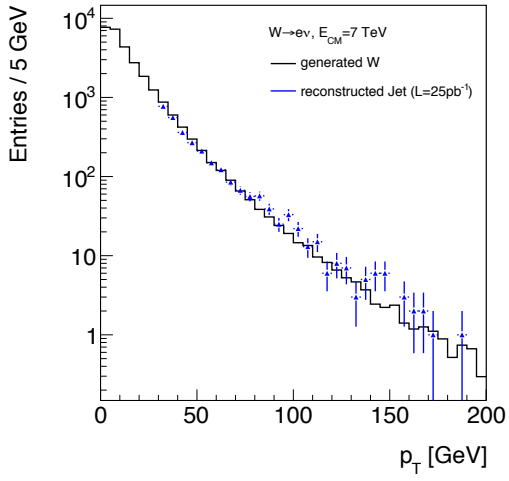

Figure 4.22: The p_t spectra for accepted W signal events in the electron channel for $25\,\mathrm{pb}^{-1}$. The transverse momentum are shown for the generated Ws and the reconstructed jet in the events.

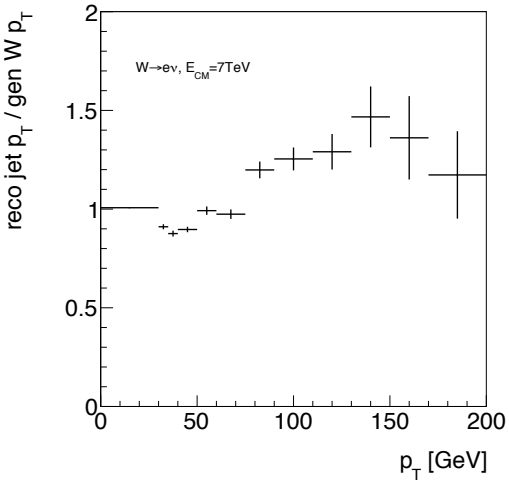

Figure 4.23: The ratio of the reconstructed and generated W transverse momentum spectrum.

the cross-section and the luminosity measurement. The Z boson rapidity distribution was compared with the Bjorken scale variable and shown that the generator level distribution could be reproduced well with the reconstructed Z boson and that the rapidity shows a PDF sensitivity.

Conclusion

The most exciting phrase to hear in science,
the one that heralds new discoveries,
is not "Eureka!" but "That's funny..."
- Isaac Asimov [86]

We have introduced the theoretical concept of the Standard Model of Particle Physics, with a focus on the Electroweak Theory, followed by the description of the LHC and the CMS experiment. Due to the lack of real data, simulated data, so-called Monte Carlo samples, have been used. A subset of this huge data sample was taken, in order to play the role of real data, the so-called pseudo data. One could expect, after the starting phase of the LHC, to have collected and reconstructed a few thousand Z bosons, corresponding to an integrated luminosity of $25\,\mathrm{pb}^{-1}$ at a center-of-mass energy of $7\,\mathrm{TeV}$. Here the analysis was performed using an integrated luminosity of $10\,\mathrm{pb}^{-1}$ at a center-of-mass energy of $10\,\mathrm{TeV}$.

It was shown that a simple and robust electron selection can be used to identify electrons coming from the process $pp \to Z \to e^+e^-$. The electron selection discussed uses only electrons within the barrel of the detector. The reason for the restriction to the barrel is that, in the starting phase the electrons in the barrel will be much simpler to understand, hence better suited to be used in further analysis. The electron selection uses the isolation condition and three additional identification criteria, including on the one hand matching the track of the electron with the position of the corresponding energy cluster, and, on the other hand considering the shower shape of the electron in the ECAL. It has been shown that this selection is very efficient.

By identifying an electron positron pair and reconstructing its four momentum, it was shown that the Z boson can be reconstructed with all its properties. These properties, like transverse momentum, rapidity or invariant mass have been compared with the generated distributions. The ability to reconstruct the Z boson observables with high precision plays a key role in understanding the detector. The Z events will allow a test of MC simulations and to demonstrate that the detector is well calibrated. It was revealed that already a 1% mis-calibration of the ECAL detector can be reproduced and measured with the reconstruction of the Z boson in the electron channel. In addition to that, a sensitivity test was performed and it could be shown that one can identify a mis-calibrated or badly working supermodule by looking at the reconstructed invariant Z boson mass as a function of the supermodule.

The ability to reconstructed the Z boson spectrum with high precision allows us to use it to control the jet transverse momentum measurement. This plays an important role in the measurement of the W boson spectrum. The rapidity of the Z boson is proportional to the momentum fraction of the partons in the proton. This fact was used to show how nicely this can be reproduced. The proton structure functions, which depend strongly at the momentum fraction, are a major source of uncertainty. By looking on the rapidity distributions the comparison with different parton distribution functions was done. Differences of at least 5% can be expected for different leading order functions, which can be used to constrain the best parton distribution function for the simulation of Monte Carlo data.

Finally, the measurements of the Z boson cross-section in the electron channel and the calculation of the integrated luminosity was performed. It was shown that one can expect a statistical error on the counting of the Z candidates of 3%. The uncertainty on the acceptance is rather small (in the permille level) whereas the uncertainty on the efficiency using a data driven method is up to 3% due to statistics. The theoretical uncertainties on the cross-section are 5%. However the biggest uncertainty is in the integrated luminosity, which is estimated to be 11%.

It was demonstrated that in a early phase of the experiment, the counting of Z bosons should be used to constrain the integrated luminosity and not to measure the cross-section. Instead one should extent the reconstruction in the electron channel and use the W boson to compute ratios, which have smaller systematic uncertainties and thus can be compared with theoretical predictions.

We have now collected a few $10\,\mathrm{nb}^{-1}$ of data and by now only a few Z and some more W could be reconstructed. In the longer term with a few fb^{-1}, i.e. 100 000 of Z and a million of W, much more could be done. The sensitivity of the p_t spectrum could be extended to higher p_t, wherein the lower statistical fluctuations allows to constrain the parton distribution functions for low Q^2. Of course, with the profound understanding of the W, the search on the Higgs boson in the $H \to WW$ channel can start.

Appendix A

Pauli and Dirac Matrices

A.1 Pauli Matrices

The Pauli matrices are three hermitian, unitary and traceless 2×2 matrices

$$\sigma^1 = \begin{pmatrix} 0 & 1 \\ 1 & 0 \end{pmatrix}, \sigma^2 = \begin{pmatrix} 0 & -i \\ i & 0 \end{pmatrix} \text{ and } \sigma^3 = \begin{pmatrix} 1 & 0 \\ 0 & -1 \end{pmatrix}. \tag{A.1}$$

Product rules

$$\sigma^i \sigma^j = \delta^{ij} \mathbb{1} + i\epsilon^{ijk}\sigma_k \tag{A.2}$$

Thus, in particular,

$$\begin{aligned} (\sigma^i)^2 &= \mathbb{1} \quad \forall i \in \{1,2,3\}, & \text{(A.3)} \\ \left[\sigma^i, \sigma^j\right] &= 2i\epsilon^{ijk}\sigma_k, & \text{(A.4)} \\ \{\sigma^i, \sigma^j\} &= 2\delta^{ij}\mathbb{1}, & \text{(A.5)} \end{aligned}$$

and for any two vectors $\vec{a}$ and $\vec{b}$,

$$(\vec{a}\cdot\vec{\sigma})(\vec{b}\cdot\vec{\sigma}) = \vec{a}\cdot\vec{b} + i\vec{\sigma}\cdot(\vec{a}\times\vec{b}). \tag{A.6}$$

Exponential

$$e^{i\vec{a}\cdot\vec{\sigma}} = \cos a + i\hat{a}\cdot\vec{\sigma}\sin a, \tag{A.7}$$

where $\vec{a} = a\hat{a}$.

A.2 Dirac Matrices

The Dirac matrices are four unitary traceless 4×4 matrices

$$\gamma^0 = \begin{pmatrix} \mathbb{1} & 0 \\ 0 & -\mathbb{1} \end{pmatrix} \text{ and } \gamma^i = \begin{pmatrix} 0 & \sigma^i \\ -\sigma^i & 0 \end{pmatrix} \tag{A.8}$$

with σ^i the Pauli matrices. It is convenient to define a 5^{th} matrix γ^5 as [1]

$$\gamma^5 \equiv i\gamma^0\gamma^1\gamma^2\gamma^3 = \begin{pmatrix} -\mathbb{1} & 0 \\ 0 & \mathbb{1} \end{pmatrix}. \tag{A.9}$$

Two additional matrices are

$$\Sigma = \begin{pmatrix} \sigma & 0 \\ 0 & \sigma \end{pmatrix}, \tag{A.10}$$

$$\sigma^{\mu\nu} = \tfrac{i}{2}(\gamma^\mu\gamma^\nu - \gamma^\nu\gamma^\mu). \tag{A.11}$$

Product rules

With the metric

$$g^{\mu\nu} = \begin{pmatrix} 1 & 0 & 0 & 0 \\ 0 & -1 & 0 & 0 \\ 0 & 0 & -1 & 0 \\ 0 & 0 & 0 & -1 \end{pmatrix}, \tag{A.12}$$

and $g^{\mu\nu}g_{\mu\nu} = 4$, one has

$$\gamma^\mu\gamma^\nu + \gamma^\nu\gamma^\mu = 2g^{\mu\nu}, \tag{A.13}$$

$$\gamma_\mu\gamma^\nu\gamma^\mu = -2\gamma^\nu, \tag{A.14}$$

$$\gamma_\mu\gamma^\nu\gamma^\lambda\gamma^\mu = 4g^{\nu\lambda}, \tag{A.15}$$

$$\gamma_\mu\gamma^\nu\gamma^\lambda\gamma^\sigma\gamma^\mu = -2\gamma^\nu\gamma^\lambda\gamma^\sigma. \tag{A.16}$$

Trace Theorems

One has

$$Tr(\gamma^{\mu_1}\gamma^{\mu_2}...\gamma^{\mu_n}) = 0 \quad \text{if } n \text{ is odd}, \tag{A.17}$$

$$Tr(\gamma^\mu\gamma^\mu) = 4g^{\mu\nu}, \tag{A.18}$$

$$Tr(\gamma^\mu\gamma^\mu\gamma^\lambda\gamma^\sigma) = 4(g^{\mu\nu}g^{\lambda\sigma} - g^{\mu\lambda}g^{\nu\sigma} + g^{\mu\sigma}g^{\nu\lambda}), \tag{A.19}$$

$$Tr(\gamma^5) = 0, \tag{A.20}$$

$$Tr(\gamma^5\gamma^\mu\gamma^\mu\gamma^\lambda\gamma^\sigma) = 4i\epsilon^{\mu\nu\lambda\sigma}, \tag{A.21}$$

where $\epsilon^{\mu\nu\lambda\sigma} = -1$ if $\mu\nu\lambda\sigma$ is an even permutation of 0123, $+1$ for an odd permutation and 0 if any two indices are the same. Note that

$$\epsilon^{\mu\nu\lambda\sigma}\epsilon_{\mu\nu\rho\tau} = -2(\delta^\lambda_\rho\delta^\sigma_\tau - \delta^\lambda_\tau\delta^\sigma_\rho). \tag{A.22}$$

Dirac Algebra

The anti-commutator defines the Dirac algebra

$$\{\gamma^\mu, \gamma^\nu\} = 2g^{\mu\nu}. \tag{A.23}$$

[1] The number 5 is a relic of old notation in which γ^0 was called γ^4.

Appendix B

Vacuum Polarization

In general, quantum field theories are not renormalizable. This means that certain quantities are not calculable, because some terms are divergent. In many cases this is not a characteristic of the theory, instead it is a manifestation of the nonexistence of the proper mathematical tools.

In this appendix we would like to illustrate exemplary the renormalization and regularization procedure for the vacuum polarization. The renormalization rewrites the expression in terms which are finite and terms which are infinite. With the regularization formalism the infinite term can be calculated in a finite way.

B.1 Renormalization

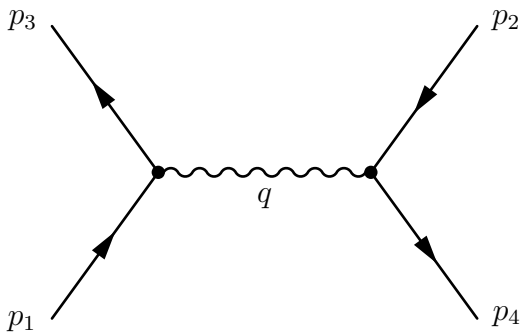

Figure B.1: Feynman diagram for a leading order process ($e^+e^- \to \mu^+\mu^-$).

Let us consider an electron-muon scattering, in lowest order the diagram looks like in Fig. B.1 and the corresponding amplitude

$$\mathcal{M} = -e^2 \left[\bar{e}(p_3)\gamma^\mu e(p_1)\right] \frac{g_{\mu\nu}}{q^2} \left[\bar{\mu}(p_4)\gamma^\nu \mu(p_2)\right], \tag{B.1}$$

with $q = p_1 - p_3$. There are a lot of higher order corrections to this diagram, but perhaps the most interesting is vacuum polarization, shown in Fig. B.2.

In this case the virtual photon momentarily splits into an electron-positron pair, leading to a

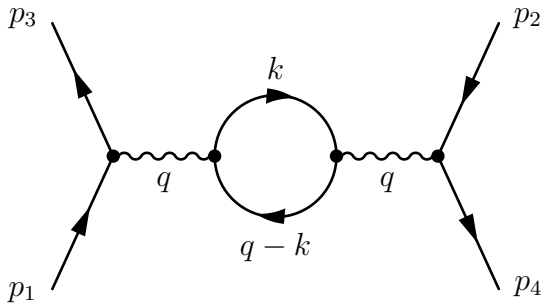

Figure B.2: Feynman diagram for a next-to-leading order process ($e^+e^- \to \mu^+\mu^-$) with vacuum polarization.

modification in the effective charge, as it will be seen. The amplitude for the second diagram is

$$\mathcal{M}_{\rm corr} = -ie^2\big[\bar{e}(p_3)\gamma^\mu e(p_1)\big]\ \left(\tfrac{-ig_{\mu\sigma}}{q^2}\right) I_2^{\sigma\rho}\left(\tfrac{-ig_{\rho\nu}}{q^2}\right)\big[\bar{\mu}(p_4)\gamma^\nu \mu(p_2)\big], \tag{B.2}$$

where [1]

$$I_2^{\sigma\rho} = -e^2\int \frac{d^4k}{(2\pi)^4}\frac{Tr[\gamma^\sigma(\not{k}+m)\gamma^\rho(\not{k}-\not{q}+m)]}{(k^2-m^2)[(k-q)^2-m^2]}. \tag{B.3}$$

The integral in Eq. (B.3) carries two space-time indices. Once one has integrated over k, the only four-vector left is q^μ, so $I^{\mu\nu}$ must have the form (where the indices are relabeled)

$$I_2^{\mu\nu} = i(q^2 g^{\mu\nu} - q^\mu q^\nu) I_2(q^2). \tag{B.4}$$

Now let us consider the exact photon two point function

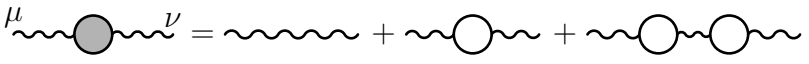

$$\begin{aligned} &= \frac{-ig_{\mu\nu}}{q^2} + \frac{-ig_{\mu\rho}}{q^2}\Big[i(q^2 g^{\rho\sigma} - q^\rho q^\sigma) I(q^2)\Big]\frac{-ig_{\sigma\nu}}{q^2} + ... \\ &= \frac{-ig_{\mu\nu}}{q^2} + \frac{-ig_{\mu\rho}}{q^2}\Delta_\nu^\rho I(q^2) + \frac{-ig_{\mu\rho}}{q^2}\Delta_\sigma^\rho\Delta_\nu^\sigma I^2(q^2) + ..., \end{aligned} \tag{B.5}$$

where $\Delta_\nu^\rho = \delta_\nu^\rho - q^\rho q_\nu/q^2$. Noting that $\Delta_\sigma^\rho\Delta_\nu^\sigma = \Delta_\nu^\rho$, one can simplify this expression to

$$\begin{aligned} &= \frac{-ig_{\mu\nu}}{q^2} + \frac{-ig_{\mu\rho}}{q^2}\left(\delta_\nu^\rho - \frac{q_\mu q_\nu}{q^2}\right)\big(I(q^2) + I^2(q^2) + ...\big) \\ &= \frac{-i}{q^2\big(1-I(q^2)\big)}\left(g_{\mu\nu} - \frac{q_\mu q_\nu}{q^2}\right) + \frac{-i}{q^2}\left(\frac{q_\mu q_\nu}{q^2}\right). \end{aligned} \tag{B.6}$$

[1] The considered Feynman rules are: 1. Every closed fermion loop gives a factor of (-1). 2. It gives the trace of a product of Dirac matrices. 3. Integration over the momenta.

According to the Ward identity [2] [87] one can abbreviate our result to

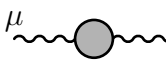

$$= \frac{-ig_{\mu\nu}}{q^2\big(1-I(q^2)\big)}. \tag{B.7}$$

Let us suppose $I(q^2)$ is computed to leading order in $\alpha = e^2/4\pi$ then $I(q^2) \approx I_2(q^2)$. The amplitude for the process will then involve the quantity

$$\alpha_0 \to \alpha_{\text{eff}}(q^2) = \frac{e_0^2/4\pi}{1-I(q^2)} \overset{\mathcal{O}(\alpha)}{=} \frac{\alpha}{1-[I_2(q^2)-I_2(0)]}, \tag{B.8}$$

where e_0 is the bare charge.

B.2 Regularization

We still have to calculate $I_2^{\mu\nu}(q^2)$ in order to fully understand the loop effects. Unfortunately, this integral Eq. (B.3) is divergent. In a sloppy manner, one can see that

$$I_2^{\mu\nu}(q^2) \sim \int |k|^3 d|k| \frac{|k|^2}{|k|^4} = \int |k| dk = |k|^2, \quad \text{as } |k| \to \infty. \tag{B.9}$$

To calculate $I_2^{\mu\nu}(q^2)$ one has to regularize the involved integral. The easiest way is to just introduce a cutoff Λ which makes the integral finite. The problem is that the Ward identity is no more valid. A dimensional regularization, due to [88], is a second option which preserves the Ward identity. In [4], the dimensional regularization is done. For the other solution see [89]. With dimensional regularization one gets

$$I_2(q^2) = -\frac{2\alpha}{\pi}\int_0^1 dx\, x(x-1)\left(\frac{2}{\epsilon} - \log\Delta - \gamma + \log(4\pi)\right), \qquad (\epsilon = 4-d) \tag{B.10}$$

where $\Delta = m^2 - x(1-x)q^2$ and $\gamma \approx 0.5772$ is the Euler-Mascheroni constant. This term is still logarithmically divergent. What is observed is the effective electric charge. Due to Eq. (B.8) this quantity is

$$\hat{I}_2(q^2) \equiv I_2(q^{2)} - I_2(0) = -\frac{2\alpha}{\pi}\int_0^1 dx\, x(x-1)\log\left(\frac{m^2}{m^2 - x(1-x)q^2}\right), \tag{B.11}$$

which is independent of ϵ. In high energy physics one is interested in small distances or $-q^2 \gg m^2$, for that Eq. (B.11) then becomes

$$\begin{aligned}\hat{I}_2(q^2) &\approx \frac{2\alpha}{\pi}\int_0^1 dx\, x(x-1)\left[\log\left(\frac{-q^2}{m^2}\right) + \log\big(x(1-x)\big) + \mathcal{O}\left(\frac{m^2}{q^2}\right)\right] \\ &\approx \frac{\alpha}{3\pi}\left[\log\left(\frac{-q^2}{m^2}\right) - \frac{5}{3} + \mathcal{O}\left(\frac{m^2}{q^2}\right)\right].\end{aligned} \tag{B.12}$$

[2] Ward identity is the amplitude $\mathcal{M}$ vanishes when the polarization vector $\epsilon_\mu(k)$ is replaced by k_μ, $k_\mu \mathcal{M}^\mu(k) = 0$. It is essentially a statement of current conservation. A proof can be found in [4].

The effective coupling constant in this limit is therefore

$$\alpha_{\text{eff}}(q^2) = \frac{\alpha}{1 - (\alpha/3\pi)\log\left(\frac{-q^2}{Am^2}\right)}, \tag{B.13}$$

where $A = \exp(5/3)$. The effective electric charge becomes much larger at small distances (high q^2).

Appendix C

Momentum Resolution Measurement

For the bending radius of a particle, with momentum p in a magnetic field B, the following relation was found in section 2.1.1

$$R = \frac{p}{0.3B}. \tag{C.1}$$

The particles pass through the magnet following a circular trajectory, where in general the bending radius R, is large compared to the magnet length L. Therefore, the deflection angle θ can be approximated by

$$\theta \approx \frac{L}{R}, \tag{C.2}$$

where the notation, illustrated in Fig. C.1, was used.

The sagitta s is related to the angle θ and the bending radius R by

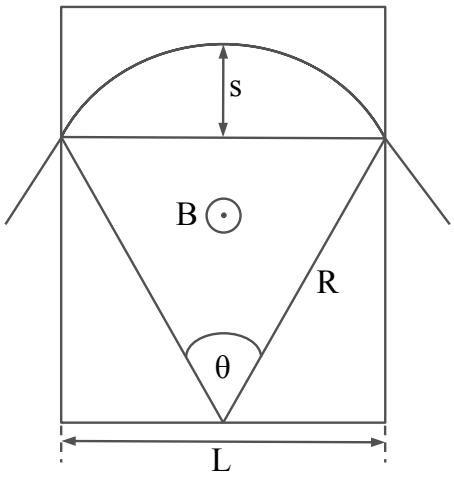

Figure C.1: Illustration of the different variables used for the momentum determination.

$$s = R - R\cos\left(\frac{\theta}{2}\right) = R\left(1 - \cos\left(\frac{\theta}{2}\right)\right). \tag{C.3}$$

Because of $1 - \cos\left(\frac{\theta}{2}\right) = 2\sin^2\left(\frac{\theta}{4}\right)$, one obtains

$$s = 2R\sin^2\left(\frac{\theta}{4}\right). \tag{C.4}$$

Since $\theta \ll 1$, the sagitta can be approximated by

$$s \approx \frac{R\theta^2}{8}. \tag{C.5}$$

Using Eq. (C.1) and the approximation Eq. (C.2) s can be expressed by

$$s \approx \frac{0.3BL^2}{8p}. \tag{C.6}$$

This leads to a momentum resolution from track measurement errors of

$$\frac{\Delta p}{p} = \frac{\Delta s}{s} = \frac{\sqrt{\frac{3}{2}}\Delta x \cdot 8p}{0.3BL^2}, \tag{C.7}$$

where $\Delta s = \sqrt{\frac{3}{2}}\Delta x$, under the assumption that the position is measured from three tracking detectors positions and the errors Δx are the same for all chambers.

In a more general calculation and considering the track measured not only at three but at N points equally distributed over the magnet length L, it can be shown that the momentum resolution due to the finite track measurement error is given by Glückstern's equation

$$\frac{\Delta p}{p} = \frac{\Delta x \cdot p}{0.3BL^2}\sqrt{720/(N+4)}. \tag{C.8}$$

For more detail see [90].

Appendix D

Novel Technique for Studying the Z Boson Transverse Momentum

This method looks only at low Z boson p_t candidates, which is equivalent to events with large dielectron azimuthal separation, $\Delta\phi > \frac{\pi}{2}$. For these events two new parameters are introduced, by decomposing the Z boson p_t into two orthogonal components (see Fig. D.1); one transverse,

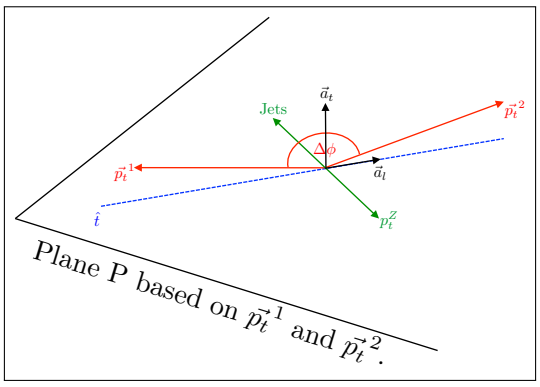

Figure D.1: A schematic representation in the transverse plane, of the construction of a_t and a_l in a typical electron/positron Z decay.

a_t, and the other parallel, a_l, to the dielectron thrust axis. The thrust axis $\hat{t}$ is defined as

$$\hat{t} = \frac{\vec{p}_t^{\,1} - \vec{p}_t^{\,2}}{|\vec{p}_t^{\,1} - \vec{p}_t^{\,2}|}, \tag{D.1}$$

where $\vec{p}_t^{\,i}$ is the transverse momentum vector of electron i. The transverse momentum vector of the dielectron system is of course, $\vec{p}_t^{\,Z} = \vec{p}_t^{\,1} + \vec{p}_t^{\,2}$. It is decomposed into the transverse component

$$a_t = |\vec{p}_t^{\,Z} \times \hat{t}| \tag{D.2}$$

and longitudinal to the thrust axis,

$$a_l = \vec{p}_t^{\,Z} \cdot \hat{t}. \tag{D.3}$$

For events with $\Delta\phi < \frac{\pi}{2}$, a_t is set equal to p_t^Z, while a_l maintains the same definition for all values of $\Delta\phi$.

Two quantities are defined: the detector level quantity, X_{reco}, and the generator quantity, X_{gen}, where X corresponds to p_t^Z, a_t and a_l. Fig. D.2 show the mean resolution, $|X_{\text{reco}} - X_{\text{gen}}|/X_{\text{gen}}$ as a function of the generator p_t^Z.

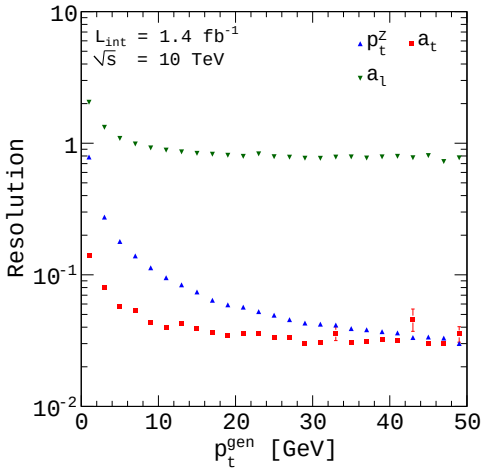

Figure D.2: Mean resolution $|X_{\text{reco}} - X_{\text{gen}}|/X_{\text{gen}}$ for each of the observables, p_t^Z, a_t and a_l as a function of the generator p_t^Z.

At low p_t^Z, $\Delta\phi \sim \pi$, the uncertainty on a_t is much smaller than the uncertainty on the p_t^Z. This is due to the fact that the uncertainty on a_t is approximately the uncertainty on the individual lepton p_t's, multiplied by the sine of a small angle. In contrast, the uncertainty on a_l is approximately the uncertainty on the individual lepton p_t's multiplied by the cosine of a small angle, i.e.

$$\delta a_t = \delta(p_t^1 + p_t^2)\sin(\alpha), \tag{D.4}$$

where α is the angle between the thrust axis and the electron, whereas the $|\hat{t}| = 1$. For a_l one obtains:

$$\delta a_l = \delta(p_t^1 + p_t^2)\cos(\alpha). \tag{D.5}$$

The $\sin\alpha$ can be approximated for small α, as α, and the $\cos\alpha$ with 1. Thus, the uncertainty on the a_l is equal to the uncertainty on the leptons and the uncertainty of the a_t is smaller than the uncertainty on the leptons by the factor α. However, for our purpose the Z p_t resolution is small enough with respect to the uncertainties on the measurement using $10\,\text{pb}^{-1}$ at $10\,\text{TeV}$, which means that we will consider the Z p_t for the rest of the thesis.

Appendix E

Additional Work

In this appendix I will list some additional work that I have done during my PhD for the CMS collaboration. The reason to not include it in the main part of the thesis is that this work was mainly a service job and did not produce primary physics results.

Electron Validation

At the time I started with my PhD the CMS event reconstruction software (CMSSW) was in its infancy. A lot of development work was still required. In the past three years many new releases had to be validated. Dealing a lot with electron distributions in my primary analysis work I was asked to carry out the electron validation for each new release. In Tab. E.1 the releases with the timetable are listed. Before March 2008 I was still setting up my tools. After July 2009 the validation became for the most part automatic.

Date	Release	Work
March 2008	CMSSW 1.6.10	Electron validation for fast and full simulation.
April 2008	CMSSW 1.6.10_patch	Electron validation for fast and full simulation.
July 2008	CMSSW 1.6.12	Electron validation for fast and full simulation.
October 2008	CMSSW 2.1.10	Electron validation for fast and full simulation.
November 2008	CMSSW 2.2.0	Electron validation for fast and full simulation.
December 2008	CMSSW 2.2.1	Electron validation for fast and full simulation.
March 2009	CMSSW 3.1.0/pre4	Electron validation for fast and full simulation.
June 2009	CMSSW 3.1.0/pre9	Electron validation for fast and full simulation.
June 2009	CMSSW 3.1.0/pre10	Electron validation for fast and full simulation.
July 2009	CMSSW 3.1.0/pre11	Electron validation for fast and full simulation.

Table E.1: Validation work list. (preX means previous version, before the release got approved.)

PAT Tuples Validation

In May 2008 a huge production of Monte Carlo samples was used to prepare for many physics papers, which means doing the entire analysis with these Monte Carlo samples, as they would be done with real data. In the same time a new data format, the so-called PAT Tuples (Physics Analysis Toolkit Tuples), were developed. With a small working group I tried to do the analysis with this new data format. We could achieve a good agreement between the established data format and the new PAT Tuples for the electron and Z variables.

Mis-alignment and -calibration Study

In the beginning of 2008 we were waiting for the startup of the experiment in the summer, which indeed happened in September. This was the reason to have a bigger study on the electron reconstruction for different alignment and calibration scenarios. We were convinced at the time, that the alignment and the calibration would be quite bad at the beginning of the experiment and would improve with more data. The analysis showed for four different scenarios:

- startup ($0\,\mathrm{pb}^{-1}$),
- after a few months (($10\,\mathrm{pb}^{-1}$),
- after a year ($100\,\mathrm{pb}^{-1}$) and
- ideal conditions,

how the electron distributions, the efficiency and the Z boson selection would look. Today we know that the detector was much better aligned and calibrated at startup that we expected. The outcome of the work was showed in two presentations [91] and [92].

October Exercise

In October 2009, just one month before the second start of the LHC, within the CMS collaboration a huge exercise was planned. The idea was to simulate the start of the LHC and try to make short analysis in a short space of time. My contribution to this so-called "October exercise" was to run my tag and probe analysis on a $Z \to e^+e^-$ sample and produce a several plots, like the ones shown in Figs. 3.25 and 3.26. Following a preparation time of a few weeks, I was able to produc these plots within a few hours, and they were consistent with other group members who did the same with their own tools.

Bibliography

[1] E. Witten: *What's ahead in Particle Physics* presented at: ICHEP 2008, 04/08/2008.

[2] CDF Collaboration: *Observation of Top Quark Production in $\bar{p}p$-Collisions* in: Phys. Ref. Lett. **74**, 2626 (1995).

[3] L. W. Bennett: *Some Recollections and Reflections on Rutherford* in: Notes Rec. R. Soc. Lond. **27**, 61 (1972).

[4] M. E. Peskin and D. V. Schroeder: *An Introduction to Quantum Field Theory* (Westview Press, Colorado, 1995).

[5] K. Nakamura et al.: *Particle Data Group* in: Journal of Physics G 37, 075021 (2010).

[6] H. Weyl: *Elektron und Gravitation I* in: Zeitschrift für Physik **56**, 330 (1929).

[7] E. Noether: *Invariante Variationsprobleme* in: Nachrichten der Königlichen Gesellschaft der Wissenschaft zu Göttigen, Math-Phys. 235 (1918).

[8] P. A. M. Dirac: *The Quantum Theory of the Electron* in: Proc. Roy. Soc. A **117**, 610 (1928).

[9] J. C. Maxwell: *A Dynamical Theory of the Electromagnetic Field* in: Philosophical Transactions of the Royal Society of London, 459-512, 155 (1865).

[10] F. Reines and C. L. Cowan: *Free Antineutrino Absorption Cross Section. I. Measurement of the Free Antineutrino Absorption Cross Section by Protons* in: Phys. Rev. **113**, 273 (1958).

[11] T. D. Lee and C. N. Yang: *Question of Parity Conservation in Weak Interactions* in Phys. Rev. **104**, 256 (1956).

[12] C. S. Wu et al.: *Experimental Test of Parity Conservation in Beta Decay* in Phys. Rev. **105**, 1413 (1957).

[13] M. Goldhaber et al.: *Helicity of Neutrinos* in Phys. Rev. **109**, 1015 (1958).

[14] S. L. Glashow: *Partial-Symmetries of Weak Interactions* in: Nucl. Phys. **22**, 579 (1961); A. Salam: *Elementary Particle Physics* edited by: N. Svartholm (Almqvist and Wiksell, Stockholm, 1968); S. Weinberg: *A Model of Leptons* in: Phys. Rev. Lett. **19**, 1264 (1967).

[15] P. W. Higgs: *Broken Symmetries and the Masses of Gauge Bosons* in: Phys. Rev. Lett. **13**, 508 (1964); Phys. Rev. **145**, 1156 (1966).

[16] F. J. Hasert et al. (Gargamelle Collaboration): *Search for Elastic Muon Neutrino Electron Scattering* in: Phys. Lett. B **46**, 121 (1973).

[17] G. Arnison et al. (UA1 Collaboration): *Experimental Observation of Isolated Large Transverse Energy Electrons with Associated Missing Energy at* $\sqrt{s} = 540\,GeV$ in: Phys. Lett. B **122**, 103 (1983).

[18] Y. Nambu: *A 'Superconductor' Model of Elementary Particles and its Consequences* in: Proceedings of the Midwest Conference on Theoretical Physics, Lafayette, Indiana, 1960.

[19] S. Weinberg: *A Model of Leptons* in: Phys. Rev. Lett. **19**, 1264 (1967).

[20] B. Kibble: *Symmetry Breaking in Non-Abelian Gauge Theories* in: Phys. Rev. **155**, 1554 (1967).

[21] T. D. Lee and C. N. Yang: *Conservation of Heavy Particles and Generalized Gauge Transformations* in: Phys. Rev. **98**, 1501 (1955).

[22] S. Weinberg: *Dynamical Approach to Current Algebra* in: Phys. Rev. Lett. **18**, 188 (1967).

[23] The ALEPH, CDF, D0, DELPHI, L3, OPAL, SLD Collaborations, the LEP Electroweak Working Group, the Tevatron Electroweak Working Group, the SLD Electroweak and Heavy Flavour Groups: *Precision Electroweak Measurements and Constraints on the Standard Model* in: arXiv:0811.4682v1 (hep-ex) (2008); updates for Summer 2009 from URL: `http://lepewwg.web.cern.ch/LEPEWWG/`.

[24] M. Gell-Mann: *A Schematic Model of Baryons and Mesons* in: Phys. Lett. **8**, 214 (1964); G. Zweig: *An SU*(3) *Model for Strong Interaction Symmetry and its Breaking* in: CERN-TH-401 (1964).

[25] V. E. Barnes et al.: *Observation of a Hyperon with Strangeness Minus Three* in: Phys. Rev. Lett. **12**, 204206 (1964).

[26] R. P. Feynman: *QED: The Strange Theory of Light and Matter.* (Princeton University Press, New Jersey, 1985).

[27] W. Pauli: *Über den Zusammenhang des Abschlusses der Elektronengruppen im Atom mit der Komplexstruktur der Spektren* in: Zeitschrift für Physik 31, 76583 (1925).

[28] B. Povh and K. Rith: *Particles and Nuclei: An Introduction to the Physical Concepts* (Springer, Berlin, 2004).

[29] M. Schmelling: *QCD Results from the Study of Hadronic Z Decays* in: Phys. Scripta **51**, 683 (1995).

[30] R. P. Feynman in: Proceedings of the 3^{rd} Topical conference on High Energy Collision of Hadrons, Stony Brook, New York, 1969.

[31] G. Sterman: *Handbook of Perturbative QCD* in: Rev. Mod. Phys. **67**, 157 (1995).

[32] A. D. Martin et al.: *Parton Distributions for the LHC* in: Eur. Phys. J. **C63**, 189 (2009).

[33] The ALEPH, DELPHI, L3 and OPAL Collaborations and the LEP Working Group for Higgs Searches: *Search for the Standard Model Higgs Boson at LEP* in: Phys. Lett. B **565**, 61 (2003).

[34] F. Zwicky: *Die Rotverschiebung von extragalaktischen Nebeln* in: Helvetica Physica Acta **6**, 110 (1933).

[35] P. J. E. Peebles and B. Ratra: *The Cosmological Constant and Dark Energy* in: Rev. Mod. Phys. **75**, 559 (2003).

[36] A. Arkani-Hamed, A. Delgado, and G. F. Giudice: *The Well-tempered Neutralino* in: Nucl. Phys. B **741**, 108 (2006).

[37] A. Einstein: *Induktion und Deduktion in der Physik* in: Berliner Tagblatt und Handelszeitung, 25/12/1919.

[38] S. Dailler: *Map of the Geneva region and of the LHC* in: LHC-PHO-1997-169 (1997).

[39] W. K. H Panofsky and M. Breidenbach: *Accelerators and Detectors* in: SLAC-PUB-7780, (1998).

[40] AC Team: *Diagram of an LHC dipole magnet* in: CERN-DI-9906025 (1999).

[41] J.-L. Caron: *LHC Layout* in: LHC-PHO-1997-060 (1997).

[42] CMS Collaboration: *CMS, the Compact Muon Solenoid: technical proposal* in: CERN-LHCC-94-38, LHCC-P-1. (1994).

[43] ATLAS Collaboration: *ATLAS: technical proposal for a general-purpose pp experiment at the Large Hadron Collider at CERN* in: CERN-LHCC-94-43, LHCC-P-2. (1994).

[44] CMS Outreach: *CMS Detector Drawings - Drawing of the complete CMS detector, showing both the scale and complexity with labels.*
URL: `http://cms.web.cern.ch/cms/Media/Images/Detector/Detector_Drawings/index.html`
(accessed 5$^{\text{th}}$ January 2010).

[45] CMS Collaboration: *The CMS Experiment at the CERN LHC* in: JINST **3** S08004 (2008).

[46] CMS Collaboration: *The CMS Tracker System Project: Technical Design Report* in: CERN-LHCC-98-006 (1997).

[47] BUL Collection: *CMS has a Heart of Pixels.* in: BUL-PHO-2003-003 (2003).

[48] CMS Collaboration: *CMS Physics TDR: Detector Performance and Software* in: CERN-LHCC-2006-001 (2006).

[49] CMS Collection: *The Construction of the CMS Electromagnetic Calorimeter: Crystal Assembly* in: CMS-PHO-OREACH-2005-003 (2005).

[50] T. Bombadil: *The CMS experiment Dees* in: BUL-PHO-2008-070 (2008).

[51] CMS Collection: *The Construction of the CMS ECAL: Avalanche Photodiodes* in: CMS-PHO-OREACH-2005-002 (2005).

[52] CMS Outreach: *CMS Times*, March 2007,
URL: `http://cms.web.cern.ch/cms/Media/Publications/CMStimes/2007/03_26/index.html`
(accessed 11$^{\text{th}}$ January 2010).

[53] D. Del Re and P. Meridiani: *Observation of the* $\pi^0 \to \gamma(\to e^+e^-)\gamma$ *Signal in the First LHC Data* in: CMS AN-2010/052, February 2010.

[54] I. Peterson: *The Jungles of Randomness: A Mathematical Safari* (Wiley, New York, 1998), p. 178.

[55] T. Sjöstrand, S. Mrenna and P. Skands: *PYTHIA 6.4 Physics and Manual* in: JHEP05 026 (2006).

[56] W. Adam et al.: *Reconstruction of Electrons with the Gaussian Sum Filter in the CMS Tracker at the LHC* in: J. Phys. G: Nucl. Part. Phys. **31** N9-N20 (2005).

[57] E. Meschi et al.: *Electron reconstruction in the CMS Electromagnetic Calorimeter* in: CMS Note 2001/034 (2001).

[58] H. W. Sorenson: *Least-Squares estimation: from Gauss to Kalman* in: IEEE Spectrum 7 (1970).

[59] R. E. Kalman: *A New Approach to Linear Filtering and Prediction Problems* in: Transaction of the ASME-Journal of Basic Engineering (1960).

[60] H. Bethe and W. Heitler: *On the Stopping of Fast Particles and on the Creation of Positive Electrons* in: Proc. of the R. Soc. Lond. A **856**, 146 (1934).

[61] W. Adam et al.: *Track Reconstruction in the CMS Tracker* in: CMS NOTE-2006/041 (2006).

[62] M. Dittmar, W. Hintz and C. Marchica: *Towards a Simple, Robust and Clean Electron Selection for the* $H \to W^+W^-$ *Search.* in: CMS AN -2009/134 (2009).

[63] M. LeBourgeois: *A Study of Electron Isolation*, Dezember 2007, at URL:
`http://indico.cern.ch`

[64] S. Harper and C. Shepherd: *Improving Sigma Eta Eta*, September 2008, at URL:
`http://indico.cern.ch`

[65] N. Adam et al.: *Towards a Measurement of the Inclusive* $W \to e\nu$ *and* $Z \to e^+e^-$ *Cross Sections in pp Collisions at* $\sqrt{s} = 10$ *TeV.* in: CMS AN-2009/098, July 2009.

[66] Ronald Ch. Remington: *CMS Detector Sensitivity for the Discovery of Supersymmetry with Two Same-sign Leptons, Jets and MET.* in: CMS CR-2009/257, August 2009.

[67] G. Bauer et al.: *Conversion Removal for Electron Fakes and Charge Misidentification* in: CMS AN-2009/173, November 2009.

[68] N. Adam et al.: *Towards a Measurement of the Inclusive Wev and Zee Cross Sections in pp Collisions at $\sqrt{s} = 10\ TeV$* in: CMS AN-2009/098, May 2009.

[69] N. Adam et al.: *Generic Tag and Probe Tool for Measuring Efficiency at CMS with Early Data* in: CMS AN-2009/111, June 2009.

[70] D. J. Boorstin: *The Six O'Clock Scholar* in: The Washington Post, 29/01/1984.

[71] M. Vesterinen, T. R. Wyatt: *A Novel Technique for Studying the Z Boson Transverse Momentum Distribution at Hadron Colliders* in: arXiv:0870.4956v1 (2008).

[72] N. Adam, V. Halyo, A. Hunt, D. Marlow et al.: *Measurement of CMS Luminosity in the 2010 Run* in: CMS AN-2010/175, June 2010

[73] C. Anastasiou et al.: *A new Method for Real Radiation at Next-to-Next-to-Leading Order* in: Phys. Rev. D **69**, 076010 (2004).

[74] A. D. Martin et al.: *Uncertainties on α_s in Global PDF Analyses and Implications for Predicted Hadronic Cross-Sections* in: Eur. Phys. J. C **64** 653 (2009).

[75] URL: `http://www.phys.psu.edu/ cteq/`

[76] URL: `http://durpdg.dur.ac.uk/hepdata/mrs.html`

[77] URL: `http://projects.hepforge.org/lhapdf/pdfsets`

[78] T. Sjoöstrand, St. Mrenna and P. Skands: *A Brief Introduction to PYTHIA 8.1* in: arXiv:0710.3820 (2007).

[79] T. Gleisberg et al.: *Event Generation with Sherpa 1.1* in: arXiv:0811.4622 (2009).

[80] S. Gieseke et al.: *Herwig++ 2.0 Release Note* in: arXiv:hep-ph/0609306v1 (2006).

[81] J. Alwall et al.: *MadGraph/MadEvent v4: The New Web Generation* in: arXiv:0706.2334 (2007).

[82] CMS Collaboration: *Measurements of Inclusive W and Z Cross-Section in pp Collisions at $\sqrt{s} = 7\ TeV$* in: CMS PAS EWK-10-002 (2010).

[83] T. Affolder et al.: *Measurement of $d\sigma/dy$ for High Mass Drell-Yan e^+e^- Pairs from $p\bar{p}$ Collisions at $\sqrt{s} = 1.8\ TeV$* in: Phys. Rev D **63**, 011101, 2001a.

[84] G. P. Salam and G. Soyez: *A practical seedless infrared-safe cone jet algorithm* in: JHEP05, 086 (2007).

[85] G. Dissertori, M. Dittmar, J. Eugster, W. Hintz, C. Marchica, P. Meridiani, A.K. Sanchez: *Towards a Precise Measurement of the W and Z Boson p_t Spectrum with CMS* in: CMS AN-2010/282 (2010).

[86] I. Asimov: *The Eureka Phenomenon* in: Fiction and Science-Fiction, June 1971.

[87] J. C. Ward: *An Identity in Quantum Electrodynamics* in: Phys. Rev. **78**, 182 (1950).

[88] G. 't Hooft and M. J. G. Veltman: *Regularization and Renormalization of Gauge Fields* in: Nucl. Phys. B **44**, 189 (1972).

[89] J. J. Sakurai: *Advanced Quantum Mechanics* (Addison-Wesley, London, 1967).

[90] R. L. Glückstern: *Uncertainties in Track Momentum and Direction due to Multiple Scattering and Measurement Errors* in: NIM **24**, 381 (1963).

[91] C. Marchica: *Electron reconstruction in 0pb, 10pb, 100pb and ideal detector conditions* URL: `http://indico.cern.ch/contributionDisplay.py?contribId=4&confId=27542`

[92] C. Marchica: *$Z \rightarrow ee$ validation in different mis-alignment/calibration scenarios* URL: `http://indico.cern.ch/contributionDisplay.py?contribId=2&confId=29383`

List of Abbreviations

ALICE	A Large Ion Collider Experiment
APD	Avalanche Photodiode
ATLAS	A Toroidal LHC Apparatus
BPix	Barrel Pixel Layer
CAF	CERN Analysis Facility
CERN	Conseil Europen pour la Recherche Nuclaire
CM	Center-of-Mass
CMBR	Cosmic Microwave Background Radiation
CMS	Compact Muon Solenoid
CSC	Cathode Strip Chambers
DAQ	Data Acquisition
DE	Dark Energy
DM	Dark Matter
DT	Drift Tubes
EB	ECAL Barrel
ECAL	Electromagnetic Calorimeter
EE	ECAL Endcap
ES	ECAL Preshower
FPix	Endcap Pixel Layer
GSF	Gaussian Sum Filter
GSW	Glashow-Salam-Weinberg Model
HB	HCAL Barrel
HCAL	Hadron Calorimeter

HE	HCAL Endcap
HLT	High-Level Trigger
IR	Interaction Region
KF	Kalman Filter
L1	Level-1 Trigger
LEP	Large Electron Positron Collider
LHC	Large Hadron Collider
LHCb	Large Hadron Collider beauty
LO	Leading Order
LSP	Lightest Supersymmetric Particle
MC	Monte Carlo
MET	Missing Transverse Energy
NLO	Next to Leading Order
PDF	Parton Distribution Function
pQCD	perturbative QCD
QCD	Quantum Chromodynamics
QED	Quantum Electrodynamics
RF	Radio-Frequency
RGE	Renormalization Group Equation
RPC	Resistive Plate Chambers
SISCone	Seedless Infrared-Safe Cone
SM	The Standard Model of Particle Physics
SUSY	Supersymmetry
TEC	Tracker EndCap
TIB	Tracker Inner Barrel
TID	Tracker Inner Disk
TOB	Tracker Outer Barrel
TP	Tag and Probe
VEC	Vacuum Expectation Value
VPT	Vacuum Phototriode
WLCG	Worldwide LHC Computing Grid

Acknowledgment

I would like thank Prof. Günther Dissertori and Quentin Ingram for having given me the possibility to write this thesis in this exciting subject of Particle Physics. Even if the promised data did not arrive as expected, it was a great experience to be a part of this huge collaboration of the CMS experiment at CERN.

Further I thank Michael Dittmar, not only for the intense collaboration, but also for many helpful suggestions, concerning particle physics amongst other things! Another special thank you goes to Fabian Stöckli, who helped me understand many technical aspects of the CMS framework. Similarly, I would like to thank also certain CMS collaborators, especially people working in the *EWK* (electroweak) and *egamma* (electron and photon) groups.

A special thank you goes to my editors, Edna Nendel and Tara Lorencak, who worked quite hard, getting out the "swissness" in my thesis.

Last, but certainly not least, my gratitude goes to my family, who have supported me all these years. I could not have done it without you!